Unione Europea

Ministero dell'Istruzione,
dell'Università e della Ricerca

Università degli Studi di Salerno

DIPARTIMENTO DI INGEGNERIA INDUSTRIALE

Dottorato di Ricerca in Ingegneria Meccanica
X Ciclo N.S. (2008-2011)

"Laser welding of Ti6Al4V alloy by disk laser: analysis and optimization"

Ing. Ernesto Mastrocinque

Tutor:

Prof. Vincenzo Sergi

Coordinatore:

Prof. Vincenzo Sergi

Alla mia famiglia

TABLE OF CONTENTS

CHAPTER 2   **Titanium: properties and applications**

CHAPTER 3   Literature review of titanium welding

ACKNOWLEDGMENTS

LIST OF FIGURES

LIST OF TABLES

SUMMARY

Titanium alloys have been successfully applied in many industrial fields because of their better performance and lighter weight than other commonly used structural materials. The conventional welding methods used for titanium alloys are tungsten inert gas (TIG) and plasma arc welding. In recent decades, autogenous processes with highly concentrated energy sources have become popular; these joining processes are laser and electron-beam welding. The power source can be concentrated in very small areas so as to achieve energy densities up to 10,000 times higher than those of the arc processes. Laser welding allows joints to be made with limited distortion. The fully-automated process, ensures high productivity and high-quality joints. Laser technology is acquiring industrial interest because the electron-beam processes have limitations, such as the need to operate in vacuum, the increased costs and the emission of X-rays. Titanium alloys are widely used in the aircraft industry, because of their high strength-to-weight ratio, corrosion resistance, operating temperature and bonding with composite materials (electrochemical compatibility, similar coefficients of thermal expansion). The criteria for the design, manufacture and operation were changed to obtain structures that are lighter and more efficient than the ones made of aluminum. However, the structures in carbonfiber- reinforced-polymer require the use of metal structures, especially in areas of great concentration of loads. In spite of several advantages, these alloys lead to excessive manufacturing costs related to the cost of the raw materials, the high volumes of waste and the complex and expensive finishing. For these reasons, it is cheaper to produce semi-finished products by welding simpler parts, instead of casting and forming processes; therefore, laser welding can be used due to its high productivity and quality end-products.

The aim of the thesis work is to find the better input process parameters values to weld 3 mm and 1 mm Ti6Al4V sheets using a 2 kW Yb:YAG disk laser. Both bead on plate and butt tests have been performed, and the beads quality is characterized in terms of geometric features, porosity content, microstructure, hardness and strength.

This work is organized in five chapters.

Chapter 1 discusses the principles of operation and the different types of laser including disk laser, used in the experimental part.

Chapter 2 presents the properties of titanium and its alloys, highlighting the various fields of application.

Chapter 3 presents a review of the different technologies used for welding of titanium alloys, focusing primarily on laser welding and its mechanisms.

Chapter 4 describes the titanium alloy, equipment and methodologies used in the experimental work.

Finally, Chapter 5 presents the results obtained.

CHAPTER 1

Laser

1.1   Introduction

Lasers are devices that amplify or increase the intensity of light to produce a highly directional, high-intensity beam that typically has a very pure frequency or wavelength. They come in sizes ranging from approximately one-tenth the diameter of a human hair to that of a very large building. Lasers produce powers ranging from nanowatts to a billion trillion watts (1021 W) for very short bursts. They produce wavelengths or frequencies ranging from the microwave region and infrared to the visible, ultraviolet, vacuum ultraviolet, and into the soft-X-ray spectral regions. They generate the shortest bursts of light that man has yet produced, or approximately five million-billionths of a second (5×10^{-15} s).

Lasers are a primary component of some of our most modern communication systems and are the probes that generate the audio signals from our compact disk players. They are used for cutting, heat treating, cleaning, and removing materials in both the industrial and medical worlds. They are the targeting element of laser-guided bombs and are the optical source in both supermarket checkout scanners and tools (steppers) that print our microchips.

Because of the special stimulated nature of the laser light source, and the apparatus needed to produce laser light, laser photons are generally not as cheap to produce or to operate as are other light sources of comparable power. We presently do not use them to light our rooms, as lamp bulbs for our flashlights, as headlights for our automobiles, or as street lamps. Lasers also don't generally provide "white light" but instead produce a specific "color" or wavelength, depending upon the laser used.

The word LASER is an acronym for Light Amplification by Stimulated Emission of Radiation. Stimulated emission of radiation is a

natural process first identified by Einstein. It occurs when a beam of light passes through a specially prepared medium and initiates or stimulates the atoms within that medium to emit light in exactly the same direction and exactly at the same wavelength as that of the original beam. A typical laser device (Figure 1.1) consists of an amplifying or gain medium, a pumping source to input energy into the device, and an optical cavity or mirror arrangement that reflects the beam of light back and forth through the gain medium for further amplification. A useful laser beam is obtained by allowing a small portion of the light to escape by passing through one of the mirrors that is partially transmitting.
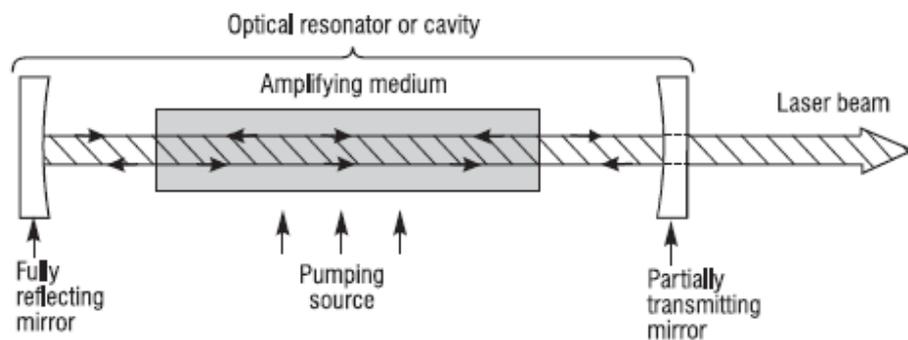
Figure 1.1 - Basic laser components

1.2   Requirements for a laser

1.2.1 Laser gain medium

Nearly all lasers are produced as a result of electrons jumping from an excited energy level within a radiating species to a lower-lying energy level and, in the process, radiating light that contributes to the laser beam. Those radiating species can include:

atoms such as in the red helium-neon (HeNe) laser, the visible and ultraviolet argon ion and helium-cadmium (HeCd) lasers, and the green and yellow copper vapor lasers (CVL)

molecules such as in the infrared carbon dioxide (CO_2) laser, the ultraviolet excimer lasers such as ArF and KrF, and the pulsed N_2 laser

liquids such as those involving various organic dye molecules dilutely dissolved in various solvent solutions dielectric solids such as those involving neodymium atoms doped in YAG or glass to make the crystalline Nd:YAG or Nd:glass lasers

semiconductor materials such as gallium arsenide or indium phosphide crystals or various mixtures of impurities blended with those and other semiconductor species Each of the above species contains a lowest energy level referred to as the ground state in which the electrons predominantly reside at room temperature, as indicated by level 0 in Figure 1.2.
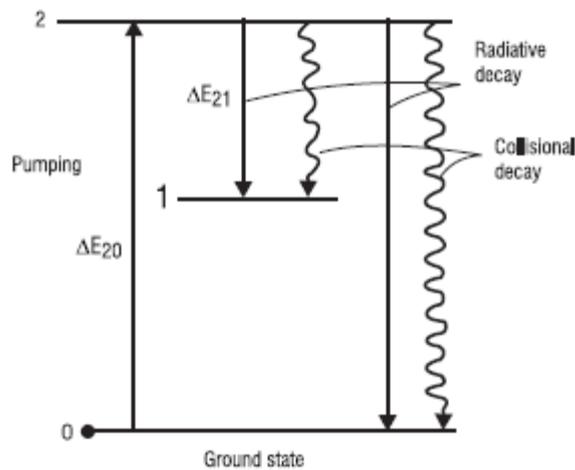
Figure 1.2 - Simplified energy diagram of an atom showing excitation and emission processes

The electrons are moved to higher-lying (excited) levels such as 1 and 2 by means of various pumping processes that will be described in the next section. They then decay back to lowerlying levels within a period of time called the lifetime of the level, and eventually find their way back to the ground state when the pumping source is removed. There are three types of processes involving the interaction of light beams with atoms that have electrons residing in various energy levels. Examples of those are depicted in Figure 1.3. First an electron residing in level 2 can spontaneously jump to level 1, radiating a photon of light when it does so.

That process is known as spontaneous emission as indicated in Figure 1.3a. Most excited energy levels undergo spontaneous emission.
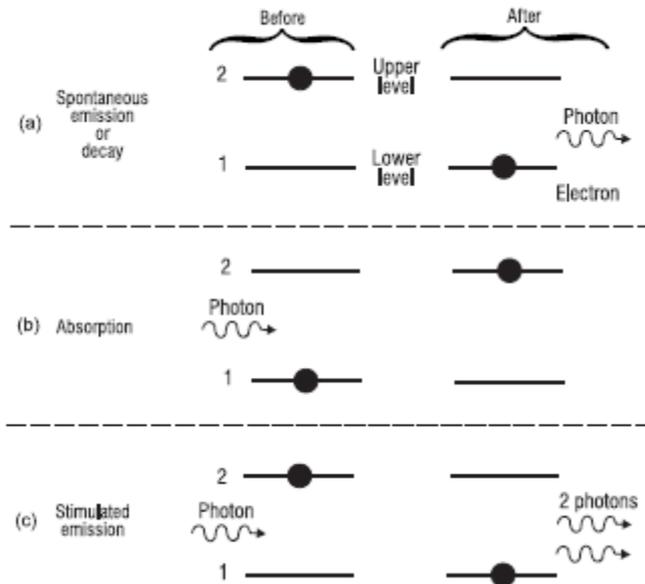
Figure1.3 - The three radiation processes that can occur when light interacts with matter

Each level has a specific lifetime τ over which it will remain in that level before decaying to a lower-lying level. That lifetime is determined by the interactions of the electron with the other electrons and nuclei of that atom. Typical lifetimes of electrons residing in specific levels that decay by radiating in the visible portion of the spectrum are of the order of 10–100 ns. Of course the ground state cannot decay further and thus has infinite lifetime. The photon radiated during spontaneous emission has the exact wavelength λ_{21} and frequency ν_{21} corresponding to the difference in energy ΔE_{21} of the two involved energy levels (1 and 2 in this case) according to the relationship in which h is Planck's constant such that h = 6.63×10^{-34} joule-s and c is the speed of light, c = 3×108 m/s.

$$\Delta E_{21} = h\nu_{21} = \frac{hc}{\lambda_{21}} \tag{1}$$

Also the wavelength λ_{21} is generally given in meters (often expressed in micrometers (μm) or nanometers (nm). Because different materials

have different energy-level arrangements, they radiate at different wavelengths and thus emit different colors or frequencies of light that are specific to the material. Nearly all the light we see originates from such transitions between energy levels of various kinds of matter. The second process is absorption, shown in Figure 1.3b, which occurs if the atom has its electron in level 1 of Figure 1.2 and a photon of light of wavelength λ_{21} collides with the atom. During the collision, the photon is absorbed by the atom and the electron is moved up to the higher energy level 2. This process is the way light interacts with practically all of matter. It can happen from any energy level that is occupied (generally the ground state) and always boosts the atom to a higher-lying level while eliminating the photon. This often results in heating of the absorbing material. The third process, shown in Figure 1.3c, is referred to as stimulated emission. It results when an electron is in a higher-lying level, such as level 2 in Figure 1.2, and a photon of light of wavelength λ_{21} collides with the atom. During the collision the photon stimulates the atom to radiate a second photon having exactly the same energy ΔE_{21} (and wavelength according to Equation 1) as that of the incident photon and traveling in exactly the same direction in order to satisfy the laws of conservation of energy and momentum. Hence, one photon leads to two identical photons, which, in effect, leads to an amplification process. A photon has been gained at the expense of the loss of energy stored within the atom. When a large group of atoms is assembled and irradiated with light, most of those atoms are in the ground-state energy level (Figure 1.2). If the photons of the impinging light have the appropriate energy ΔE_{20} for example, as indicated in Figure 1.2, the light will be absorbed according to the following expression for the variation of intensity I with the distance L into the material in which

$$I = I_0 e^{-\sigma_{20} N_0 L} \tag{2}$$

I_0 is the intensity of the beam when it first reaches the atoms, σ_{20} is referred to as the cross section for absorption or emission of those two levels, and N_0 is the population density of atoms residing in level 0 (number of atoms per unit volume). If N_0 is in atoms/cm^3 and L is in cm, the absorption cross section σ_{20} must be expressed in units of area or cm^2 (hence the name cross section). Equation 2 indicates that the amount of beam absorption depends on both the number density of atoms residing in level 0 and the length L or thickness of the medium comprising those

atoms as indicated in Figure 1.4. Also, the exponential factor suggests quite rapid absorption if the exponent is large. For example, $e^{-2} = 0.135$ and $e^{-4} = 0.018$. Hence, if either the length of the medium or the population is doubled, the beam intensity drops by nearly a factor of 8! Chemists have used this effect for many decades to measure the concentration of a material dissolved into a solvent. Equation 2 is known as Beer's law, and the product $\sigma_{20} N_0$ is referred to as the absorption coefficient. This absorption process is also one of the techniques used in pumping lasers in order to transfer population to level 2 from level 0, as will be discussed later.
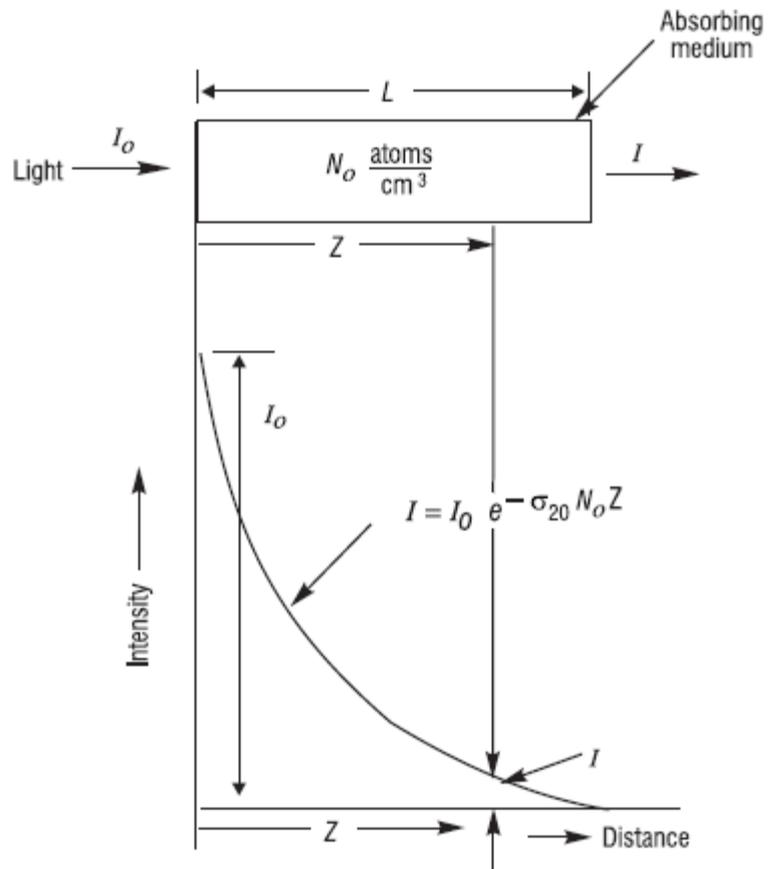
Figure 1.4 - Intensity variation versus depth z into an absorbing sample

The absorption described above could have been equally applied if population initially existed in level 1, and light of energy ΔE_{21} and wavelength λ_{21} would be absorbed by the medium according to the following equation.

$$I = I_0 e^{-\sigma_{21} N_1 L} \tag{3}$$

An alternative situation will now be considered. Suppose that we were able to "pump" (excite) a significant amount of population of the medium from level 0 to level 2 according to Equation 2. Also, for the time being let us assume that there is no population in level 1. Then again, let us consider having a beam of photons of energy ΔE_{21} and wavelength λ_{21} enter the medium. According to the earlier discussion, and considering the process described in Figure 1.3c, the only process that can occur is stimulated emission, and we would expect more photons to be generated as the beam progresses. That is exactly what happens! Since the absorption indicated in Figure 1.3b and also described in Equation 2 is a symmetrical process with the stimulated emission process of Figure 1.3c, it is not surprising that the beam evolves in a similar way to that of Equation 2 except that a sign reversal must be made in the exponent to reflect the process of photon production instead of photon absorption. This can be described mathematically in the equation below in which we

$$I = I_0 e^{+\sigma_{21} N_2 L} \tag{4}$$

now have the population density N_2 in the expression along with the appropriate cross section σ_{21}. Now, if population is allowed to be in both level 1 and level 2, both absorption and stimulated emission will occur within the medium and therefore Equations 2 3 4 must be combined to give

$$I = I_0 e^{+\sigma_{21}(N_2 - N_1)L} \tag{5}$$

as indicated in Figure 1.5. Hence, if more population exists in level 2 than in level 1, N_2 will be greater than N_1 and the exponent of Equation 5 will be positive. The beam will grow and emerge from the medium with a greater intensity than when it entered. In other words, for amplification or gain to occur, the condition must be

$$\frac{N_2}{N_1} > 1 \qquad (6)$$

Having N_2 be larger than N_1 is known as having a population inversion, which is not a normal, naturally occurring relationship. This would be the equivalent of having a mountain in which there is more dirt at higher levels than at lower levels. The mountain would taper inward toward the bottom rather than outward, which is generally an unstable situation. The only way to maintain such an "inversion" is to continually transfer or "pump" more dirt up to higher levels by a conveyor belt or some other process. The equivalent transfer to higher levels, or "pumping" is also required in lasers to maintain the population inversion of level 2 with respect to level 1 such that amplification can be produced.
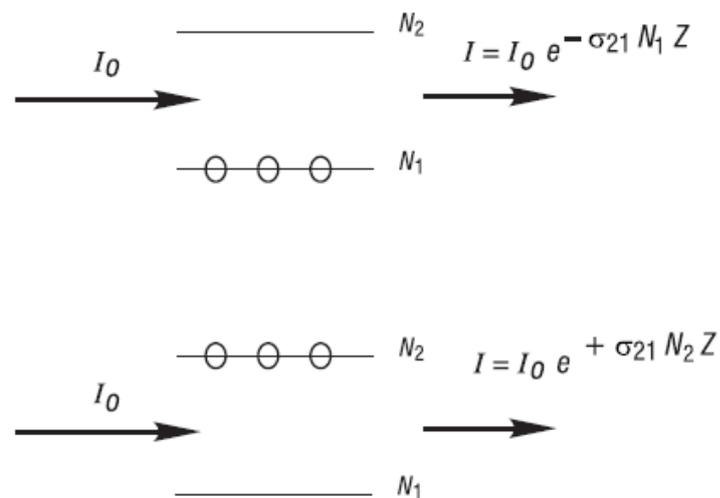
Figure 1.5 - Absorption and stimulated emission effects combined in a laser gain medium

Population inversions in gases - Inversions in gases are generally produced by applying a voltage across a gas discharge tube that consists of a long, narrow glass or ceramic tube serving to confine the gain medium, with electrodes installed at each end of the tube. In its simplified form the electrodes, which are essentially electrical feedthroughs, are

attached to each end of the tube to allow a voltage to be applied across the length of the tube. The tube is then filled with a low-pressure gas or gas mixture that includes the species that will serve as the gain medium. The applied voltage produces an electric field within the laser tube that accelerates the electrons within the gas. Those electrons collide with the gas atoms and excite the atoms to excited energy levels, some of which serve as upper laser levels. Lower-lying levels, those to which higher-lying levels can transition, typically decay to the ground state faster than the higher-lying levels, thereby establishing a population inversion between some of the higher and lower levels as indicated in Figure 1.6. This inversion can be envisioned by considering that, if the lower levels drain out faster than the upper levels, there will be less population left in those lower levels than in the higher-lying levels. The laser light then occurs when the higher-lying levels decay to the lower levels while radiating photons at the wavelengths corresponding to the energy separation between the levels. In many instances the excitation is a two-step process in which the electrons first excite a long-lived or metastable (storage) level or they ionize the atom, leaving an ion of that species and another electron. In either case, that level then transfers its stored energy to the upper laser level via a subsequent collision with the laser species. The laser transitions in gaseous laser media typically occur at relatively precise, discrete wavelengths that correspond to the energy difference of inherently narrow energy levels.
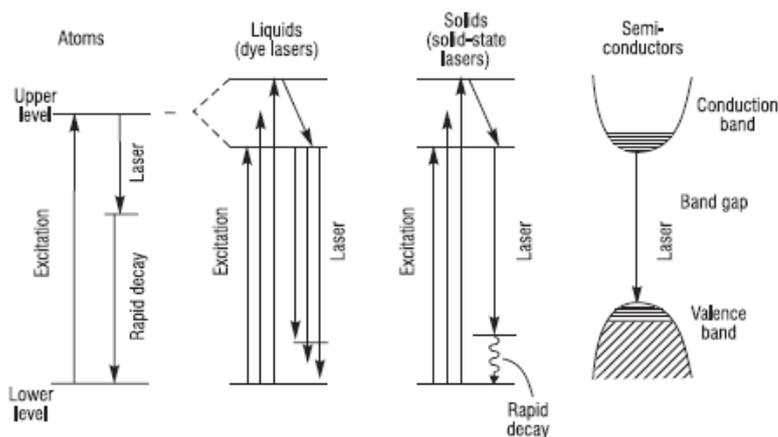
Figure 1.6 - Inversion processes in gases, liquids, solids, and semiconductors

Population inversions in liquids - Most excited energy levels in liquids decay so rapidly due to collisions with the surrounding nearby atoms or molecules that they can't stay around long enough to participate in a lasing process. There are some molecules however, namely organic dye molecules, that do have a sufficiently long lifetime in an upper energy level (of the order of 1–5 ns) so they can participate in the laser process by being excited to an upper laser level. These molecules also have the ability to radiate the energy from that level rather than lose the energy due to decay by collisions. Those molecules are the dyes that are used to color cloth and other objects that we use in our everyday life. When dissolved in a solvent such as alcohol or water, they can be concentrated in sufficient quantity to be used as a laser gain medium. In these dissolved dye solutions, electrons cannot be made to flow in the form of an electrical current within the liquid as they can in gases. Therefore the pumping of the upper laser levels must be carried out by optical means such as a flashlamp or another laser as shown in Figure 1.6. When the light is applied to the dye solution, it is absorbed at certain wavelengths by the dye as described by Equation 2, placing the dye molecules in highly excited upper laser levels. A population inversion is then produced between those levels and a very broad range of lowerlying energy levels, thereby allowing the possibility for a wide range of laser wavelengths to be produced within the gain medium. Those lower levels are not initially pumped by the light and therefore are sufficiently empty to produce the inversion. Dye lasers thus allow the possibility of wide wavelength tunability and have been used extensively in doing a variety of spectroscopic studies in which very specific laser wavelengths are desired.

Population inversions in crystalline solids and glasses - As in the case of liquids, when energy levels in solids are excited, typically by irradiating those solids with light, the levels tend to decay much more rapidly via collisions with their surrounding neighbors rather than by radiating their energy in the form of light. In a few cases, however, specific types of atoms are embedded into a transparent host material (such as a specific crystalline solid or a glass) at concentrations of up to 1 part in 100, and the atoms radiate their energy rather than decay by collisions. These specific types of atoms, such as chromium or neodymium, consist of a radiating electron surrounded by a "screen" of other electrons that protect that radiating electron from being bombarded

by collisions from neighboring atoms. The consequence is that the atoms can absorb pump light that passes through the transparent host medium and can then subsequently radiate that energy. Gemstones such as rubies fall into that category. Ruby, a desired gemstone and also the material that comprised the gain medium for the first laser, consists of chromium atoms doped into a transparent sapphire (Al_2O_3) host crystal. The color of the ruby crystal is determined by the chromium atoms, which absorb light in the blue and green regions of the spectrum and radiate in the red. When these types of laser crystals absorb light, the energy ends up in excited energy levels that serve as the upper laser level. These crystals have the property that the upper laser level has a very long lifetime before it decays by radiating when compared to all other types of laser gain media. The population inversion in most of these lasers occurs by the lower laser levels being rapidly depleted by collisions with the neighboring atoms (Figure 1.6) since these levels are not screened or protected as are the upper laser levels. An exception to this is the ruby laser in which the lower laser level is the ground state. In this case the pumping power must be excessively high in order to pump more than half of the chromium atoms into the upper laser level to produce an inversion. In these solid-state laser gain media, some of the doping atoms produce very broad excited energy levels and others have very narrow energy levels. The broad energy levels allow a broad wavelength region over which gain or amplification occurs and thus allow broad wavelength tunability of the lasers. The narrow energy levels produce lasers operating over a very narrow wavelength region or narrow bandwidth.

Population inversions in semiconductors - Inversions in semiconductors are produced when joining a p-doped semiconductor material with an n-doped semiconductor material in a similar way to that of producing a transistor to create a pn junction. The n-doped material contains an excess of electrons and the p-doped material has an excess of holes (a material with excess positive charge). When a voltage is applied across the junction, with the positive voltage on the p side, the electrons are pulled through the junction toward the positive electrode and the holes are attracted to the negative side, producing an electrical current flow across the junction. The electrons and holes meet within the junction and are attracted to each other because of opposite charges. When they meet, they recombine and emit radiation and also can produce a population inversion. This inversion occurs between energy levels located above and

below the semiconductor bandgap (Figure 1.6), the gap in energy below which the material is transparent. This energy typically corresponds to a wavelength in the infrared, and hence most semiconductors radiate in the infrared and are not transparent in the visible spectral region like glass is. However, semiconductor lasers are under development to operate in the green and blue regions of the spectrum. At very low currents, a population inversion does not occur even though recombination radiation is emitted. In fact, such nonlaser-like emission is the source of radiation from a light-emitting diode (LED). In comparison, to produce a population inversion, a very high current density is applied within the junction region. However, this high current density leads to excessive heat deposition in the material; therefore a significant part of the development of semiconductor lasers involves how to remove the heat, or to make smaller junctions so that less current is required. The material and its corresponding energy bandgap determine the laser wavelength. Equation 5 describes the way in which a beam is amplified if a population inversion exists between two energy levels such as 1 and 2, as described above. An inversion is a necessary condition for making a laser but not a sufficient condition. The exponential factor in Equation 5 must be high enough for the beam to grow and develop into the kind of narrow beam that is expected from a laser. For example, if the exponent turns out to have a value of only 0.00001, there will be no noticeable beam growth even though Equation 6 might be satisfied. The exponent of Equation 5 consists of a cross section σ_{21} that is characteristic of a specific material and also a specific radiative transition in that material. It is referred to as a cross section because it has dimensions of length^2 or area.

Bandwidth of laser gain medium - The bandwidth of the laser gain medium determines the range of wavelengths over which amplification can occur for any specific laser. This bandwidth is expressed in either a wavelength range $\Delta\lambda_G$ or a frequency range $\Delta\nu_G$. These two expressions are related by

$$\Delta\lambda_G = \frac{\lambda^2}{c}\Delta\nu_G \qquad (7)$$

in which λ is the laser wavelength and c is the speed of light. The bandwidth of the gain medium is usually determined by the bandwidth over which the spontaneous emission occurs for a given laser transition.

This bandwidth is determined by specific properties of the energy levels involved in the transitions, such as their lifetimes, how the atoms interact with other atoms, how closely the atoms are arranged, etc. Typically, atomic gas lasers have bandwidths of the order of 1 GHz (109 Hz). Molecular lasers have bandwidths that are sometimes a factor of 10 to 10,000 larger than that due to the closeness in wavelength of several molecular transitions that overlap in frequency. Solid-state lasers can have relatively narrow bandwidths of the order of 100 GHz in cases such as the Nd:YAG laser, or very wide bandwidths, of the order of 100 THz (1014 Hz) in the case of the titanium sapphire laser. Semiconductor lasers have bandwidths typically of 1013 Hz. Comparisons of the laser gain bandwidths for the HeNe, Nd:YAG, and Ti:Al$_2$O$_3$ lasers are shown in Figure 1.7. These various bandwidths are not the bandwidths of the laser beam that emerges from the amplifier but do indicate the range over which amplification can occur. Laser mirror cavity properties primarily determine the bandwidth of the emerging laser beam, as will be described later under laser beam properties.
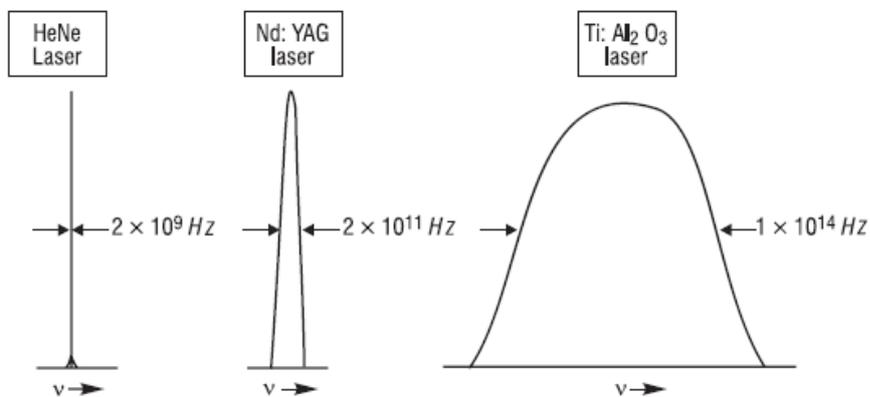
Figure 1.7 - Laser gain bandwidths for the HeNe, Nd:YAG, and Ti:Al2O3 lasers

1.2.2 Laser pumping sources

Laser pumping sources are the means by which energy is transferred into the laser gain medium to produce the required population inversion

ΔN_{21}. These pumping sources generally consist of either electrons flowing within the medium or light being absorbed by the medium.

Electron pumping - Electron pumping is used primarily in gaseous or semiconductor gain media. In gases, many electrons are produced when a few initial electrons within the gain medium are accelerated by an electric field within the medium and these many electrons then collide with neutral atoms, exciting those atoms to higher-lying energy levels and even ionizing some of the atoms (removing an electron). The freed electrons are also accelerated, producing an avalanche of electrons and therefore an electrical current within the medium. The electrons lose their energy by transferring it to the atoms during the collision process. Some of the lasers operate on a pulsed basis, applying a large amount of current for a short period of time. Others operate on a continuous (cw) basis, using a much smaller but continuous current. In semiconductors, the electrons flow through the semiconducting material by applying a voltage across the pn junction with the positive voltage on the side of the p-type material. This leads to recombination radiation when the electrons combine with the holes in the junction. The heat loading of the semiconductor limits the current.

Optical pumping - Optical pumping of lasers generally applies to the pumping of liquid (dye) lasers and to dielectric solid-state lasers and is provided by either flashlamps or other lasers. The most common types of flashlamps used for pumping lasers are narrow, cylindrical quartz tubes with metal electrodes mounted on the ends, filled with a gaseous species such as xenon that serves as the radiating material within the lamp. A voltage is applied across the electrodes of the flashlamp and current flows through the gas, populating excited levels of the atoms within the gas that radiate and produce intense light emission. The process is similar to that of electron excitation of lasers described above except that a population inversion is not produced and the radiating material of the lamp radiates via spontaneous emission, rather than by stimulated emission as in the case of a laser gain medium. The pumping wavelength of the flashlamp is determined by the gaseous medium inserted within the flashlamp tube. Xenon is the most common species because of both its radiating efficiency and its emission of a broad spectrum of wavelengths from which to choose in matching the lamp emission to the pumping absorption bands of the laser. Examples of flashlamp configurations for pumping lasers are shown tin Figure 1.8. Figure 1.8a shows the flashlamp

in the form of a helix wrapped around the laser rod. Figures 5-9b and 5-9c show the flashlamp inserted into an elliptically-shaped or circularly-shaped elongated laser cavity. In Figure 1.8b the flashlamp is located at one focus of the ellipse and the laser rod to be pumped at the other focus of the ellipse. Figure 1.8d shows two flashlamps used in a double elliptical cavity, one of the most favorable arrangements, with the laser rod in the center. Sometimes the laser mirrors are coated onto the ends of the laser rod and sometimes they are mounted externally to the rod, along the longitudinal axis of the cavity.
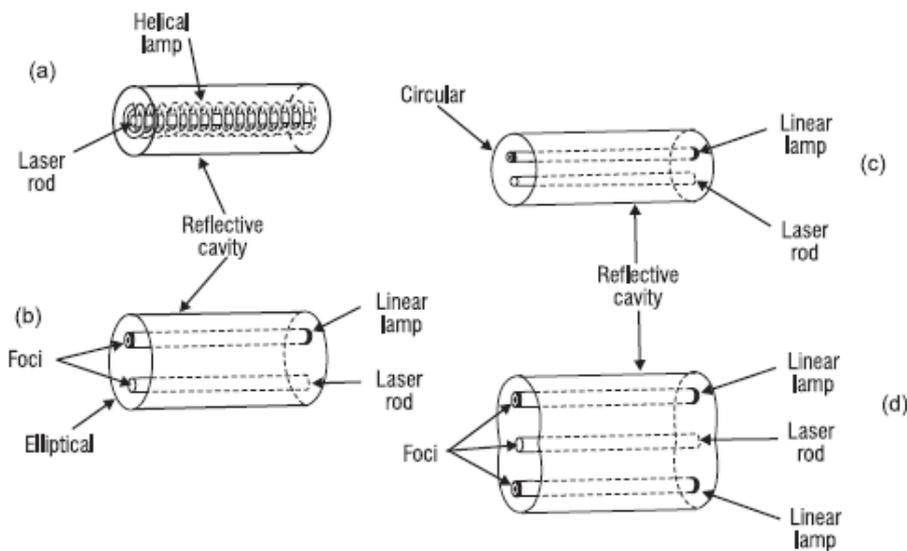
Figure 1.8 - Flashlamp configurations for pumping lasers

Laser pumping is used in cases in which the pumping energy must be concentrated into a relatively small volume or for a very short time, or if the pumping wavelength must be provided over a fairly narrow-wavelength bandwidth. Pumping lasers include the argon ion or doubled Nd:YAG cw lasers for pumping titanium-sapphire lasers, excimer lasers for pumping dye lasers, and gallium arsenide semiconductor lasers for pumping Nd:YAG lasers. In most cases the laser is focused to a relatively small gain region, a line focus for dye lasers and a spot focus for the other lasers. Two examples of diode pumping of Nd:YAG lasers are shown in Figure 1.9.
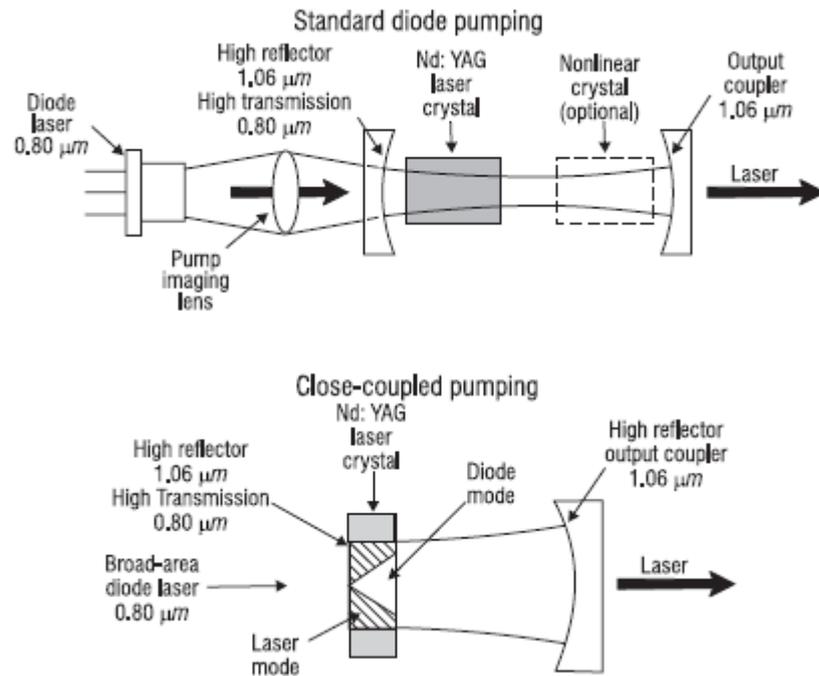
Figure 1.9 - Examples of laser diode pumping of Nd:YAG lasers

1.2.3 Laser beam properties

Laser beam properties such as direction and divergence of the beam, the beam profile, and the wavelength and frequency characteristics of the laser within the wavelength region of the laser gain bandwidth are determined largely by the laser mirrors. The factors determining those properties include mirror curvature, surface quality, and reflectivity as well as separation and location, assuming that the structure holding the mirrors is a secure, vibration-free structure. The unique electromagnetic wave properties produced by the mirrors are referred to as modes. Before discussing these mirror properties, we must consider the shape of the gain medium and the beam growth to the point of beam saturation.

Shape of gain medium - The goal of constructing a laser is to capture most of the spontaneous emission that is normally emitted in all directions within the gain medium and redirect it into a single direction. This is done with the assistance of the gain or amplification that can be initiated within

the medium. It is desirable to have the gain medium be of an elongated shape so that the gain, which is length dependent, will operate primarily in that one elongated direction. Hence, most laser gain media are long, narrow devices with mirrors located at the ends.

Growth of beam and saturation - If significant gain is provided along the length of the gain medium, the spontaneous emission emitted in the elongated direction will grow at a rate dependent upon the amount of gain available as it moves through the length of the medium. The emission that starts at one end and transits to the other end will have grown by a factor of between 0.02 (2%) and 10 (1,000%) in a single pass, depending upon the type of laser. However, even the high factor-of-10 growth available in some lasers is not sufficient to produce a powerful unidirectional laser beam in one pass. Hence, mirrors are placed at both ends of the medium, forming a cavity to redirect the beam back and forth through the amplifier and thereby allow the beam to continue to grow until a point of beam saturation is achieved. At somewhere between 2 passes (dye lasers) and 500 passes (HeNe lasers), the beam will have become so intense within the laser cavity that there won't be sufficient atoms in the upper laser level within the gain medium to accommodate all of the impinging photons. This is the condition of beam saturation, and the intensity of the beam is known as the saturation intensity. The condition of saturation occurs when the exponent of Equation 5 ($\sigma_{21}\Delta N_{21}L$) reaches a value of approximately 12. In this saturation, the length L is the effective length of many passes through the amplifier so we will define that length as LT. Hence, we have the condition to reach saturation as ($\sigma_{21}\Delta N_{21}L_T \cong 12$) or ($g_{21}L_T \cong 12$). At that point the beam will have grown by a factor of approximately $e^{12} = 1.6 \times 10^5$ according to Equation 5. When it reaches that intensity it will settle down to a stable value (as long as the pumping continues) in which the conversion from pump power to laser photons reaches an equilibrium balance. In the case of the HeNe laser described above, that requires 500 passes through the amplifier. If the amplifier length is 20 cm, the effective length in Equation 5 is 500×20 cm or 100 m. Hence, the beam travels through 100 m of amplifier length before it reaches saturation. If more pump power is applied, above the value where the saturation intensity is reached, more laser power will be produced and will be available through the output mirror of the laser. The condition for a population inversion and thus amplification within the amplifier was given by Equation 6 ($N_2/N_1 > 1$).

However, even though gain might exist within the amplifier, the laser still might not develop a beam if the gain is not sufficiently high to overcome losses within the laser cavity. The laser mirrors won't have 100% reflectivity and there might be additional losses such as scattering and reflective losses at windows and other optical elements placed within the cavity. Hence, a simple expression is used to determine the threshold condition for a laser beam to develop, based upon the laser cavity characteristics. For a laser in which the amplifier length has a value of L and the mirrors have identical reflectivities R, with no other losses in the cavity, the threshold condition for the gain coefficient g is given as

$$ g = \frac{1}{2L} \ln \frac{1}{R^2} \tag{8} $$

which has dimensions of 1/length. Any value of g higher than that given by Equation 8 will produce a laser beam within the cavity. For a more complex laser cavity in which the mirrors have different reflectivities R_1 and R_2, and a1 and a2 represent other losses within the cavity (beyond the amplifier), the expression for the threshold gain g is given as

$$ g = \frac{1}{2L} \ln \left[\frac{1}{R_1 R_2 (1 - a_1)(1 - a_2)} \right] + \alpha \tag{9} $$

The term α represents a potential absorption loss within the amplifier itself, which is present in only a few types of lasers. It is a distributed loss expressed in the same units as g or (1/length). For example, in solid-state lasers it is termed excited state absorption.

Longitudinal cavity modes - When the beam is developing within the mirror cavity, traveling back and forth, certain wavelengths within the gain bandwidth of the laser tend to be more enhanced than others. These are wavelengths (or frequencies) in which the light beam in the cavity forms a standing wave. Such an effect occurs when an exact number of half-wavelengths of the light fit within the separation distance between the mirrors. Typically there will be several hundred thousand wave peaks for each standing wave that occurs within the cavity. Hence, each standing wave must have a wavelength such that an integral number of oscillating waves fits in the space separating the mirrors. If more than one standing wave is present, each standing wave (longitudinal mode) will be

separated in frequency from the next one by a fixed exact amount that depends upon the laser cavity length d. That frequency separation Δv between longitudinal modes can be obtained by dividing the speed of light c by twice the cavity length or

$$\Delta v = \frac{c}{2d} \tag{10}$$

In Figure 1.10, several of these modes are shown occurring within the frequency bandwidth of a typical gas laser. Typically, the separation in frequency is of the order of 500 MHz (5×10^8 Hz) whereas the laser frequency itself is of the order of 500,000,000,000,000 Hz (5×10^{14} Hz). For example, two of these discrete standing waves might have frequencies of 500,000,000,000,000 Hz and 500,000,500,000,000 Hz, separated in frequency by 500 MHz.

Max

Gain
bandwidth
of amplifier

0

Max

Cavity
reflectivity
vs frequency

0

Max

Laser
output

0

Frequency
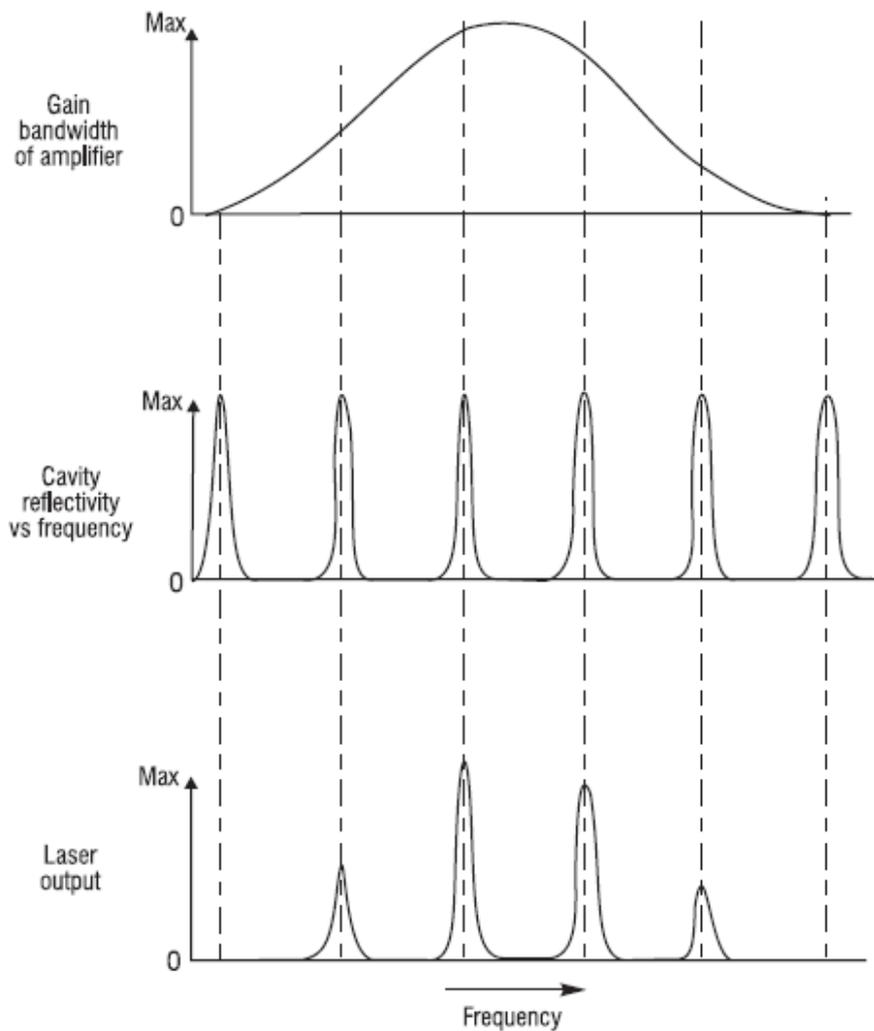
**Figure 1.10 - Several longitudinal modes are shown occurring within the
gain bandwidth of a typical gas laser**

Each discrete standing wave is referred to as a longitudinal mode
associated with the laser cavity. Figure 1.11 shows two such modes
within a cavity. There will always be at least one longitudinal mode and
there could be many more, depending on the frequency or wavelength
bandwidth of the laser gain medium. If more than one longitudinal mode
is being generated, they will be indistinguishable unless a spectrum

analyzer is used to analyze the beam. They all travel in the same direction, and their color will be indistinguishable because their wavelengths (frequencies) are so similar.
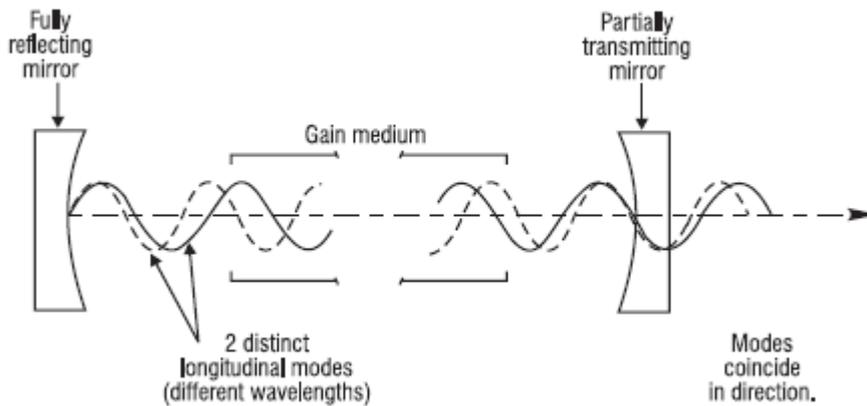
Figure 1.11 - Two distinct longitudinal modes operating simultaneously in the same laser cavity

The frequency width of a single longitudinal mode can be very narrow, typically in the range of 106 to 108 Hz, determined by the mirror reflectivity (higher-reflecting mirrors produce narrower bandwidths) and by the cavity stability (free of vibrations).

Transverse modes - The presence of more than one longitudinal mode involves many light beams traveling exactly the same path through the amplifier but differing in wavelength depending upon the total number of wave cycles that fit between the mirrors. Contrary to this, different transverse modes involve slightly different optical paths through the amplifier and thus have slightly different directions when they emerge from the laser as shown in Figure 1.12. Because of the different optical path lengths, they also have slightly different frequencies. Each of these stable modes evolves because the light traveling that particular pathway recurs exactly from one round trip of the beam to the next, therefore developing into a steady beam. Each transverse mode traveling over its unique path might also consist of several longitudinal modes separated in frequency according to Equation 10.
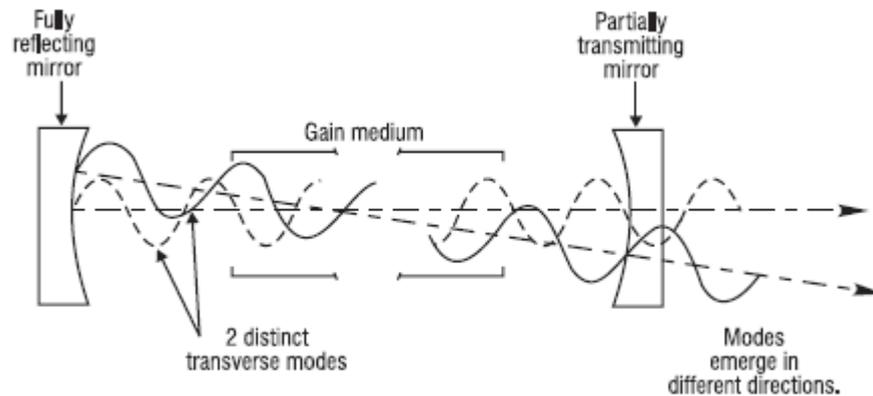
Figure 1.12 - Two transverse modes occurring simultaneously within a laser cavity

The lowest-order transverse mode, known as the TEM_{00} mode, travels down the central axis of the laser gain medium. Higher-order modes have slightly diverging beams as shown in Figure 1.12. The TEM_{11} mode, for example, if it were the only mode present, would appear as a doughnut-shaped beam when projected onto a screen. Complex patterns can be present if several transverse modes are operating. In most cases, closely located transverse modes differ in frequency by a smaller value than do adjacent longitudinal modes that follow the same path through the amplifier. The TEM_{00} mode has a beam-intensity profile in the direction transverse to the direction of propagation that is described by a Gaussian function as given by the following expression.

$$I = I_0 e^{-\frac{2r^2}{w^2}}$$
(11)

where I_0 is the intensity on the beam axis at any location, r is the perpendicular distance from the beam axis, and w is defined as the beam waist. This beam profile is shown on the left side of Figure 1.13. The beam waist, varying along the axis of the laser, is defined such that the intensity has fallen to $1/e^2$ of the intensity on axis. It turns out that 86.5% of the energy is contained within the beam radius in which r = w. The TEM_{00} mode is often the desired mode because it propagates with the least beam divergence and can be focused to the tightest spot. It can generally be obtained by placing an adjustable aperture within the laser

cavity and decreasing the aperture diameter until only the TEM_{00} mode remains.
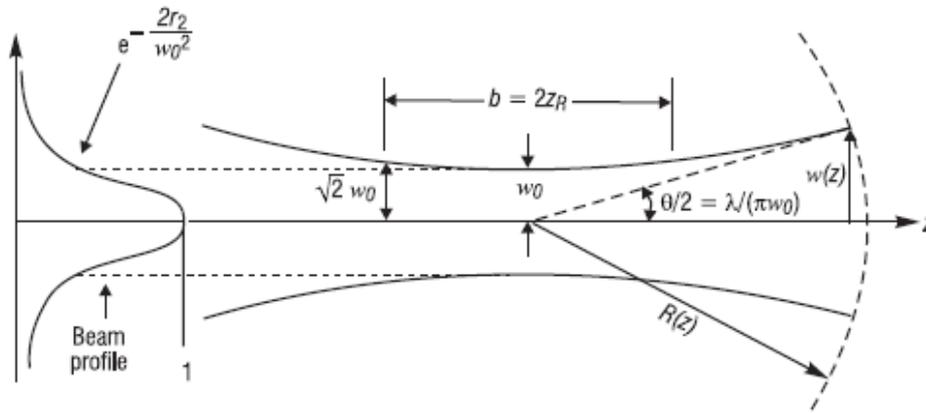
Figure 1.13 - A diagram showing some of the parameters of a Gaussian laser beam (TEM00 mode)

Gaussian beams have a minimum beam waist w_0 that usually occurs somewhere between the laser mirrors. The beam then gradually expands from that location. If the laser mirrors have the same radius of curvature, the minimum beam waist occurs exactly halfway between the mirrors. If the minimum beam waist is known, the beam waist $w(z)$ at any distance z from where the minimum occurs can be determined from the following equation (provided the beam does not interact with any type of optical element that would change the beam in any way).

$$w(z) = w_0 \left[1 + \left(\frac{\lambda z}{\pi w_0^2} \right)^2 \right]^{1/2} \tag{12}$$

where λ is the wavelength of the beam. This is diagrammed in Figure 1.13. The expanding beam has a curved wavefront with a radius of curvature R(z) given by

$$R(z) = z \left[1 + \left(\frac{\pi w_0^2}{\lambda z} \right)^2 \right] \tag{13}$$

The beam angular spread Θ in radians at distances well beyond the laser mirrors can be expressed as

$$\Theta = \frac{2\lambda}{\pi w_0} \tag{14}$$

as shown in Figure 1.13. This angular divergence Θ can be approximately determined by measuring the beam diameter at a known distance from the laser (by projecting the beam onto a screen) and then finding the ratio of the beam radius (half the diameter) to the distance from the laser. From Equation 14, it can be seen that a larger w_0 and/or a shorter wavelength λ gives a smaller angular beam divergence.

Also shown in Figure 1.13 is the value of $z = z_R$ such that

$$z_R = \frac{\pi w_0^2}{\lambda} \tag{15}$$

This value z_R is referred to as the Rayleigh range and is considered the depth of focus for a Gaussian beam. Twice the value of z_R or $b = 2\,z_R$ is known as the confocal parameter. At a distance z_R in either direction from the location of the minimum beam waist w_0, the value of the beam waist has increased to $\sqrt{2}\;w_0$. When a confocal laser cavity is set up the diameter of the beam at the mirrors will thus have the value of $2\sqrt{2}\;w_0$. For laser cavities in which the mirrors have the same radii of curvature, the expression for w_0 can be given as

$$w_0 = \left\{ \frac{\lambda}{2\pi} [d(2R - d)]^{1/2} \right\}^{1/2} \tag{16}$$

If the radius of curvature is equal to the separation between mirrors, or $R = d$, the cavity is known as a confocal resonator. For this case the expression for w_0 then simplifies even further to

$$w_0 = \left(\frac{\lambda d}{2\pi} \right)^{1/2} \tag{17}$$

Another very common laser cavity arrangement is known as the semi-confocal resonator cavity. This case uses a curved mirror and a flat mirror (infinite radius of curvature) with the mirror separation being half the radius of curvature. This, in effect, is one-half of the confocal resonator as described above because it folds half of the resonator back on itself by using a flat mirror at the halfway location. This is a common resonator to obtain a parallel beam at the output of the laser, if the output mirror is the flat mirror.

1.3   Laser properties related to applications

1.3.1 Collimation

Collimated light is light in which all of the light rays or waves are traveling in a specific direction and hence they are all parallel to each other. Lasers produce the most collimated light of any type of light source. Such collimated light is used for reference beams in construction, leveling and grading land, alignment of pipe such as sewer pipe, and sending light over long distances without suffering significant divergence, and in laser pointers. Producing the most collimated light, in other words the least divergent light, is determined by the cavity mirror properties including the radii of curvature of the mirrors and the separation between mirrors as indicated in Equations 12, 13, and 14. For the smallest beam divergence, w_0 must be large, as you can see from Equation 14. Also, the rays of the laser beam are the most parallel when the beam is at the location of the minimum beam waist w_0 as described in Equations 12, 15, and 16.

1.3.2 Monochromaticity

Monochromaticity refers to how pure in color (frequency or wavelength) the laser beam is or, in other words, how narrow the laser beam frequency bandwidth is. Note that this is essentially $N\Delta v$ as described above in the mode-locking discussion if the laser is lasing with more than one longitudinal mode. If the laser is operating in a single longitudinal mode, as most solid-state and semiconductor lasers do, the

actual laser linewidth can be significantly narrower, the width of a single longitudinal mode beam. For most applications requiring a single narrow wavelength, most lasers would normally provide a sufficiently narrow frequency output bandwidth, of the order of 10^9–10^{11} Hz. This would represent a bandwidth that is less than 0.1% of the frequency or wavelength of the beam itself (or even smaller in most instances). However, in some applications, such as in remote sensing or in establishing a new frequency standard, a much narrower linewidth is required. Linewidths of the order of 1 MHz (10^6 Hz) or less can be obtained by operating with a single longitudinal and single transverse mode (TEM_{00}). The narrowing is enhanced by choosing highly reflecting mirrors, constructing a very stable mirror cavity in conjunction with the amplifier by eliminating vibrations of the mirrors and other cavity elements, and providing temperature stability.

1.3.3 Coherence

Coherence refers to the how much in step or in phase various portions of a single laser beam are. The closeness in phase of various portions of the laser frequency bandwidth is referred to as temporal or longitudinal coherence. The closeness in phase of different spatial portions of the beam after the beam has propagated a certain distance is referred to as spatial or transverse coherence. This phased relationship determines how readily the various portions of the beam can interfere with each other, after the beam has propagated a specific distance, to produce such effects as diffraction (bending) of light and related applications such as holography. Typically, applications involve dividing the beam into two or more beams that travel different lengths or pathways and are then recombined. When they are recombined they will interfere with each other, producing the desired effect if those parts are still in phase (coherent); if they are no longer in phase, the effect will not occur. The coherence length is used to describe the beam propagation distance over which the beams stay in phase. For longitudinal or temporal coherence, the coherence length l_C is related to the wavelength λ and the total frequency bandwidth of the laser $\Delta \nu_L$ by

$$l_c = \frac{\lambda^2}{\Delta\lambda} \tag{18}$$

$\Delta\lambda$ is the actual bandwidth of the laser beam given in wavelength units.
For transverse or spatial coherence, the transverse coherence length l_t is
related to the laser wavelength λ, the laser source diameter at its origin s,
and the distance r the beam has propagated from its origin, by the
following relationship.

$$l_r = \frac{r\lambda}{s} \tag{19}$$

1.3.4 Intensity and radiance

Intensity or irradiance is the power of the laser beam divided by the
cross-sectional area of the beam. It is thus typically given in watts per
square centimeter (W/cm^2). It is a measure of the amount of energy that
can be applied to a specific region within a given amount of time. It is one
of the two most important parameters in using the laser for materials
processing applications such as welding, cutting, heat treating, ablating,
and drilling, or for laser surgery. The other important parameter is the
laser wavelength, since the amount of absorption of all materials,
including biological materials, is dependent upon the wavelength of the
light. In some instances a deep penetration of the beam is desired, for
example in doing processes that must be carried out quickly. In that
situation, a laser wavelength in which the material has a relatively low
absorption would be selected. Other applications might require a shallow
penetration in order to control the quality of the edge to be left after the
process is completed, such as in some surgical processes or in drilling
very small holes. Thus, a wavelength region of high absorption would be
chosen for the laser. A general rule is that absorption is very high for most
materials at ultraviolet wavelengths and decreasing at longer wavelengths.
However, this does not hold true for all materials or for all wavelengths.
Many materials have high absorption peaks at specific wavelengths that
could occur anywhere in the spectrum, so one must be careful to obtain
the absorption versus wavelength curves for the desired material before

choosing the specific laser. In all instances where high beam intensity is desired, the availability of the laser with sufficient intensity at that wavelength must be considered. Not all wavelengths with such intensity are possible. There are, however, lasers such as the CO_2 laser in the middle infrared (10.6 μm); the Q-switched Nd:YAG laser in the near infrared (1.06 μm) and frequency-doubled Nd:YAG to the green (530 nm); the copper vapor laser in the green (510 nm) and yellow (578 nm); and the ultraviolet excimer lasers including the XeF laser (351 nm), XeCl laser (308 nm), KrF laser (at 248 nm), ArF laser (193 nm), and F_2 laser (157 nm). For various aspects of materials processing, the beam must have an intensity in the range of 108–109 W/cm^2. Radiance is a parameter that includes the beam intensity (W/cm^2) and takes into account the beam divergence angle. The divergence angle is generally given in steradians, which is a three-dimensional angular measurement as opposed to the term degrees, which describes angular spread in only two dimensions (in a plane). A complete sphere contains 4π steradians. Hence, radiance is given in units of watts per unit area per unit solid angle or (W/cm^2-sr). Laser beam divergence is usually given in milliradians (mr) because of the very low divergence of most lasers. The approximate beam divergence in radians can be obtained by measuring the laser beam diameter at a specific, relatively long distance from the laser and dividing it by the square of the distance to where the measurement is made. Radiance becomes useful when a beam must be propagated over a reasonable distance before it is used or where the divergence can affect the focusing ability of the beam. Since most materials applications do not involve the tightest focusing possible for a given beam, intensity is usually the more important parameter.

1.3.5 Focusability

Many applications of lasers involve their ability to be focused to a very small spot size. Perhaps one of the most demanding applications is in focusing the small diode laser in a compact disk player. To store as much information as possible on each disk, that information must be included in the smallest grooves possible on the disk. The width of the grooves is determined by the ability of a laser beam to access a single groove without overlapping into adjacent grooves. Hence, the diameter of the

spot size to which the laser beam can be focused becomes a very important parameter. The smallest diameter that can be obtained with a focused laser, assuming that a single TEM$_{00}$ mode can be obtained from the laser, is approximately the dimension of the wavelength of the laser and is given by the following expression

$$d_{min} \cong \frac{4\lambda(\frac{f}{d_l})}{\pi} \qquad (20)$$

in which the f/d$_l$ is the focal length of the lens used for the focusing divided by the useful diameter of the lens, the same notation as on camera lenses. If the laser beam is less than the actual lens diameter, the beam diameter is used instead of the lens diameter in determining the f/d$_l$. In other words, a laser operating in the visible spectral region with a wavelength of the order of 500 nm could be focused to a size of less than one hundredth the width of a human hair! The effective f/d$_l$ focusing lens (ratio of focal length to laser beam diameter intercepted by the lens) must be of the order of unity to obtain such a small focus. Most lasers, however, can be focused relatively easily to spot diameters of the order of 0.1–0.2 mm. Extra care must be taken in terms of beam quality (mode quality) and lens focal length to obtain smaller spot diameters.

1.4   Examples of common lasers

1.4.1 HeNe

The helium-neon laser (HeNe) was the first gas laser. The most widely used laser wavelength is the red wavelength (632.8 nm) with a cw power output ranging from 1 to 100 mW and laser lengths varying from 10 to 100 cm. HeNe lasers can also be operated at the 543.5-nm green wavelength and several infrared wavelengths. Initiation of a relatively low electrical current through a low-pressure gas discharge tube containing a mixture of helium and neon gases produces the population inversion. With this gas mixture, helium metastable atoms are first excited by electron collisions with helium ground-state atoms. This energy is then

transferred to the desired neon excited energy levels, thereby producing the required population inversion with lower-lying helium energy levels.

1.4.2 Arogn ion and Krypton ion

The argon ion laser and the krypton ion laser provide a wide range of visible and ultraviolet laser wavelengths. They produce cw output at wavelengths ranging from 275 to 686 nm and powers of up to tens of watts. Running a dc current through a long, narrow-bore plasma discharge tube filled with a low-pressure (0.1 torr) argon or krypton gas produces the population inversion. The argon atoms must be ionized to the first through third ionization stages to reach the appropriate energy levels for laser action. As a result, these lasers are relatively inefficient but still extremely useful for certain applications because of their short wavelengths.

1.4.3 HeCd

The helium cadmium laser (HeCd) operates continuously (cw) in the blue (441.6 nm) and ultraviolet (354 and 325 nm) portions of the spectrum with powers ranging from 20 to 200 mW and laser lengths of 40–100 cm. The population inversion in the amplifier region is produced by heating metallic cadmium to a vaporized state in a narrow-bore quartz discharge tube, mixing it with helium gas, and running an electrical discharge current of up to 100 mA through the tube. The excitation mechanisms include Penning ionization (helium metastable atoms colliding with neutral Cd atoms and exchanging energy), electron collisional ionization, and photoionization from strong, short-wavelength radiation originating within the helium atoms. The laser uses an effect known as cataphoresis to transport the cadmium atoms through the discharge and thereby provide the necessary uniform cadmium distribution within the gain region.

1.4.4 Copper vapor

The pulsed copper vapor laser (CVL) provides high average powers of up to 100 W at green (510 nm) and yellow (578 nm) wavelengths at very

high repetition rates of up to 40 kHz and pulse durations of 10–50 ns. The copper is heated within the laser gain region to temperatures of up to 1600 °C in 2–10-cm-diameter ceramic tubes typically of 100–150 cm in length. The lasers are self-heated such that most of the energy provided by the discharge current provides heat to bring the plasma tube to the necessary temperature. Excitation occurs by electrons colliding with neutral copper atoms to excite them to the relevant laser-related energy levels.

1.4.5 CO_2

The carbon dioxide laser (CO_2), operating primarily in the middle infrared spectral region around 10.6 μm, is one of the world's most powerful lasers, producing cw powers of over 100 kW and pulsed energies of up to 10 kJ. It is also available in smaller versions with powers of up to 100 W from lasers the size of a shoe box. These lasers operate in a gas discharge in mixtures of helium, nitrogen, and CO_2 gases. Electron collisions with the nitrogen molecules within the discharge produce metastable energy levels. The energy contained in those levels is subsequently transferred by collisions to the CO_2 molecule, where the population inversion is produced. This is one of the most efficient lasers, with conversion of input electrical power to laser output power of up to 30%.

1.4.6 Excimer

Excimer lasers consist of mixtures of noble gas atoms such as argon, krypton, and xenon with reactive gases such as fluorine or chlorine operating in a special type of high-pressure gaseous discharge. They are therefore also known as rare gas-halide lasers. The actual laser species is an excited-state molecule containing a combination of the two types of atoms, such as ArF, KrF, XeF, and XeCl. The term excimer results from a contraction of the words "excited state dimer," which indicates the excited-state nature of the lasing molecule. The lasers operate primarily in the ultraviolet spectral region with wavelengths at 193 nm (ArF), 248 nm (KrF), 308 nm (XeCl), and 351 nm (XeF). The laser output consists of 10–50-ns pulses typically of 0.2 to 1 J/pulse at repetition rates of up to 1 kHz. These lasers are relatively efficient (1–5%) and are of a size that can

fit on a desktop. The excitation occurs with electrons within the discharge colliding with and ionizing the rare gas atoms while at the same time dissociating the halide molecules into either F or Cl atoms to form negative halogen ions F^- and Cl^-. The negative halogen ions and positive rare gas ions readily combine in an excited state to form the laser species since they are of opposite charge and hence attract each other.

1.4.7 Organic dye

Dye lasers have the advantage of wide tunability in wavelength. When changing from one dye to another, the total wavelength region that can be covered ranges from 320 to 1500 nm. The gain medium for dye lasers consists of a solvent such as alcohol or water within which an organic dye is dissolved in a typical concentration of 1 part in ten thousand. If a diffraction grating or prism is used to replace one of the laser mirrors, the grating can be rotated to tune the laser wavelength over the spectrum of the dye. Each dye has a tunable gain bandwidth of approximately 30–40 nm with a linewidth as narrow as 10 GHz or less. Dye lasers are available in either pulsed (up to 50–100 mJ/pulse) or cw (up to a few W) in tabletop systems that are pumped either by flashlamps or by other lasers such as frequency-doubled or -tripled YAG lasers or argon ion lasers. Most dye lasers are arranged to have the dye mixture circulated by a mechanical pump into the gain region from a much larger reservoir because the dyes degrade at a slow rate due to the excitation (optical pumping) process. Dye lasers, with their broad gain spectrum, are particularly attractive for producing ultrashort light pulses by a mode-locking process as described earlier. The shortest pulses ever generated are 5 thousandths of a trillionth of a second (5×10^{-15} s).

1.4.8 Ruby

The ruby laser, which lases at the extreme red end of the visible spectrum at 694 nm, was the very first laser demonstrated. It consists of a crystalline sapphire (Al_2O_3) host material into which chromium atoms (the lasing species) are infused (doped) at a concentration of up to 0.05% by weight. The energy-level arrangement of the ruby laser, with the ground state as the lower laser energy level, makes for a very ineffective

pumping process, in which very large amounts of pump light are required before gain is achieved. Therefore, this laser is not as efficient as other solid-state lasers and is not used much anymore.

1.4.9 Nd:YAG and Nd:glass

Neodymium is a very effective laser species when doped into either yttrium-aluminum-garnet (YAG) or glass host materials. The primary laser wavelength is at 1.06 μm for YAG and 1.05 μm for glass. The lasers are optically pumped either by flashlamps or by other lasers (especially GaAs semiconductor diode lasers). YAG is a very attractive host material for Nd because it has a high thermal conductivity and is a robust material, and hence the laser can produce high average-power output without having the crystal break. The Nd:YAG laser produces cw powers of up to 250 W and pulsed energies of up to 1 J/pulse.

1.4.10 Ti:Al$_2$O$_3$

Another class of solid-state lasers is the broad-bandwidth, tunable lasers. The most well-known and used laser in this category is the titanium-sapphire laser, Ti: Al$_2$O$_3$, consisting of titanium atoms doped into a sapphire (Al$_2$O$_3$) host at a concentration of up to 0.1% by weight. This laser operates over a wavelength ranging from 660 nm to 1,180 nm (1.08 μm), which gives it a gain bandwidth of 520 nm, the largest of any laser except perhaps the free-electron laser (a laser generated by an oscillating beam of high-energy electrons). This large bandwidth allows for large tunability as well as very short pulse production via mode-locking. It is also the one solidstate laser that has a much shorter upper-level lifetime than most other solid-state lasers, just under 4 μs, which makes it difficult to pump with flashlamps and also difficult to Q-switch. Hence, this laser is typically pumped with other lasers such as the argon ion laser or the doubled Nd:YAG laser. Ti:Al$_2$O$_3$ lasers are used in infrared spectroscopy of semiconductors, laser radar, rangefinders, and remote sensing and in medical applications such as photodynamic therapy. They are also used to produce short pulses of X rays by focusing high-intensity pulses onto a solid target from which a tiny, high-temperature, high-density plasma is produced that radiates large quantities

of X rays. Other lasers in this broadband, tunable category include the alexandrite laser operating at 700 nm to 820 nm and the chrome-doped LiSAF laser, operating at 780 nm to 1010 nm.

1.4.11   Erbium fiber

Fiber lasers were first operated in Nd-doped glass fibers, but the fiber laser of major current interest is the erbium-doped fiber laser operating at 1.4 to 1.6 μm. This fiber laser can be spliced into a normal transmitting optical fiber, and, when optically pumped with a semiconductor laser at either 980 nm or 1.48 μm, it provides amplification to a communication signal that is being transmitted through the fiber. The pump light is fed into the fiber line - with a beam-combining device - thereby merging with the signal. This laser amplifier is especially useful in undersea optical fiber cables transmitting phone and data information between continents. More recently, it has also been used in local area networks and other shorter-distance communication applications. Several of these amplifiers must be installed equally spaced within a fiber when transmitting a message from America to Europe, for example. The amplifier bandwidth allows for a technique referred to as WDM (wavelength division multiplexing), which involves sending many separate signal beams at slightly different wavelengths through the same fiber, each of which is amplified by the single erbium-doped fiber amplifier. Hence, the data volume is increased significantly without having to install more fiber communication lines.

1.4.12   Semiconductor lasers

Semiconductor lasers are small, very efficient lasers with dimensions of less than a millimeter. The wavelengths of commercial lasers range from approximately 600 nm in the red to 1.6 μm in the near infrared. Lasers in the blue and green are also under advanced development, but very few are available commercially. These lasers consist of small semiconductor crystals grown such that they can be cleaved in short segments of approximately 0.5 mm in length. The cleaving is done in a direction perpendicular to the laser axis, leaving a surface (facet) at each end of the gain medium that serves as a mirror. No reflective coatings are

generally required; the cleaved surface itself serves to provide a reflectivity of the order of 35% or more from each of the two mirror surfaces, which is ample due to the very high gain or amplification present in the laser. Because of the short separation between mirrors, it is generally possible to obtain laser operation on only one longitudinal mode. Also, because of the short cavity length, the laser operates in a highly multi-transverse-mode output with a high angular divergence beam. To obtain single TEM_{00}-mode operation, it is necessary to coat the two end facets of the laser with an antireflection coating at the laser wavelength. Then an external mirror cavity can be installed with the appropriate mirror radii and reflectivity, as well as a suitable aperture on axis to restrict beam spread. Semiconductor lasers are mass produced by depositing various layers of p- and n-doped material, insulating material, and metal contact layers by lithographic techniques. The most common semiconductor lasers are heterostructure lasers in which additional layers of different materials of similar electronic configurations are grown adjacent to the pn junction. This helps confine the electrical current flow to the junction region in the direction perpendicular to the layers, thus minimizing the required current, energy deposition, and heat loading in the devices. The laser mode in the transverse direction is controlled either by gain guiding, in which the gain is produced over a specific narrow lateral extent determined by fabrication techniques, or by index guiding, in which the index of refraction in the transverse direction is varied to provide total internal reflection of the guided mode. Quantum-well lasers are semiconductor lasers that have a very thin gain region in the direction perpendicular to the layers, of the order of 5–10 nm. The laser gain bandwidth is significantly reduced due to a quantum effect. The gain coefficient remains the same, but the volume over which the energy deposition occurs is confined to an even smaller region. This significantly reduces the threshold current without significantly sacrificing laser output power. Because of their low threshold current and their low power consumption, quantum-well lasers are presently the most commonly used semiconductor lasers. The largest applications of semiconductor lasers are in communication, in which the laser provides the signal, and in compact disk players, in which the laser is focused into the disk grooves and reflected to detect the digitally coded information. They are also used in high-speed printing systems and laser pointers and as pump sources for solid-state lasers (mainly Nd:YAG).

1.5 Disk laser

The thin-disk laser (sometimes called thin-disc laser or active-mirror laser) is a special kind of diode-pumped high-power solid-state laser, which was introduced in the 1990s by the group of Adolf Giesen at the University of Stuttgart, Germany. The main difference from conventional rod lasers or slab lasers is the geometry of the gain medium: the laser crystal is a thin disk, where the thickness is considerably smaller than the laser beam diameter. The heat generated is extracted dominantly through one end face (Figure 1.14) in the longitudinal rather than in the transverse direction. The cooled end face has a dielectric coating which reflects both the laser radiation and the pump radiation. The thin disk is also often called an active mirror, because it acts as a mirror with laser gain. Within the laser resonator, it can act as an end mirror or as a folding mirror. In the latter case, there are two double passes of the laser radiation per resonator round trip, so that the gain per round trip is doubled and the threshold pump power is reduced. The thin-disk laser should not be confused with the rotary disk laser, where the gain medium is a quickly rotating disk, which is usually a few millimeters thick.
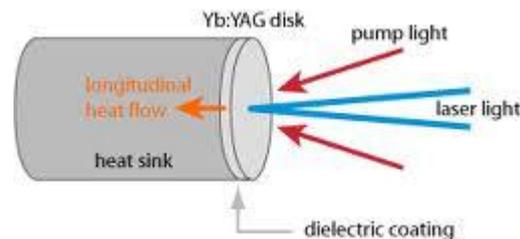
Figure 1.14 - Schematic setup of a thin disk laser head

1.5.1 Thermal lensing effect and power scalability

Due to the small thickness of the disk (100–200 μm for Yb:YAG), the temperature rise associated with the dissipated power is small. (It is not relevant that the density of heat generation is rather high, because the heat is generated very close to the heat sink.) In addition, the temperature gradients are dominantly in a direction perpendicular to the disk surface (Figure 1.15) and thus cause only weak thermal lensing and

depolarization loss. This allows for operation with very high beam quality due to the weak thermal beam distortions, and stable operation can be achieved over a wide range of pump powers.
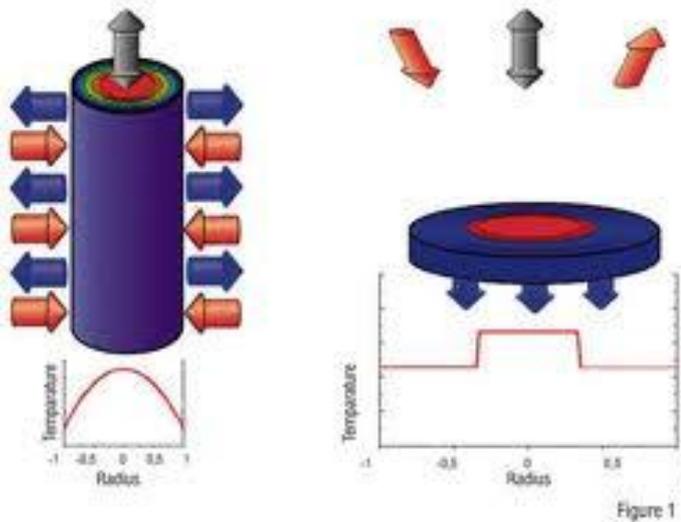
Figure 1.15 – Difference temperature gradients between rod and disk geometry

A very important property arising from the thin-disk geometry is power scalability in a strict and meaningful sense. The scaling procedure is simple: for example, the output power can be doubled by applying twice the pump power to twice the area on the disk, while keeping the disk thickness and doping level constant. The laser resonator has to be modified so as to double the mode area in the disk. With this scaling procedure applied, the new design with twice the output power has unchanged peak optical intensities and a nearly unchanged maximum temperature in the disk (the latter essentially because the cooling area has also been doubled). As far as thermal lensing results from the temperature dependence of the refractive index, the dioptric power (inverse focal length) of the thermal lens is reduced to half of the original value, which just compensates the doubled sensitivity of the larger mode to focal length changes. The power has thus been scaled without increasing optical intensities, the magnitude of temperature rises, or thermal lens problems. Strictly, thermal lensing effects can be increased by the power scaling as

far as they result from mechanical stress in the disk, but this effect can be kept small by keeping the disk thickness small. Another limitation arises from amplified spontaneous emission (ASE) in the transverse direction, which ultimately limits the gain achievable in the longitudinal direction, but becomes severe only at very high power levels with many kilowatts from a single disk. The use of a composite disk with an undoped part on top of the doped part can also strongly suppress ASE; at least for continuous-wave lasers, the ASE limit may be pushed to the order of 1 MW from a single disk.

Power scalability in a wide range is achieved even for passively mode-locked thin-disk lasers. Here, the doubling of the output power also involves doubling of the mode area on the SESAM (semiconductor saturable absorber mirror), so that optical intensities in that device and also cooling issues are not limiting factors. Limitations rather arise from the challenge of implementing dispersion compensation at high power levels.

So far, around 500 W of output power in a diffraction-limited continuous-wave beam have been obtained with a single disk, or around 1 kW using two disks. In multimode operation, more than 4 kW per disk are possible, and 16 kW using four disks in one resonator. Multimode thin-disk lasers with 16 kW output power are commercially available, and similar or even higher power levels in nearly diffraction-limited beam appear to be feasible. With mode-locked thin-disk lasers, ≈ 140 W of average output power has been achieved.

1.5.2 Multipass Pumping

The small thickness of the disk typically leads to inefficient pump absorption when only a single or double pass is used. This problem is normally solved by using a multi-pass pump arrangement, which can be made fairly compact when using a well-designed optical setup, typically containing a parabolic mirror and prism retroreflectors. Such arrangements easily allow one to arrange for 8 or 16 double passes of the pump radiation through the disk without excessively stringent requirements on the pump beam quality. Compared with high-power fiber lasers, thin-disk lasers have lower demands on the brightness of the pump diodes. The pump source of a thin-disk laser is usually based on high-

power diode bars, either in fiber-coupled form or with free-space power delivery. A typical pump wavelength is 940 nm for Yb:YAG, whereas ytterbium-doped tungstate crystals can be more efficiently pumped near 981 nm.

1.5.3 Gain media

The most often used gain medium for thin-disk lasers is Yb:YAG. Compared with Nd:YAG, it has a shorter emission wavelength (typically 1030 nm), a smaller quantum defect (reducing the dissipated power), a longer upper-state lifetime (improving energy storage for Q switching), and a larger gain bandwidth (for shorter pulses with mode locking). On the other hand, it is a quasi-three-level gain medium with significant reabsorption at the laser wavelength, and thus requires higher pump intensities. The thin-disk principle is well adapted to these parameters.

For broad wavelength tuning and for ultrashort pulse generation, other ytterbium-doped gain media offer a still wider gain bandwidth. Examples are tungstate crystals (Yb:KGW, Yb:KYW, Yb:KLuW), $Yb:LaSc_3(BO_3)_4$ (Yb:LSB), $Yb:CaGdAlO_4$ (Yb:CALGO) and $Yb:YVO_4$. Particularly promising are novel sesquioxide materials such as $Yb:Sc_2O_3$, $Yb:Lu_2O_3$ and $Yb:Y_2O_3$, having excellent thermo-mechanical properties and a potential for very high output powers and high efficiencies. A slope efficiency of 80% has been demonstrated with $Yb:Lu_2O_3$.

Nd:YAG or $Nd:YVO_4$ may also be used in thin-disk lasers, when a wavelength of 1064 nm is required, or when the much smaller saturation energy of $Nd:YVO_4$ is relevant.

Generally, a high doping concentration is desirable for thin-disk gain media. This allows one to use a rather thin disk (and thus to minimize thermal effects) without arranging for too many passes of the pump radiation. Most ytterbium-doped gain media are quite favorable in this respect.

CHAPTER 2

Titanium: properties and applications

2.1 Introduction

In 1791 William Gregor the British reverend, mineralogist, and chemist discovered titanium. He examined the magnetic sand from the local river, Helford, in the Menachan Valley in Cornwall, England, and isolated "black sand", now known as "ilmenite". By removing the iron with a magnet and treating the sand with hydrochloric acid he produced the impure oxide of a new element. He named it "mechanite", after the location. Four years later, the Berlin chemist Martin Heinrich Klaproth independently isolated titanium oxide from a Hungarian mineral, now known as "rutile". Greek mythology provided him a new name from the children of Uranos and Gaia, the titans. The titans were utterly hated by their father and so detained in captivity by him in the earth's crust, similar to the hard to extract ore – hence he named it Titanium. It took more than 100 years before Matthew Albert Hunter from Rensselaer Polytechnic Institute in Troy, N.Y., was able to isolate the metal in 1910 by heating titanium tetrachloride ($TiCl_4$) with sodium in a steel bomb. Finally, Wilhelm Justin Kroll from Luxembourg is recognized as father of the titanium industry. In 1932 he produced significant quantities of titanium by combining $TiCl_4$ with calcium. At the beginning of World War II he fled to the United States. At the U.S. Bureau of Mines he demonstrated that titanium could be extracted commercially by reducing $TiCl_4$ by changing the reducing agent from calcium to magnesium. Today this is still the most widely used method and is known as the "Kroll process". After the Second World War, titanium-based alloys were soon considered key materials for aircraft engines. In 1948 the DuPont Company was the first to produce titanium commercially. Today aerospace is still the prime consumer of titanium and its alloys, but other markets such as

Table 2.1 - Physical properties of high-purity polycrystalline titanium (> 99.9%) at 25C

Structure prototype	Mg
Pearson symbol	hP2
Space group	$P6_3/mmc$ (194)
β-transus temperature	882 °C
Lattice parameters	a = 0.295 nm c = 0.468 nm c/a = 1.587
Thermal expansion coefficient [10^{-6} K^{-1}]	8.36
Thermal conductivity [W/m K]	14.99
Specific heat capacity [J/kg K]	523
Electrical resistance [10^{-9} Ω m]	564.9
Elastic modulus [GPa]	115
Shear modulus [GPa]	44
Poisson's ratio	0.33

architecture, chemical processing, medicine, power generation, marine and offshore, sports and leisure, and transportation are gaining increased acceptance. Titanium is not actually a rare substance as it ranks as the ninth most plentiful element and the fourth most abundant structural metal in the Earth's crust exceeded only by aluminum, iron, and magnesium. Unfortunately, it is seldom found in high concentrations and never found in a pure state. Thus, the difficulty in processing the metal makes it expensive. Even today it is produced only in a batch process, and no continuous process exists as for other structural metals. Titanium usually occurs in mineral sands containing ilmenite ($FeTiO_3$), found in the Ilmen mountains of Russia, or rutile (TiO_2), from the beach sands in Australia, India, and Mexico. Titanium dioxide is a very versatile white pigment used in paint, paper, and plastic, and consumes most of world production. Besides Russia, Australia, India, and Mexico, workable mineral deposits include sites in the United States, Canada, South Africa, Sierra Leone, Ukraine, Norway, and Malaysia. Of all the 112 chemical elements in the periodic system known today, about 85% are metals or metalloids. There are various ways to classify the metals, such as ferrous or nonferrous metals, ingot or sintered metals, light or heavy metals. Titanium is classified as a nonferrous and light metal. The properties of

metals are essentially based on the metallic bonding of the atoms in the crystal lattice. This means that the free, mobile valence electrons in the lattice result in classic "metallic" properties such as electrical conductivity, plastic deformation by atomic slip in crystal lattices, and alloying by incorporation of impurity atoms into the crystal lattice with the consequence of increased hardness and strength as well as reduced ductility. Table 2.1 shows a selection of important physical properties of highly pure polycrystalline titanium. Metals vary substantially in weight. At 0.5 g cm–3 Lithium has the lowest density while Osmium and Iridium are the heaviest metals with a density of 22.5 g cm^{-3}. The separation point between light and heavy metals is 5 g cm^{-3}. Therefore, Titanium with a density of 4.51 g cm^{-3} is the heaviest light metal. Although twice as heavy as the classic light metal – aluminum – it has only about half the specific weight of iron or nickel (Figure 2.1). Titanium alloys primarily stand out due to two properties: high specific strength and excellent corrosion resistance. This also explains their preferential use in the aerospace sector, the chemical industry, medical engineering, and the leisure sector. Only at temperatures below 300C do carbon fiber reinforced plastics have a
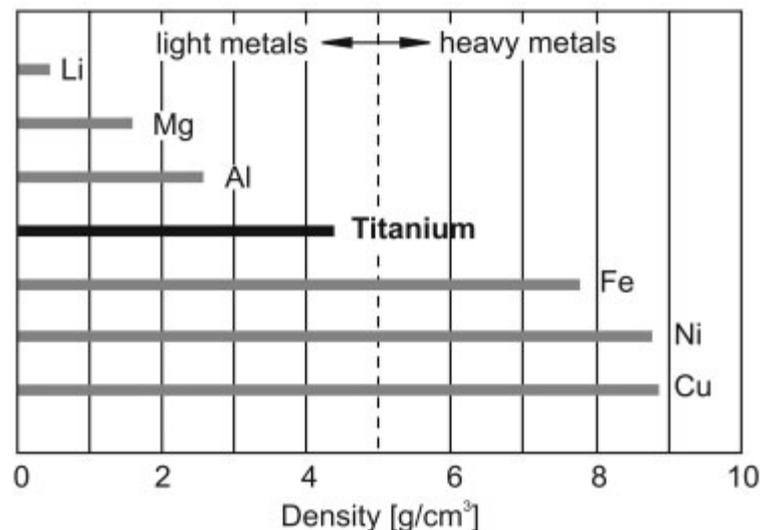
Figure 2.1 - Density of selected metals
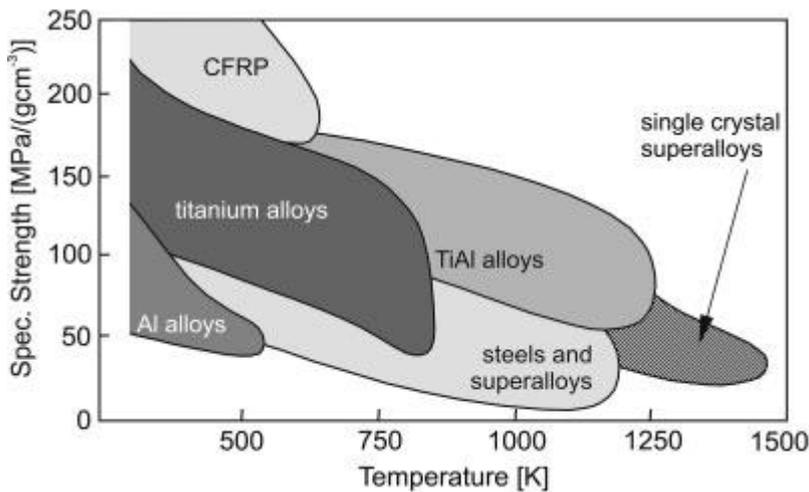
Figure 2.2 - Specific strength versus use temperature of selected structural materials compared with titanium alloys and aluminides

higher specific strength than titanium alloys (Figure 2.2). At higher temperatures the specific strength of titanium alloys is particularly attractive. However, the maximum application temperature is limited by their oxidation behavior. Since titanium aluminides partly overcome this disadvantage, they have become the subject of intense alloy development efforts. While conventional elevated temperature titanium alloys are used only up to temperatures slightly above 500C, TiAl-based alloys directly compete with well-established high temperature steels and Ni-base superalloys (Figure 2.2).

2.2 Metallurgy of titanium

Like a number of other metals – Ca, Fe, Co, Zr, Sn, Ce, and Hf – titanium can crystallize in various crystal structures. However, each modification is only stable within particular temperature ranges. The complete transformation from one into another crystal structure is called allotropic transformation; the respective transformation temperature is called the transus temperature. Pure titanium, as well as the majority of titanium alloys, crystallizes at low temperatures in a modified ideally

hexagonal close packed structure, called α titanium. At high temperatures, however, the body-centered cubic structure is stable and is referred to as β titanium. The β-transus temperature for pure titanium is 882±2 °C. The atomic unit cells of the hexagonal close packed (hcp) α titanium and the body-centered cubic (bcc) β titanium are schematically shown in Figure 2.3 with their most densely packed planes and directions highlighted. The existence of the two different crystal structures and the corresponding allotropic transformation temperature is of central importance since they are the basis for the large variety of properties achieved by titanium alloys. Both plastic deformation and diffusion rate are closely connected with the respective crystal structure. In addition, the hexagonal crystal lattice causes a distinctive anisotropy of mechanical behavior for the titanium. The elastic anisotropy is particularly pronounced. The Young's modulus of titanium single crystals consistently varies between 145 GPa for a load vertical to the basal plane and only 100 GPa parallel to this plane.
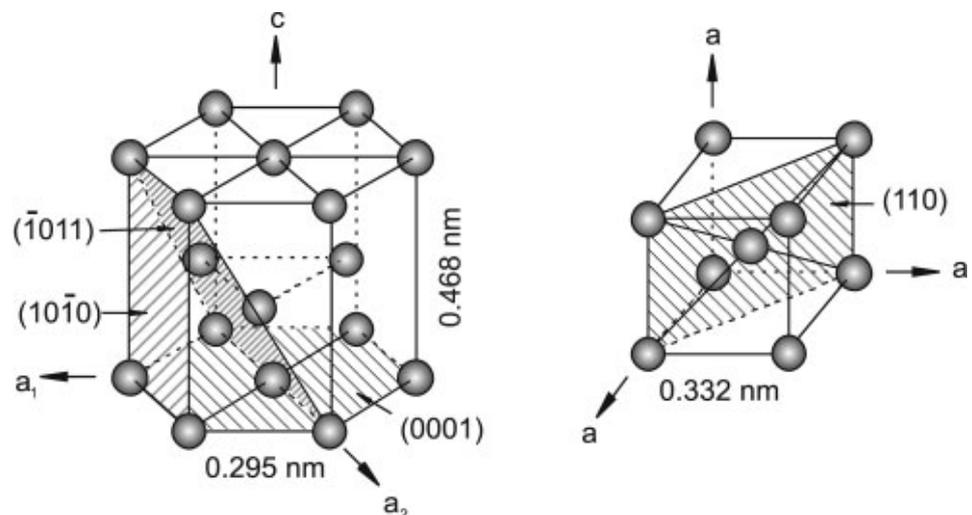
Figure 2.3 - Crystal structure of hcp α and bcc β phase.

2.2.1 β-α Transformation

Upon cooling from the β phase field of titanium the most densely packed planes of the bcc β phase {110} transform to the basal planes {0001} of the hexagonal α phase. The distance between the basal planes in is slightly larger than the corresponding distance between the {110} planes in β. Therefore, the β/α transformation causes a slight atomic distortion (Figure 2.4). This leads to a slight contraction of the c-axis relative to the a-axis in the hcp α and reduces the c/a-ratio below the value of ideally close packed hexagonal atomic structures. A slight increase in volume is observed macroscopically during cooling through the β/α transformation temperature.
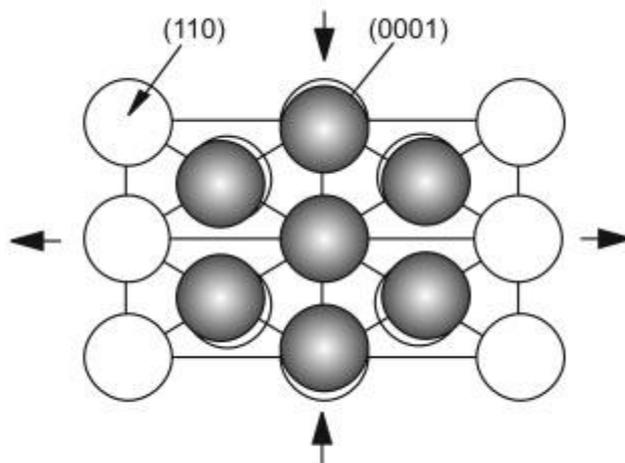
**Figure 2.4 – β/α transformation according
to Burgers relationship**

The corresponding transformation of the slip planes of the bcc β titanium into the basal planes of the hcp α titanium and the respective orientations of the slip directions is given by the following orientation relationship:

$\{0001\}_\alpha // \{110\}_\beta$
$<1120>_\alpha // <111>_\beta$

Since the Burgers vectors can also describe the slip directions, the above orientation relationship is referred to as a Burgers relationship. The six slip planes and the two slip directions of the β titanium unit cell give a maximum of 12 variants of orientation to the α. This variety of orientations is also reflected in the metallographic microstructure. Within the prior β grains, which can be as large as several millimeters, individual α lamellar packets nucleate and grow according to the previously mentioned 12 orientation relationships, with the individual lamellar packets having a common orientation within them. The large – but limited to 12 – number of possible orientations results in multiple repetitions of the orientation of the lamellar packets. Consequently, this results in a very characteristic microstructure similar in appearance to the weave pattern of a basket and are therefore referred to as basket- weave structures (Figure 2.5).
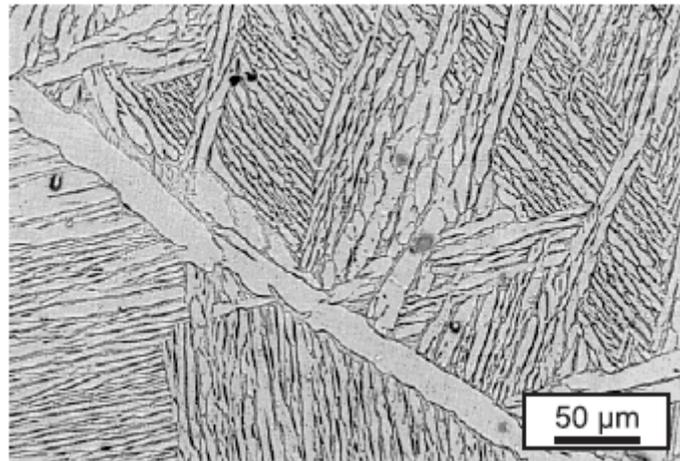
Figure 2.5 – Lamellar microstructure of Ti-6Al-4V

2.2.2 Diffusion

Because of the densely packed atoms in hcp α titanium, diffusion is considerably lower than in bcc β titanium: the diffusion coefficient of α titanium is orders of magnitude smaller than that of β titanium. The

following coefficients are given for self-diffusion of titanium at 500 °C and 1000 °C. The resulting diffusion paths, d, after 50 h at 500 °C and 1 h at 1000 °C illustrate these differences.

500 °C:	$D_{\alpha\text{-Ti}} \approx 10^{-19}$ m^2/s	after 50 h:	d≈0.8 μm
	$D_{\beta\text{-Ti}} \approx 10^{-18}$ m^2/s		d≈0.9 μm
1000 °C	$D_{\alpha\text{-Ti}} \approx 10^{-15}$ m^2/s	after 1 h:	d≈4 μm
	$D_{\beta\text{-Ti}} \approx 10^{-13}$ m^2/s		d≈40 μm

The different diffusion coefficients of α and β titanium are influenced by the microstructure and thus influence the mechanical behavior of the two phases, e.g. creep performance, hot workability, and superplasticity. The limited volume diffusion in α titanium translates into a superior creep performance of α titanium and α containing Ti alloys compared to β titanium. Below the β-transus temperature, time- and temperature-dependent diffusion processes are substantially slower. Therefore, fast cooling leads to a very fine lamellar structure whereas upon slow cooling a coarse lamellar structure is obtained. The radial spread of the α lamellae is parallel to the {110} planes of the β phase. If sufficient cooling rate is provided, the individual lamellae not only nucleate at grain boundaries but also on the growth front of individual lamellar packets. At high cooling rates from temperatures above the martensite start temperature, the bcc β transforms completely into the hcp α by a diffusionless transformation process, leaving behind a metastable fine plate-like, or acicular, martensitic microstructure. The martensitic transformation does not lead to embrittlement; however, strength is slightly increased compared to α titanium. The martensite can be further split into hexagonal α' martensite and orthorhombic α'' martensite, the latter being observed on quenching from temperatures below about 900 °C. The orthorhombic α'' martensite is characterized by good deformability. The hexagonal α' martensite has a similar orientation relationship to β as that of α. The martensitic microstructure is therefore also characterized by a very fine basket-weave structure with needle-like character due to its diffusionless nucleation process.
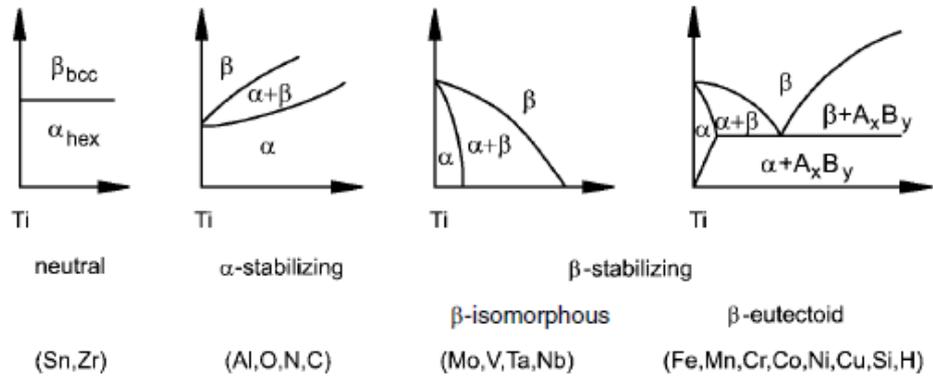
Figure 2.6 – Influence of alloying elements on phase diagrams of Ti alloys

2.3 Titanium alloys

Depending on their influence on the β-transus temperature, the alloying elements of titanium are classified as neutral, α-stabilizers, or β-stabilizers (Figure 2.6). The α-stabilizing elements extend the α phase field to higher temperatures, while β-stabilizing elements shift the β phase field to lower temperatures. Neutral elements have only minor influence on the β-transus temperature. Apart from the regular alloying elements, there are also primarily nonmetallic elements on the order of few 100 ppm present as impurities. Among the α-stabilizers, aluminum is by far the most important alloying element of titanium. The interstitial elements oxygen, nitrogen, and carbon also belong to this category. In addition to extending the α phase field to higher temperatures, the α-stabilizers develop a two-phase α+β field. α-stabilizing elements are subdivided into β-isomorphous and β-eutectic elements. Of these, the β-isomorphous elements, e.g. Mo, V, and Ta, are by far more important due to their much higher solubility in titanium. On the other hand, even very low volume fractions of β-eutectic elements, e.g. Fe, Mn, Cr, Co, Ni, Cu, Si, and H, can lead to the formation of intermetallic compounds. Sn and Zr are considered neutral elements since they have (nearly) no influence on the α/β phase boundary. As far as strength is concerned, they are not neutral since they primarily strengthen the α phase. Usually titanium alloys are classified as α, α+β, and β alloys, with further subdivision into near-α and metastable β alloys. This is schematically outlined in a threedimensional

phase diagram, which is composed of two phase diagrams with an α- and a β-stabilizing element respectively (Figure 2.7). According to this scheme, the α alloys comprise commercially pure (cp) titanium and alloys exclusively alloyed with α-stabilizing and/or neutral elements. If minor fractions of β-stabilizing elements are added, they are referred to as near-α alloys. The α+β alloys, the most widely used alloy group, follow this class; at room temperature these alloys have a β volume fraction ranging from about 5 to 40%. If the proportion of β-stabilizing elements is further increased to a level where β no longer transforms to martensite upon fast
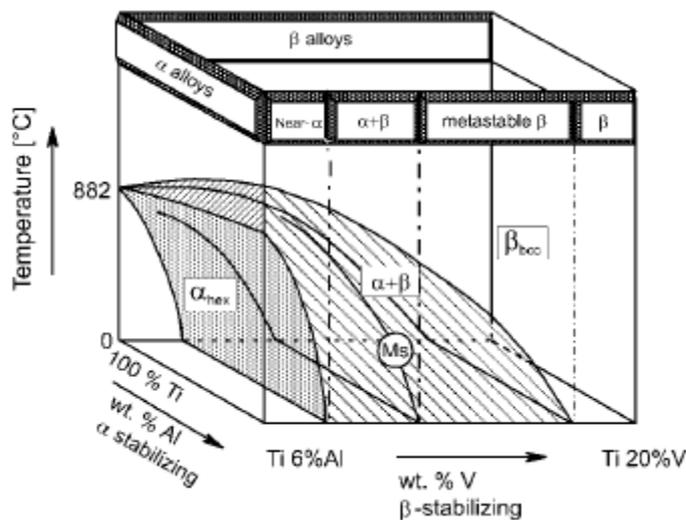
Figure 2.7 – Three-dimensional phase diagram to classify Ti alloys
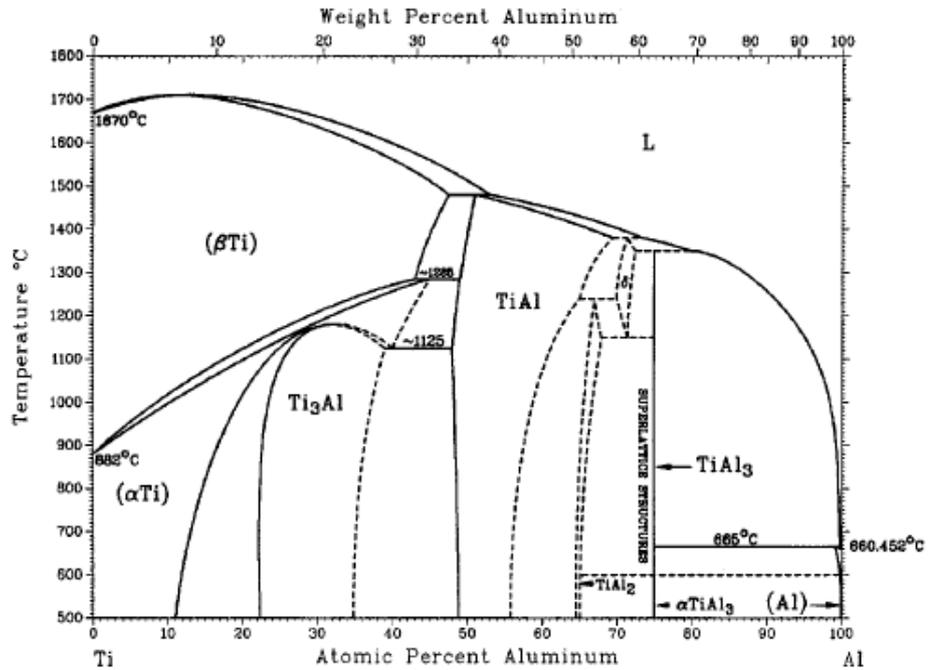
Figure 2.8 – The Ti-Al phase diagram

quenching, the alloys are still in the two-phase field and the class of metastable β alloys is reached. It should be noted that these alloys can still reveal an equilibrium β volume fraction of more than 50%. Finally, the single-phase β alloys mark the end of the alloying scale of the conventional titanium alloys. The most important and by far most intensively investigated titanium phase diagram is the system Ti-Al (Figure 2.8). Apart from the α and β phases, which are of central importance for the conventional titanium alloys, several intermetallic phases are present, such as α_2-Ti_3Al, γ-TiAl, $TiAl_2$ and $TiAl_3$. Of these only the α_2-Ti_3Al and γ-TiAl are of technical relevance today, since $TiAl_2$ and the stoichiometric compound $TiAl_3$ (a line compound) are extremely brittle. Titanium aluminide alloys of technical interest are found in the range of the two-phase field α+α_2 and of γ-TiAl. With the exception of model alloys, the latter alloys are usually also two-phase α_2+γ or multi-phase alloys depending on the alloying elements. If these aluminides are alloyed with Nb another intermetallic phase – Ti_2AlNb – appears, which is the basis for the class of orthorhombic titanium aluminides. A further

intermetallic phase with some technical relevance is the τ phase, which belongs to the cubic $L1_2$ family. This phase is present when elements like V, Cr, Mn, Fe, Co, Ni, Cu, or Zn substitute for about 10% of the aluminum in high Al-containing $TiAl_3$-base alloys.

2.3.1 The alloying elements of titanium

The properties of titanium alloys are essentially determined by two factors: the chemical composition and the microstructure. The chemical composition of the titanium alloys primarily determines the properties and volume fraction of the phases, α and β. Due to the limited deformation capability of hexagonal dense packed crystal structures, α is less ductile compared with the body-centered cubic β. The diffusion coefficient of α is more than two orders of magnitude lower than that of β. Therefore, the resistance to creep and oxidation increases with increasing aluminum content, while simultaneously the ductility and the deformation capability deteriorate. Therefore, care had to be taken when new alloys were developed so as to not exceed 9 wt. % of the so-called aluminum-equivalent

Al eq.=wt. %Al+1/3 wt. %Sn+1/6 wt. %Zr+10 wt. %O <9 wt. %

for otherwise the alloy-embrittling intermetallic compound Ti_3Al precipitated. For this reason the aluminum content of conventional titanium alloys was limited to a maximum of 6 wt. % for a long time. Today, however, this borderline is intentionally crossed, as demonstrated by the large activities on titanium aluminides. Scientists and engineers have learned to take advantage of the extraordinary properties of intermetallic compounds on the basis of Ti_3Al (α_2) and, in particular, of TiAl (γ). Si, Sn, Zr, and interstitial oxygen strengthen α. Si atoms tend to segregate to dislocations and thus effectively prevent dislocation climb, which improves creep behavior. Zr tends to homogenize fine silicide precipitates. Mo, V, and Nb are moderate solid solution strengtheners of β. In metastable β alloys the β phase can be effectively strengthened by fine omega precipitates. Unfortunately, these high strength levels are usually accompanied by falls in ductility. Nb is known to improve the

oxidation behavior of titanium alloys, while small additions of Pd substantially improve their corrosion resistance.

2.3.2 α alloys

α alloys are primarily used in the chemical and process engineering industry. Here excellent corrosion behavior and deformability are of prime concern while high (specific) strength only ranks second. The various commercially pure (cp) titanium grades differ primarily in oxygen content. As an interstitial alloying element, oxygen drastically increases strength with a simultaneous reduction in ductility. To reach the required strength levels of cp titanium grades, only oxygen is intentionally alloyed; while elements like carbon and iron are considered impurities brought into the alloy via the manufacturing process. The four cp titanium Grades 1 to 4 cover a room temperature tensile strength level of 240 to 740 MPa. Of these, Grade 1 has the lowest strength level and excellent cold formability. Therefore, it is used for deep drawing applications, as cladding alloy for steel reactors, as well as sheet metal for explosive claddings – generally speaking for parts which require excellent corrosion resistance but only low strength. Grade 2, with tensile strength levels between 390 and 540 MPa, is the most popular cp titanium grade. Higher strength Grade 3 is nearly exclusively used for pressure vessel applications. This still moderately cold-formable higher strength grade allows for designs with reduced wall thickness and is therefore used where weight is a concern. Grade 4 has the highest strength of up to 740 MPa and is preferentially used for mountings and fittings. However, complex parts have to be shaped at temperatures around 300 °C. For the highest corrosion protection requirements, the Pd-containing alloy Grade 7 was developed. However, due to its high price the nearly equivalent alloy Grade 12 is often preferred. If higher strength levels are required, Ti-5Al-2.5Sn is a good choice. As one of the oldest titanium alloys, it gained acceptance decades ago for low-temperature applications as a material for hydrogen tanks and pressure vessels. Like the other α alloys, Ti-5Al-2.5Sn cannot be age hardened and is thus easy to weld.

2.3.3 α+β alloys

Among the α+β alloys, Ti-6Al-4V is by far the most popular titanium alloy. More than 50% of all alloys in use today are of this composition. The alloy was developed in the early 1950s in the United States at the Illinois Institute of Technology and is therefore one of the very first titanium alloys to be made. There are two reasons for the success of Ti-6Al-4V. First, the good balance of its properties. Second, it is the by far the most intensively developed and tested titanium alloy, which is a major advantage – especially in the aerospace industry, the largest user of Ti-6Al-4V. Other α+β alloys like Ti-6-6-2 and IMI 550 were primarily developed for high strength. High strength and high toughness is realized with Ti-6-2-4-6. Alloys Ti- 6-2-2-2-2, Ti-55-24-S or Ti-17 were primarily developed for elevated temperature applications in gas turbine engines up to about 400 °C.

2.3.4 β alloys

Beta titanium alloys are the most versatile class of titanium alloys. They offer the highest strength to weight ratios and very attractive combinations of strength, toughness, and fatigue resistance at large cross sections. Some of the disadvantages compared to α+β alloys are increased density, a rather small processing window, and higher cost. In the past Ti-13V-11Cr-3Al had been applied to a larger extent (SR-71 Project). Currently five alloys are mainly used: Ti-10-2-3, Beta C, Ti-15-3, TIMETAL 21S, and BT 22 for structural components, and Ti 17 for gas turbine engine compressor discs. Among these alloys, Ti-10-2-3 offers, when properly processed, the best combinations of strength, toughness, and high cycle fatigue strength of any titanium alloy. Recently some new alloys like Beta-CEZ, LCB, and SP 700 have been developed and are now being introduced. More information about the particular use of these alloys will be given later. One of the keys for successful application of beta alloys is the development of appropriate processing conditions. Systematic correlations between processing, microstructure, and properties must be derived in order to find a technically reasonable and safe processing window.

2.4 Mechanical properties of titanium alloys

A convenient and widely used system for specific identification of the various grades of commercially pure titanium and titanium alloys used for engineering and corrosion resisting applications is provided by ASTM which cover all the forms supplied in titanium and its alloys:

B 265 - Strip Sheet and Plate
B 337 - Seamless and Welded Pipe
B 338 - Seamless and Welded Tube
B 348 - Bars and Billets
B 363 - Seamless and Welded Fittings
B 367 - Castings
B 381 - Forgings
B 861 - Seamless Pipe (to replace B337)
B 862 - Welded Pipe
B 863 -Wire
F 67 - Unalloyed Titanium for Surgical Applications
F 136 - Ti-6Al-4V for Surgical Applications

Grades 1,2,3,4 are commercially pure (alpha) titanium, used primarily for corrosion resistance. Strength and hardness increase, and ductility reduces with grade number. Grade 2 is the most widely used specification in all product forms. Grade 1 is specified when superior formability is required. Grades 3 and 4 are used where higher levels of strength are necessary.

Grades 7, 11, 16, 17, also alpha alloys, contain palladium (Pd) and provide superior corrosion resistance in particular to reducing acid chlorides. Grades 26 and 27 are similarly also alpha alloys, and contain .1% ruthenium (Ru) to provide enhanced corrosion resistance in reducing environments. The mechanical properties of grades 7, 16 and 26 are identical to those of Grade 2. The mechanical properties of grades 11, 17 and 27 are similarly identical to those of Grade 1. Grade 12 (alpha) also offers superior corrosion resistance to commercially pure titanium, but is stronger and retains useful levels of strength up to 300 °C.

Grade 5 is the 'workhorse' alpha-beta alloy of the titanium range. It is also specified with reduced oxygen content (ELI) for enhanced toughness (Grade 23), and with addition of .05% palladium for added corrosion resistance, (Grade 24) and with palladium and nickel (Grade 25). Current

interest in this alloy for marine applications is focused upon Grade 23 with .05% palladium or Grade 29 with .1% ruthenium. Restrictions on fabricability may limit availability in certain products.

Grade 9, (near alpha) has good fabricability and medium levels of strength. Grade 18 (Grade 9 + .05% Pd) and Grade 28, (Grade 9 + .1% Ru) offer enhanced corrosion resistance.

Beta-C and TIMETAL®21S are high strength highly corrosion resistant beta alloys in the ASTM range. They are respectively Grade 19, and Grade 21. (The counterpart of Grade 19 with .05% Pd is Grade 20). Grade 32 (Navy alloy) has good weldability together with high toughness and resistance to stress corrosion cracking in marine environments. Grade 21, (TIMETAL®21S) and Grade 32, (TIMETAL®5111) are also available with the addition of .05% palladium.

Weldments in ASTM grade 2 are normally characterised by increased strength, accompanied by a reduction of ductility and fracture toughness. Any strengthening induced by cold work will be lost in the joint region. Weldments in Ti-6Al-4V typically exhibit nearmatching strengths to the base metal, but have lower ductility. The toughness of the weld zone is superior to alpha-beta processed material, showing similar values to alpha-beta processed parent alloys.

Table 2.2 - Typical mechanical properties and physical properties of titanium and titanium alloys

Designation	Commercially Pure Titanium	Medium Strength Alloys	High Strength Alloys	Highest Strength
Alloy type	Alpha	Alpha-Beta	Alpha-Beta	Beta
0.2% Proof Stress MPa	345-480	480-550	725-1000	1100-1400
Tensile Strength MPa	480-620	600-650	830-1100	1200-1500
Elongation %	20-25	15-20	8-15	6-12
Tensile Modulus GPa	103	104	110-120	69-110
Torosion Modulus GPa	45	43	40-48	38-45
Hardness HV	160-220	200-280	300-400	360-420

Density g/cm^3	4.51	4.48-4.51	4.43-4.60	4.81-4.93
Thermal expansion 10^{-6}/°C	8.9	8.3	8.9	7.2-9.5
Conductivity W/mK	22	8.0	6.7	6.3-7.6
Specific Heat J/kg °C	525	544	565	490-524

2.5 Fabrication of titanium alloys

To build a usable component from titanium or titanium alloys with the required properties, the semi-finished products have to be put into a final shape. This requires similar forming methods to those used for metals in general. Since the starting titanium products are already relatively expensive, attempts are made to minimize the machining costs for final component design. Therefore, cost-optimized titanium parts are almost always a result of a carefully selected processing route. In particular, "near-net-shape" processing has the potential to substantially reduce the manufacturing costs and simultaneously increase the material output factor, which is called the "fly-to-buy-ratio" in the aerospace sector. In the following, first machining procedures for titanium alloys will be described. Then, manufacturing methods with a high net-shape potential like casting, welding, superplastic forming in combination with diffusion bonding, as well as powder metallurgy will be highlighted.

2.5.1 Machining

To a large extent, machining of titanium and titanium alloys follows criteria that are also applied to common metallic materials. Compared to high strength steels, however, some restrictions have to be recognized, which are due to the unique physical and chemical properties of titanium:

- The lower thermal conductivity of titanium hinders quick dissipation of the

heat caused by machining. This leads to increased wear of the cutting tools.

- The lower modulus of elasticity of titanium leads to significant spring back after deformation under load. This causes titanium parts to move away from the cutting tool during machining.
- The lower hardness of titanium and its higher chemical reactivity leads to a tendency for galling of titanium with the cutting tool.

Therefore, some general guidelines should be adhered to for successful machining of titanium parts:

- The workpiece should be as short as possible and mounted to be vibration-free into the grips of the working machine.
- Sharp cutting tools should be used and replaced at the first sign of wear. Tool failure occurs quickly after a small initial amount of wear.
- A stiff working machine and stiff grips are required.
- The titanium parts have to be effectively cooled by use of copious amounts of cutting fluid. This allows the heat to dissipate quickly, but also fire can be prevented, since titanium fines, turnings, or chips can cause a fire hazard. Waterbased soluble oils can be used, as well as solutions of vapor-phase rust inhibitors of the nitrite amine type.
- Low cutting speeds should be used while feed rates should be high. Never stop feeding while the cutting tool and work piece are in moving contact, since this could promote smearing or galling, and rapid tool destruction.
- Hard surface scales should be removed before machining, either by grit blasting or pickling in a solution of 2% hydrofluoric acid and 20% nitric acid.

High-speed cobalt-based steel tools are mostly used for machining titanium because of their flexibility and low cost. High feed rates and speeds or rough surfaces may, however, require special qualities found in cemented carbides or stellites. Because of titanium's tendency to smear and gall with the tooling, milling turns out to be more difficult than turning. Generally, cut-down milling is preferred to conventional milling since damage to the milling cutter from built-up edges and chip welding to the cutting edge are minimized. Clearance angles for face milling cutters should be greater than those used for steel. Use of sharp tools is a

must. End milling of titanium is best performed by using short length cutters, which should have sufficient flute space to prevent chip clogging. For drilling, the workpiece should be clamped as rigidly as possible. This usually prohibits manual drilling. The drill, preferably high-speed cobalt-containing steel with short cutting length, should be sharpened and cleaned. The feed rate can be high, the cutting speed, however, must be low. To avoid excessive friction, cooling with chlorinated cutting oil is required. The drill should be put on strongly, and drilling chips should be removed by raising the drill frequently. To allow a free flow of chips, the rake angle of the drill must be sufficiently large to avoid welding between the drill and the workpiece. The tendency of titanium for fretting and galling is a particular concern during thread cutting. For this reason, the use of chemically active lubricants is recommend, e.g. sulfurous cutting oils or mixtures including carbon tetrachloride, molybdenum sulfide or graphite. Straight, clean holes must be drilled to ensure good tapping results. To avoid unnecessarily shortening tool life, threads shouldn't be cut manually where possible. Male threads have to be cut on a lathe since cutting dies can fret, thus preventing sound threads. The thread depth should be increased gradually. For cutting female threads a drill with a strong core and a short cutting edge should be used. The tap drill should be extra tapered and flank relieved. Titanium can be sawn using conventional band sawing or power hacksawing. Because of titanium's poor heat dissipation, the saw speed should be reduced by about one quarter compared to steel. Appropriate cooling also has to be provided here, preferably on the basis of sulfurous or chlorinated oils. The contact pressure of the saw blade should be high. Carbide-tipped tooling increases sawing speed. Since hard oxide surface scales increase tool wear, they should be removed before sawing by grit blasting, grinding or chemical agents. The low thermal conductivity of titanium is most noticeable during surface grinding operations. Here it can even come to chemical reactions between the grinding media and the titanium surface, leading to smearing or even to intense sparking, which can cause a fire hazard. Therefore, the use of reduced wheel speeds – half to one third of conventional operating speeds – and ample coolant is therefore essential to get the best results with titanium. As abrasive grinding media, aluminum oxide and silicon carbide wheels as well as resin-bonded diamond wheels have proved to be successful. For smooth surfaces with

minimum roughness, oil emulsions including nitrite-amine-based fluids should be used.

2.5.2 Casting

Casting can be considered to be the classic (near-)net-shape process. Due to often very extensive metal removal by machining from the ingot to the final component, and the relative expense of titanium material, casting offers a high cost saving potential. Furthermore, casting enables to do without extensive post-processing of cast components. Often complex components can be produced for which conventional production methods would be too complex or expensive. Compared to forged parts, however, strength and ductility penalties have to be accepted. These can at least be partly compensated for by intelligent casting-specific component design. The two casting methods used are rammed graphite mold casting and investment casting. Rammed graphite mold casting is similar to sand casting. It is considered an inexpensive process and particularly suitable for large castings. Wooden, plastic epoxy, or metal patterns are used to shape the molds. Coring offers the possibility to produce hollow castings. The mold for the external shape is made in two halves, and the separately made core is then located by core prints between them. The location of the gates and risers have to suit each casting design. The completed molds are then embedded on a casting table for centrifugal casting. Cast components of up to 2750 kg have already been successfully produced. Even larger structures are likely, but can also be manufactured by welding together two or more individual castings. Also, permanent molds of machined graphite blocks may be used. Here sprays have to be used to prevent metal-mold reaction during pouring and to keep the solidified part from sticking to the mold. Permanent molds are preferably used for simple, symmetrical thin section shapes with large flat areas, e.g. plates or missile wings. Investment casting is used in preference to graphite mold casting when close tolerances, thinner sections, smaller draft angles, and better surface finishes are required. Due to the high reactivity of the liquid titanium, casting must be carried out in vacuum and water-cooled crucibles have to be used. The lost-wax process is preferred since it yields high surface quality and precise dimensional components. Often theses

parts require no extra post-processing and are ready to install. First, a wax model is manufactured from a dimensionally stable metal form, e.g. of aluminum. This form takes into account that the wax model must be bigger than the final titanium cast part due to shrinkage of both the wax and the titanium alloy. The wax models are then assembled in a cluster, coated with ceramic slurry, and dried. In the next production step, the ceramic green bodies are dewaxed in an autoclave. Burning provides the required stability to the ceramic form for the actual casting process and, simultaneously, removes left wax residues. Casting then is carried out in a vacuum arc furnace with a self-consuming electrode. The titanium alloy melt drips into a water-cooled copper crucible, forms a thin titanium scull, which then acts as the crucible. Centrifugal casting is used to fill the final mold. After cooling, the casting is removed from the mold by breaking off the ceramic mold (lost wax). After removing stays, risers, and channels the final cast piece is ready. Due to the reaction of the titanium with the ceramic mold, a thin reaction zone is formed during casting, which has an adverse effect on the mechanical properties and must therefore be removed by pickling. To eliminate inevitable porosity, it is a common practice for cast aerospace parts to be hot isostatically pressed (HIP) just below the beta transus temperature at pressures of around 100 MPa. The main fields of application for investment castings are high performance parts for the aerospace and non-aerospace industry. Titanium cast parts are used as static components in jet engines, e.g. as casings, compressor casings or as exhaust gas pipes of auxiliary gas turbines. Furthermore, cast parts from titanium are used in the automotive industry (valves, turbocharger rotors), medical engineering (implants), dental technology as well as the electronics industry. The 1990s experienced a boom in the manufacture of investment-cast titanium golf club heads.

2.6   Applications

Titanium and its alloys were specially developed for aerospace applications in the 1940s in the United States. Today the aerospace market accounts for about 50% of worldwide titanium consumption, and in the United States these figures have been as high as 70%. However the aerospace market, and in particular the military sector, is characterized by

vigorous boom-to-bust demand and price cycles. Therefore, efforts have been made to substantially increase titanium consumption in less cyclic non-aerospace markets. Here the greatest obstacle has often proven to be the high cost of titanium components, which results from not only the price of the raw material, but also the higher secondary costs of semi-finished and final products. Nowadays the exceptional properties, such as low weight at high strength and outstanding corrosion resistance, have paved the way for titanium and its alloys to enter applications in high-quality industrial and consumer products. Certainly, these are not yet mass-market products, but the trend to use titanium and its alloys outside the aerospace sector continues steadily. In particular, applications in the chemical industry, medical engineering, energy and transportation technology, as well as architecture, sports and leisure have played pioneering roles.

2.6.1 Aerospace

An increasing scarcity of resources and their growing expense demands a reduction in energy consumption for passenger and goods transportation. Here the aerospace sector plays a special role with respect to the application of new materials. Compared to land-based transportation systems, the much lower system quantities and much higher specific energy consumption allow designers to tolerate orders of magnitude higher cost for weight savings. For example, while one kilogram of weight saved in the automotive industry cannot cost more than about € 10, the aerospace industry is willing to pay up to about € 1000. For space applications, more than € 10 000 may oftentimes still be economically attractive. This comparison is even more dramatic if weight savings are compared on a percentage basis. Due to a much higher payoff over a system's life cycle, the tolerable material prices in the aerospace sector are about three to five orders of magnitude higher than those in the automotive industry (Table 2.3). The much higher payoff for weight reduction in aircraft, and especially spacecraft, is rationalized by the much lower payload capacity compared to land-based vehicles. As an example, a Boeing 747 carries about 100 tons of fuel, which is approximately one third the take-off weight of the jumbo jet. This would correspond to a

tank volume of about 500 liters for a mid-sized passenger car. Accordingly, the remaining payload is quite limited. If fuel consumption is lowered by only 10%, a simple estimate shows one could increase the payload of the Boeing 747 by 10 tons. Alternatively, as less fuel means less weight, the use of smaller, lighter engines would be possible. Landing gears, wings, support structure, etc., could similarly be downsized as well. This "snowball effect" leads to secondary weight savings, which are almost as high as that due to the installation of the lighter component itself. What possibilities do materials offer for weight savings in the aerospace arena? A Lockheed study provides some insight to this question. Although based on military aircraft, it still delivers good, general guidelines. The study reasons that if metal density is reduced by 10%, the weight of the component is also reduced by 10%. The same component weight reduction can also be achieved by increasing the strength, but by 35%. Likewise, the stiffness would have to be increased by 50%, and the damage tolerance by 100% to achieve the same 10% weight savings. This underlines the sustained importance of light metals as materials of choice in the aerospace sector.

Table 2.3 - Tolerable extra costs for weight reductions of 1 kg or 1% of the structural weight

	T€/kg	T€/wt.%
Automobile	0.01	0.1
Regional aircraft	0.5	100
Large aircraft	1	1000
Space	10	10000

2.6.2 Aircraft

Compared to steels or aluminum alloys, titanium alloys must be considered a much younger structural material. The first alloys were developed at the end of the 1940s in the USA. Among these was the classic titanium alloy, Ti-6Al-4V, which still captures a large portion of aerospace applications today. The outstanding properties of titanium alloys include high specific strength and excellent corrosion resistance.

Therefore, titanium alloys are found in aerospace applications where the combination of weight, strength, corrosion resistance, and/or high temperature stability of aluminum alloys, high strength steels, or nickelbased superalloys are insufficient. The main drivers for titanium's use in aerospace applications are:

- weight reduction (substitute for steels and Ni-based superalloys)
- application temperature (substitute for Al alloys, Ni-based superalloys, and steels)
- corrosion resistance (substitute for Al alloys and low-alloyed steels)
- galvanic compatibility with polymer matrix composites (substitute for Al alloys)
- space limitation (substitute for Al alloys and steels).

Figure 2.9 shows the percentage of structural weight for various material classes in modern large commercial aircraft, distinguished between airframe and engine materials. The fuselage of the Airbus A330/340, for example, is manufactured of nearly two thirds aluminum. At about 7%, titanium alloys have a similar share of the structural weight as steels. However, at over a third the structural weight, titanium is the second most common material in the jet engine following Ni-based superalloys; and by volume, titanium alloys are the most abundant material in the engine. In addition to material properties, cost is a determining factor in the selection of materials for design. This extends beyond raw material costs to the production costs for the finished component. Therefore, besides the mechanical properties required for component integrity, a material's producibility measured by its castability, machinability, (plastic) formability, and weldability represents an important factor impacting cost. Particularly imperative in the aerospace industry is to adopt a life cycle approach to material selection by considering the cost implications of maintenance and repair over the expected lifetime of a component. The aircraft manufacturers, as well as producers and manufacturers of titanium alloys, are subject to the airlines' demands to maximize component performance while simultaneously reducing overall costs. Applications of titanium alloys in the aerospace sector will be highlighted in the following sections. First, fixed-wing aircraft will be addressed, then the use of titanium in jet engines will be

highlighted, and finally examples for helicopter and space applications will be given.
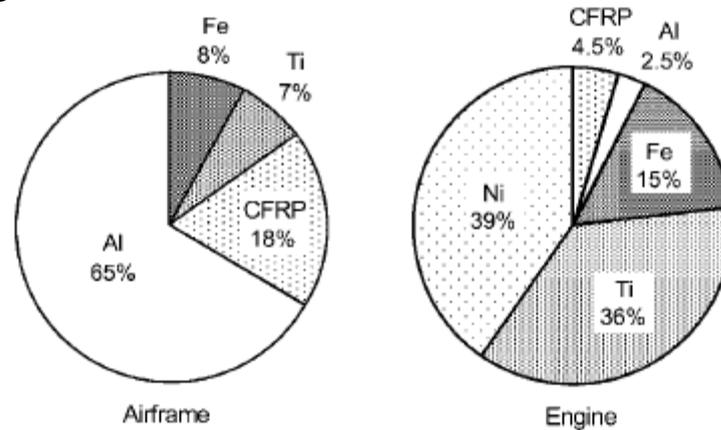
Figure 2.9 – Percentage of aluminum, titanium, and steel alloys and FRP of the structural weight of modern large commercial aircraft and gas turbine engines

Airframe

Oftentimes, saving weight is the major reason for choosing titanium alloys in fuselage applications, thus making use of the high specific strength of the metal. Frequently, the substitution for high-strength steels is worthwhile even if steel's strength is higher, or for aluminum-based alloys even if aluminum's density is lower. This has led to increased use of titanium alloys in fuselages over the past four decades. Figure 2.10 charts the steady growth of titanium use in Boeing commercial aircraft since titanium's introduction to fuselages in the 1950s. Today, it accounts for approximately 9% of the structural weight of the Boeing 777. Similar numbers are found for Airbus aircraft. In the following, typical fuselage applications for titanium alloys are highlighted. Titanium alloys are used to stop fatigue crack growth in aircraft fuselages. They are applied as thin, narrow rings placed around the aluminum aircraft fuselage
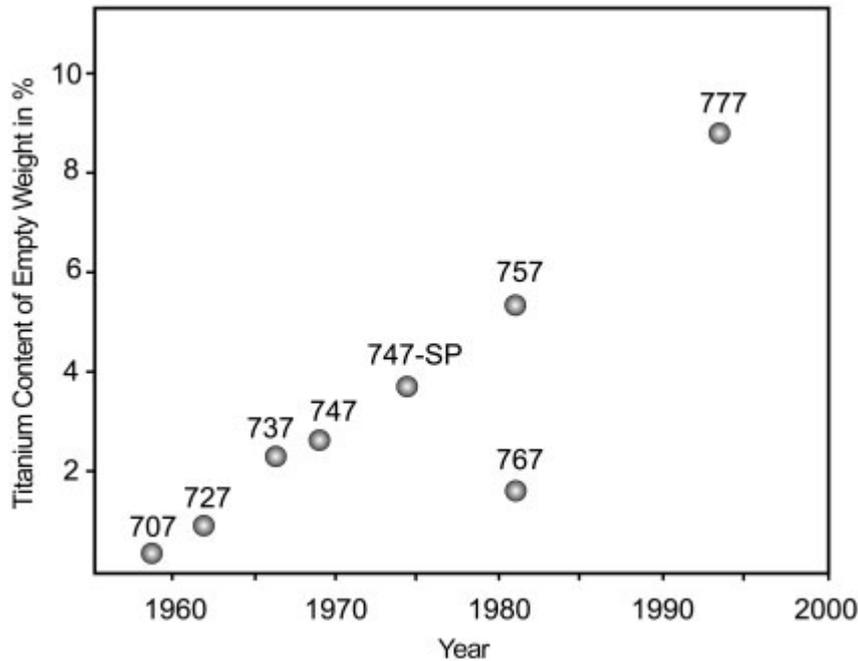
Figure 2.10 – Increase in application of titanium alloys in commercial Boeing aircraft

like a "belly band", preventing potential fatigue cracks from propagating catastrophically in the outer skin. Nowadays, titanium alloys are also used for hydraulic tubing of modern aircraft.

Compared to steel tubes, weight savings of up to 40% are possible. The α+β alloy Ti-3Al-2.5V is primarily used for this application as it is easily deformed and demonstrates sufficient strength. Where high corrosion resistance is required at moderate strengths, commercially pure titanium is used. Aircraft floors surrounding on-board kitchens and toilets are an example where the corrosive environment dictates titanium's use. The piping system for de-icing equipment is manufactured from unalloyed titanium. Here strength is less important than thermal stability. Since temperatures can well exceed 200 °C, aluminum alloys may no longer be used. Furthermore, excellent corrosion resistance is required since warm aggressive media have to be transported. Despite higher initial cost, primary components of aircraft landing gear are increasingly manufactured from forged titanium alloys. The higher up front cost pays

off over the long term as high-strength steels typically need to be replaced at least once in an aircraft's lifetime due to their susceptibility to stress corrosion. Landing gear component replacement is avoided if made from titanium alloys; and the Boeing 777 (Figure 2.11) has set the trend for their use. Here the main landing gear is almost completely manufactured from forged components of TIMETAL 10-2-3, which nearly doubled the amount of titanium used on the 777. The weight savings amounted to approximately 270 kg per aircraft.
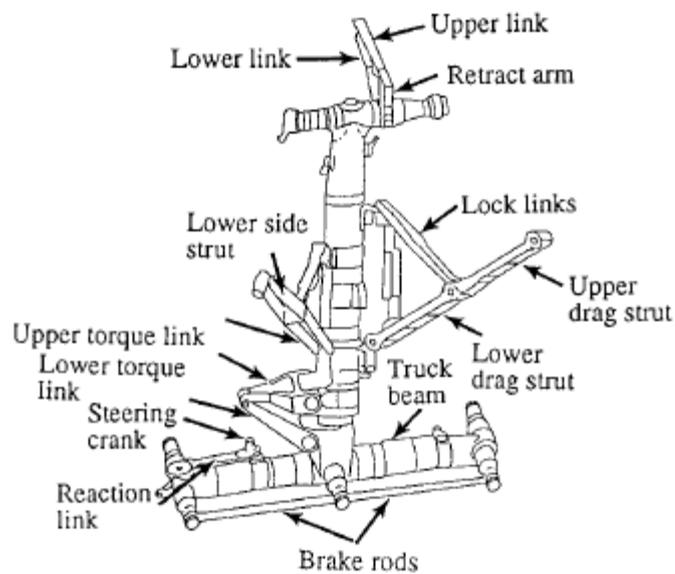
Figure 2.11 – Main landing gear of the Boeing 777 of forged TIMETAL 10-2-3 parts

Due to potentially high loads, e.g. from bird strikes, the frames of cockpit windows are manufactured from forged titanium alloys (Figure 2.12), while aluminum-based alloys provide sufficient strength for other window frames. Titanium alloys are preferred to support the vertical and horizontal stabilizer structure in a carbon fiber reinforced polymer (CFRP) tail assembly. This use is primarily dictated by

**Figure 2.12 – Window frames of Ti-6Al-4V
for the cockpit of a commercial aircraft**

the close match between titanium's coefficient of thermal expansion, compared to aluminum's, and that of polymer matrix composites. Additionally, titanium alloys are chemically more compatible with carbon fibers than aluminum and are used to avoid galvanic corrosion problems. Compared with the commercial aircraft market, the use of titanium alloys is considerably higher in military fighter aircraft. The greater use is driven by design in response to the larger thermal and mechanical loads associated with greater maneuverability and supersonic cruise speed. The proportion of titanium alloys in military aircraft fuselages can exceed 50%; for the SR-71 "Blackbird" it was 95%. Due to the aero kinetic heating of the surface skin, titanium alloys were used since the temperature capability of the most advanced elevated temperature aluminum alloys was insufficient. Today, titanium accounts for about 35 to 50% of the weight of a modern fighter aircraft. The most common area to find titanium is in the engine bay of fighter aircraft, where temperatures can quickly exceed aluminum's capability. For example, conventional titanium sheet and rivet construction was used extensively in the aft end of the US F-15 aircraft. However, with the redesign to the F-15E model, advanced techniques using superplastic forming and diffusion bonding (SPF-DB) were extensively employed for the same structure. This change in manufacturing technique eliminated 726 part details and 10000 fasteners, enhancing the maintainability of the aircraft. Newer alloys such

as Ti-6Al-2Zr-2Sn-2Mo-2Cr-0.25Si are used in the airframes of the US F-22 and Joint Strike Fighter projects. This alloy has moderate temperature capability and is used primarily in engine bay bulkheads of these aircraft where fuselage temperatures are highest. Generally speaking, meeting the high performance requirements of military aircraft is of greater importance compared to commercial aircraft, where overall cost effectiveness is the primary driver. The biggest, and probably also most spectacular, titanium structure in military aircraft is the wing box, which carries the load from the wings and can sometimes incorporate a swing-wing design. Figure 2.13 shows an example of a mid-fuselage bulkhead for the US F-22, which makes up part of the wing box. With a width of 4.90 m, a depth of 1.80 m, and a height of 0.2 m, it is one of the largest titanium forgings ever produced. Although the final component only weighs about 150 kg, it was initially forged from a single cast ingot of almost 3000 kg. This example clearly exhibits the extremely high machining losses, 95%, which can be found in Ti forgings, and demonstrates the opportunity for optimization of the forging process in the future. Titanium alloys are exceptionally well suited as a spring material. Here, in comparison with high strength steels, the density-corrected modulus of elasticity can lead to weight savings of up to 70%, a simultaneous volume savings of up to 50%, and improved corrosion resistance. Due to their higher strengths, alloys such as Beta C or Ti-15V-3Cr-3Sn-3Al are preferred alloy candidates.
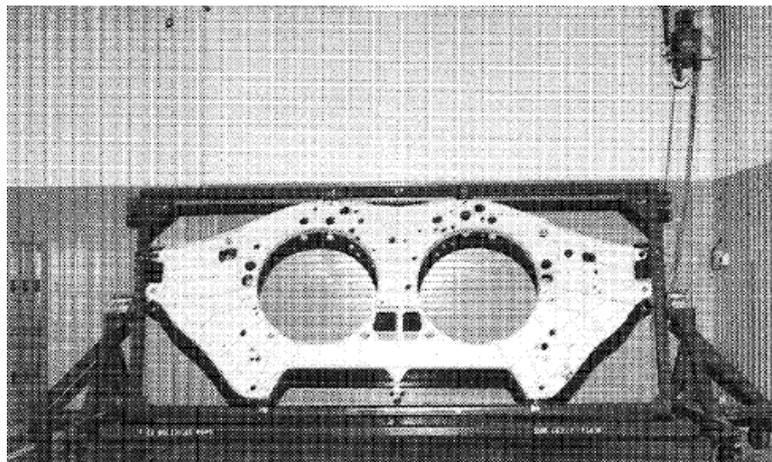
Figure 2.13 – Center bulkhead of the F-22

Gas turbine engines

The main area of application for aerospace titanium alloys is in the gas turbine engine. Approximately one third the structural weight of modern turbine engines is made up of titanium. Besides nickel-based superalloys, titanium alloys are the standard engine material. Indeed, the first jet engines introduced at the beginning of the 1950s by Pratt & Whitney in the USA and Rolls-Royce in England contained titanium alloys. Since then the titanium content has steadily increased, as illustrated for Rolls-Royce engines in Figure 2.14 . Furthermore, over the years an evolutionary trend in alloy design is observed from the α+β alloys to the elevated temperature near-α alloys. Compressor blades were the first engine components to be made from titanium, titanium compressor disks being introduced next. The large front fan blades of modern jet engines are now often made from titanium alloys too. Figure 2.15 shows the scale of such components represented by the Rolls-Royce Trent jet engine series. Due to steadily increasing engine by-pass ratios, the newest blade designs exceed lengths of one meter. At these dimensions, fan blade flutter can become a serious problem since the blade tips may reach the velocity of sound and cause mixed supersonic/subsonic flow fields and generate associated shock waves. To increase their stiffness, shrouds, or snubbers, were added to the middle of the blades. Although these mid-span shrouds were able to control vibration, they adversely affected the aerodynamic efficiency of the fan and lowered fuel efficiency. Advanced fan designs have eliminated shrouds by improving blade stiffness through an increase in chord width and have led to a reduction in the number of blades by about one third. Today, these wide chord fan blades are employed in the latest generation jet engines. However, the large mass of these blades dictates designs other than the previously used solid titanium alloy forgings.
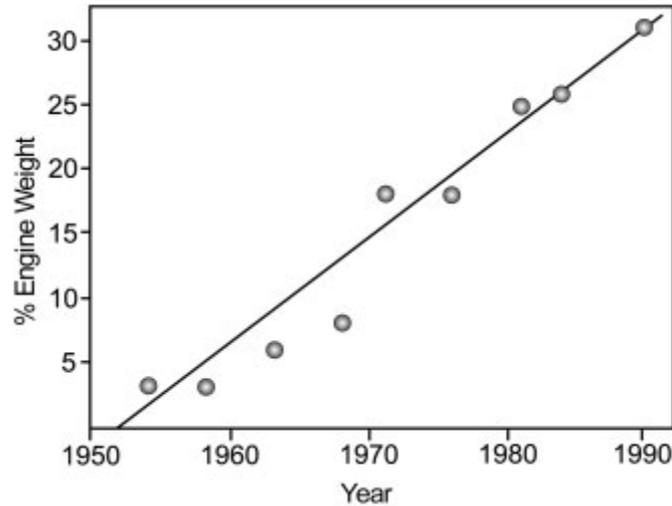
Figure 2.14 – Applications of titanium alloys in Rolls-Royce engines

Figure 2.15 – Front fans of commercial Rolls- Royce Trent engines made of Ti-6Al-4V

The major engine manufacturers have pursued different concepts for the production of lightweight wide chord fan blades for their latest large jet engines. General Electric was the first to use fiber reinforced polymer composites in the fan blades of their GE90. However, to meet erosion

resistance requirements, the blades are designed with leading edges made from titanium. Rolls-Royce and Pratt & Whitney have continued to use designs based on titanium. To reduce the weight of their engines both have moved to hollow titanium fan blade technology. Early hollow fan blade designs were comprised of machined titanium face sheets that were liquid-phase diffusion bonded to a titanium honeycomb core. Advances in manufacturing techniques now allow the blades to be produced from Ti sheet via superplastic forming and solid-state diffusion bonding (SPF-DB). The new engines for the Airbus A380 from both Rolls-Royce (Trent 900) and the GE/Pratt & Whitney Engine Alliance (GP7200) will have fan diameters of approximately three meters and will incorporate hollow titanium fan blades.

Evolutionary engine design stresses the need to further decrease the weight of the compressor blades and disks, while extending component life or inspection intervals. This can be achieved using an integrally bladed disk, or "blisk", design. The finished blisk is a single assembly where disk and blades are metallurgically bonded together. For small blade heights up to about 60 to 80 mm, it is more cost effective to machine a blisk from an oversized forged disk. Larger blades are generally attached to the disk by linear friction welding. In addition to the weight reduction from a blisk design, the lack of a mechanical interface between the blades and the disks eliminates a common site for fatigue crack initiation. This can result in extended inspection intervals. An example of a blisk compressor stage manufactured by MTU Aero Engines is shown in Figure 2.16 . Blisk technology is now standard technology in small and medium size category compressors of commercial and military engines. In the Eurofighter's EJ200 engine, for example, all three stages of the fan section are a blisk design; the first two being manufactured using linear friction welding, the third by electrochemical machining (ECM). Since fan blades and disks are used at low temperatures, they are normally manufactured from Ti-6Al-4V. The maximum temperature limit for this alloy is about 315 °C. Therefore, the disks and blades of the first 4 to 5 stages of the compressor (low-pressure compressor) can also be made from Ti-6Al-4V. However, elevated temperature near-α alloys are used in the high-pressure compressor. Today, the maximum temperature limit for these alloys is about 540 °C. This upper bound is not limited by the elevated temperature strength or creep resistance of the near-α alloys, but by their moderate oxidation resistance, especially in comparison to

nickel-based superalloys. In long-term elevated temperature applications titanium alloys form an "α-case" at the surface, i.e. a zone with a brittle α phase caused by oxygen enrichment, which leads to a drastic reduction in ductility and fatigue strength. For rotating components, titanium's temperature limit can be even lower due to its propensity to burn. This condition is created when a rotating blade rubs on the inside wall of the engine casing causing localized heating at the blade tip. At elevated temperatures and in a high-pressure air environment, this can lead to very rapid oxidation of the titanium. These conditions are encountered in the highpressure compressor of the engine. The oxidation process, which is exothermic, can become self-propagating and cause a titanium fire. To mitigate this problem, Pratt & Whitney developed a highly stabilized β-alloy called Alloy C (Ti-35V-15Cr)
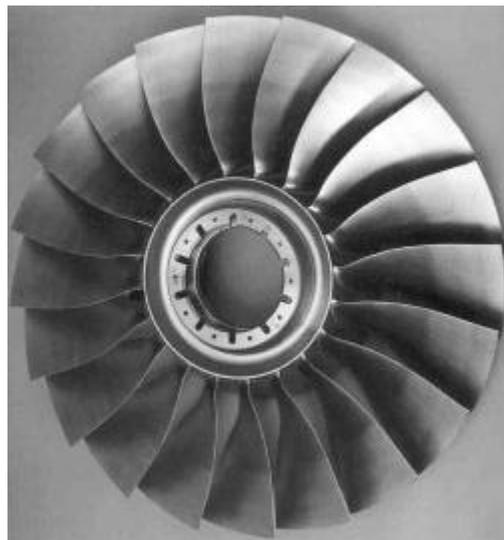
Figure 2.16 – Titanium blisks for compressor applications

that is resistant to burning. This alloy is finding application in the F-22's F119 engine in compressor stators as well as augmentor and nozzle components. These temperature limitations for titanium alloys mean the hottest parts in the compressor, i.e. the disks and blades of the last compressor stages, have to be manufactured from Ni-based superalloys at nearly twice the weight. Additionally, problems arise associated with the different thermal expansion behavior and the bonding techniques of the

two alloy systems. Therefore, enormous efforts are underway to develop a compressor made completely of titanium. Titanium alloys are required that can be used at temperatures of 600 °C or higher. This has been the impetus for extensive research and development work in the area of elevated temperature titanium alloys. The maximum application temperature of titanium alloys has been raised from about 300 °C to nearly 600 °C over the last 40 years.

Within the last few years, the near-α class of elevated temperature titanium alloys has been the subject of particular development interest. An example of the state-of-the-art of this development is IMI 834 (Ti-5.8Al-4Sn-3.5Zr-0.7Nb-0.5Mo-0.35Si), developed jointly in the United Kingdom by IMI Titanium Ltd. and Rolls- Royce in the 1980s. With a potential use temperature of almost 600 °C, the alloy was aimed at replacing the IMI 685 and IMI 829 alloys preferred in European jet engines. After IMI was acquired by Titanium Metals Corporation (TIMET), this alloy was given the trade name TIMETAL 834 and has since found its way into European military jet engines. Presently it is also used as a compressor disk material in the last two stages of the medium-pressure compressor, and the first four stages of the high-pressure compressor in variants of the Rolls-Royce Trent series commercial jet engine. A bimodal microstructure with a primary volume fraction of 15% has proven to be an optimum microstructure for this particular application. In the United States, the mature Ti-6-2-4-2S is still the preferred high temperature alloy for jet engine applications.

Despite the discussion of near-α titanium alloys, the objective to further increase high temperature strength is addressed with the development of titanium aluminides. These materials, based on the intermetallic compounds $\alpha_2(Ti_3Al)$ and $\gamma(TiAl)$, have been studied for their potential to raise the application temperatures of titanium alloys to 650 °C and 800 °C, respectively. Their excellent creep resistance is due to the ordered nature of the crystal structure. However, this structure also makes the intermetallics relatively brittle and correspondingly hard to deform. Alloying with Nb, Cr, V, Mn or Mo and microstructural optimization are two approaches to gain increased ductility. Another important aspect for the use of titanium aluminides in turbine engines is the resistance of these materials to initiating a titanium fire, as shown in Figure 2.17. TiAl-based alloys in particular minimize the risk of titanium fire. Compressor blades of future high-pressure compressors are therefore

a potential application of TiAl alloys. Sufficient damage tolerance, a satisfactory oxidation behavior, and producibility (cost) are critical parameters that will ultimately determine the use of titanium aluminides in aerospace. The prospect for potential application of TiAl-based alloys is much higher for jet engine components with less stringent damage tolerance requirements.
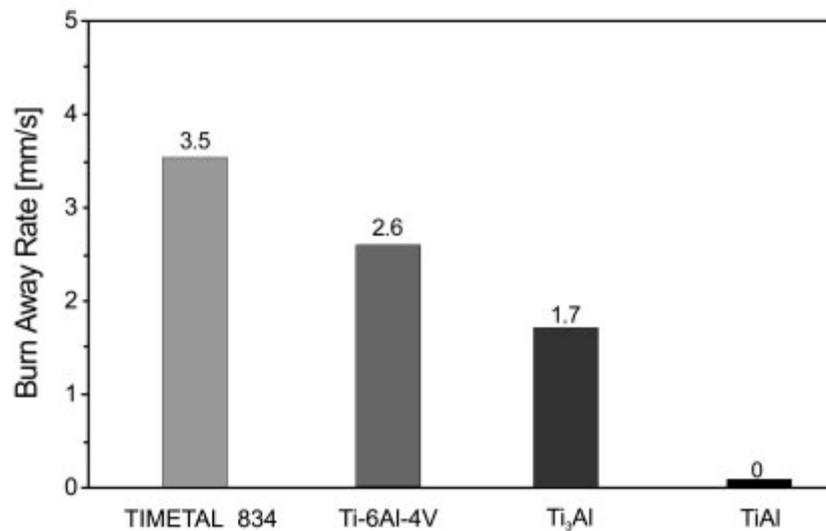
Figure 2.17 – Burn resistance of titanium aluminides compared to conventional titanium alloys

Increased stiffness and elevated temperature strength are the primary goals for the development of long fiber reinforced titanium matrix composites (TMCs). Potential areas for application in jet engines are high-stiffness, high-strength fan blades, and thermally stable cylindrical components in the high-pressure compressor. Most investigations have been carried out on SiC long fiber reinforced Ti-6Al-4V. Matrices of near-α alloys and titanium aluminides, stable at higher temperatures, are also of interest. The availability of TMCs enables previously untenable design approaches, such as the integrally bladed compressor ring, or bling. The bling design eliminates the hub of the disk, significantly reducing the component weight by up to 70%. However, in order to accomplish this, the strength of the material at the base of the blades must

be much higher to support the centrifugal loads and calls for use of metal matrix composite reinforcement. As with blisks, the number of parts is drastically reduced, substantially reducing maintenance costs compared to conventionally bladed rotors. Such improvements are likely to justify the high manufacturing costs, and will allow compressors and jet engines themselves to be built considerably more compact. Continued research and development, particularly in processing and component life management techniques, still have to be completed before these composite materials are put into rotating components. The first aerospace use of continuously reinforced titanium composite material is a low risk application as an actuator piston on the F-22's F119 engine.

Aerospace hydraulic fluid is one of the few corrosive media to otherwise usually corrosion-resistant titanium alloys. Above 130 °C hydraulic fluid forms an acid that etches the titanium and leads to hydrogen embrittlement of the component. One of the few alloys that appears to be immune to this attack is the alloy TIMETAL 21S. For this reason, the Boeing Company uses TIMETAL 21S for the plug and other parts of the nozzle assembly on its 777 aircraft. The 777 uses the largest jet engines GE90, PW4084 and Trent 875. Pratt & Whitney also plans to use similar components manufactured from TIMETAL 21S for its PW4168 engine that flies on the Airbus A330.

Helicopters

For helicopters, titanium alloys are used in the most highly stressed component: the rotor head. Figure 2.18 shows examples of forged Ti-6Al-4V rotor heads for the Eurocopter BO 105 and BK 117 helicopters. However, intensive studies are ongoing for the high-strength β alloy replacements. For example, the alloy TIMETAL 10-2-3 has replaced Ti-6Al-4V for the main rotor head of the Westland Super Lynx helicopter. Today alloys are also established in other helicopter programs. TIMETAL 10-2-3 is used for the rotor mast and rotor head for the US RAH-66 Comanche helicopter. The same alloy is also being applied in the yoke assembly of the tiltrotor V-22 Osprey.
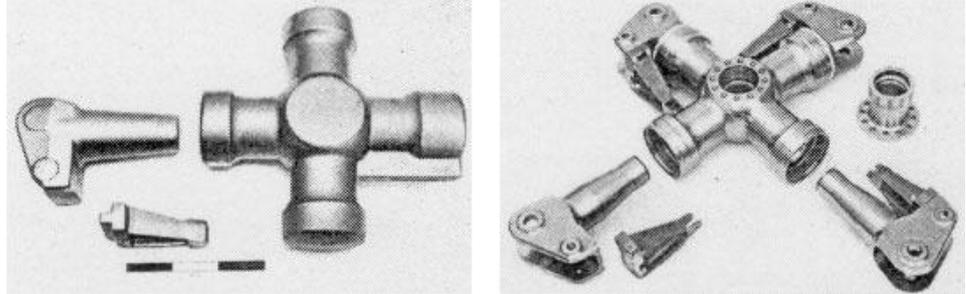
Figure 2.18 – Forged rotor head of the BO 105 and BK 117 helicopters

Space applications

Due to the comparatively small payload of space vehicles, saving weight in these structures is even more important than in aircraft. For this reason, titanium alloys were used extensively in the first Apollo and Mercury programs. Fuel and satellite tanks are regarded as a standard application for titanium alloys. Titanium's low weight, high strength, and long term chemical compatibility with fuel give titanium alloys an advantage over high-strength steels. Furthermore, the integrity of the tanks must be reliably nondestructively tested before being sent into orbit, which is most consistently done for metallic tanks. Non-metallic components require additional efforts to ensure their integrity. Figure 2.19 shows pressure vessels made from titanium alloys for the US Space Shuttle program.
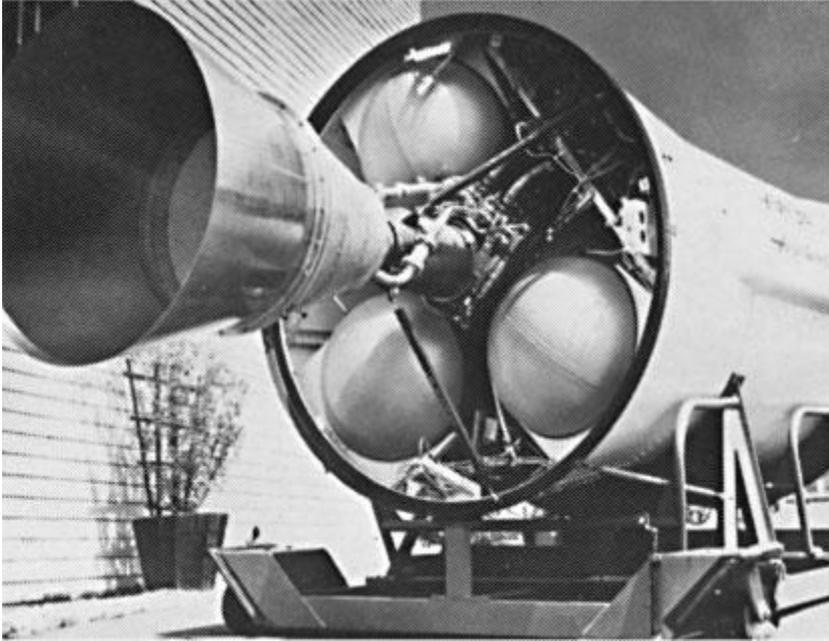
Figure 2.19 – Pressure tanks manufactured from titanium for space transportation systems

The requirement for extremely lightweight satellite component construction dictates very intensive, weight-optimizing manufacturing techniques. Under favorable conditions, the final fuel tank wall thickness in commonly used satellite propulsion systems is machined from 25 mm thick forged half-shells to less than 1 mm. This exceptionally high degree of machining can be drastically reduced by superplastic forming. Titanium sheet, 6 to 10 mm thick, can be superplastically formed to hemispheres and either simultaneously diffusion bonded or later conventionally welded to form a tank. Compared to conventional production by forging and machining, clear cost savings are obtained. Figure 2.20 shows a tank used for the Attitude Control System (SCA) on the Ariane 5. It was produced from two SPF half-shells that were TIG welded together. In addition to superplastic forming, cold-formable alloys provide another cost effective route. MAN Technologie AG uses such an approach to produce the fuel tanks for the ESA on the Automated Transfer Vehicle (ATV) for the International Space Station (ISS). The Ti-

15-3 tank half-shells are formed by a special, patented cold rolling process called counter-role spin forming.

Ti-3Al-2.5V was developed, among others, for low temperature applications and shows good toughness and ductility down to cryogenic temperatures. Therefore, it is used for high-pressure piping in the hydrogen pumping systems of the US Space Shuttle.

Figure 2.20 – Attitude Control System (SCA) tank of welded Ti-6Al-4V SPF half shells

2.6.3 Automotive

In the mid-1950s, titanium was already first used in the automotive industry. The turbine-driven, experimental vehicle of General Motors, the Titanium Firebird II, had an outer skin manufactured completely from titanium. The vehicle, which never went into production, also remained the only car with a titanium skin; except for ground-bound high speed racing cars developed later, which needed temperature protection from aero-kinetic heating.

Since then, however, it has been a constant objective of the titanium industry to penetrate the mass market of the automotive industry, even if it were only with niche products. Growing demand for fuel-efficient and environmentally friendly cars requires reduced weight at simultaneously improved performance. Titanium alloys, with their high specific strength and excellent corrosion resistance, were the materials of primary choice. The higher price of titanium has, however, proven to be a major stumbling block for wide spread automotive application, and use was initially limited to the racing and high performance sports car sector such as Formula 1 racing cars, competition motorcycles, and high-end automobiles, such as Ferrari. In the late 1990s, Toyota succeeded in being the first mass production automobile manufacturer to introduce titanium engine valves into a series production vehicle in Japan. But the "Altezza" is a mid-size family car and not, as one might have expected from the higher costs of titanium, an automobile in the high price market. A powder metallurgy route is used to manufacture the titanium valves. Ti-6Al-4V/TiB powders are used for the intake valves, while the high temperature outlet valves are manufactured from Ti-Al-Zr-Sn-Nb-Mo-Si/TiB powders. The Altezza's 2-l engine has 16 valves, which together weigh only about 400 g compared to almost 700 g for steel valves. The lower weight allowed valve springs to be re-dimensioned with corresponding additional weight savings. Other titanium applications in the power train connecting rods in the Acura NSX V-6 engine and engine valves in Nissan's Infiniti V-8 motor. Also, Yamaha uses titanium valves for one of its recent 250 cm^3 motocross engines.

Automotive coil springs are ideal components for which substitution of steel by titanium can be quite economic. In particular, the relatively low modulus of elasticity or, more exactly, the low shear modulus of titanium alloys, which is only about half that of steel, is of central importance. Compared to conventional automotive coil spring material, the lower modulus translates to increased coil deflection, resulting in fewer coil turns for a given spring application. Therefore, weight is not only reduced by the lower density of titanium, but also by the more compact height of the springs, thus allowing increased payload, and increasing engine or passenger compartment space. Theoretically, titanium springs would account for a "lightweight factor" of 3 to 4. However, due to the portion of inactive coil, weight savings in practical applications amount for little more than 50%. Finally, titanium springs

need no corrosion allowance or coating due to their inherent corrosion resistance.

For quite some time, Formula 1 racing cars have made use of the advantages of titanium springs, which are also used in motorcycle racing. However, the Volkswagen group was the first in the world to introduce titanium springs into a series

Figure 2.21 – Worldwide first commercial series production of titanium springs for rear suspension of the Volkswagen Lupo FS

production vehicle. Again, it wasn't an expensive model of the upper class, but the Lupo "FSI", a compact car that has been equipped with titanium rear suspension springs since the year 2000 (Figure 2.21). TIMETAL LCB (Ti-6.8Mo-4.5Fe-1.5Al) was chosen instead of the traditional Ti-6Al-4V alloy. On the one hand, since it is a beta alloy, it has a particularly low shear modulus, which is even lower than that of standard α+β alloys and thus further increases the physical advantage. Additionally, the alloy is also cheaper than Ti-6Al-4V. Like the name LCB (low-cost beta) implies, expensive vanadium was replaced by iron, allowing less-expensive Fe-Mo master alloys to be used. To keep the production costs of the springs at acceptable levels, the spring manufacturer, Muhr and Bender in Attendorn, Germany, paid much

attention to adapt existing processes utilized for steel to the production of the titanium coil springs.

The exhaust system is another attractive component in the automotive industry for using titanium. The Austrian sports motorcycle manufacturer KTM uses a rally exhaust system manufactured from titanium for its motocross engine "LC8". The wall thickness of the muffler is as thin as 0.3 mm for weight reduction. Remus, a world-wide leader in sport exhaust systems, offers sport exhausts for motorcycles with a titanium casing weighing as little as 2.5 kg. Reduced weight and even more – a lifetime guarantee – were primarily decisive for the introduction of the first series production titanium exhaust system in the automotive industry. Since 2001, General Motors Corp.'s sports car Chevrolet Corvette Z06 has been equipped with exhaust system subassemblies completely manufactured from titanium Grade 2. Compared with 18.6 kg for the stainless steel alternative, the titanium muffler weighs only 11 kg. Although worldwide consumption of titanium for automotive applications exceeded 1000 tons in 2002, which is more than an order of magnitude higher than in 1995, the high cost of the raw material is still a central problem for widespread application. For the near future it is not expected that titanium prices will lower drastically. Hopes are, however, that in a high-volume industrial market, prices could very well be reduced to half or one third those known for aerospace, which would in turn open new opportunities for titanium in the automotive industry.

2.6.4 Medical applications

Right at the beginning of the new millennium medicine history was written. But unlike the first successful heart transplantation on December 3rd, 1967, at the Groote-Schur hospital in Cape Town, South Africa, the implantation of the first artificial heart into the body of Robert Tools was almost unnoticeably carried out at the Jewish hospital in Louisville, Kentucky, USA, on July 2nd, 2001. The two surgeons from the University of Louisville, Laman Gray and Rob Dowling, will also probably never attain the fame and publicity of the South African surgeon Christian Barnard in the 1960s; however, the company ABIOMED from Danvers, Massachusetts, may possibly. They developed the first artificial

implantable replacement heart AbioCorTM shown in Figure 2.22. The fully implantable prosthetic system weighs nearly 1 kg, is about the size of a grapefruit, is entirely self-contained and estimated to cost about $ 70000. Apart from many soft tissues and plastic tubing, the metallic parts of the artificial heart, like connectors, valves, etc., are manufactured from c.p. titanium.

This pioneering work underlines the important progress titanium and its alloys have made as surgical implant materials in medical engineering within the last 30 years. The excellent compatibility with the human body is regarded as a key property for the choice of titanium: Titanium is generally perceived as the biocompatible metallic material. Furthermore, titanium is extremely resistant to corrosion from body fluids, and is compatible with bone and living tissue, and is elastically deformable as thin foil material. Thus, pure titanium combines many of the attributes desirable for heart pacemaker cases and as the carrier structure for replacement heart valves.

If implants have to carry mechanical loads, titanium alloys are used. Their outstanding strength to weight ratio and excellent fatigue behavior are decisive for the choice of material for orthopedic devices. Favorable to other high-strength metallic materials, titanium has a relatively low modulus of elasticity, which reduces the differences in stiffness between the human bone and the implant. This is important, for example, to the traditional application of titanium alloys as hip implants (Figure 2.23) and knee joints, but also to bone fracture plates and screws, and intramedullary nails or plates for cranial surgery. Titanium alloys are further

Figure 2.22 – The metallic parts of the first artificial heart are made of titanium

Figure 2.23 – Components of a hip implant made from cast titanium

used to substitute parts of the shoulder, the spine, the elbow, and the hand. External bone-fracture fixation provides another area for titanium applications. Since titanium withstands repeated sterilization, instruments for heart or eye surgery are made from titanium.

Initially, the standard titanium alloy Ti-6Al-4V was chosen for medical applications, since engineers could take advantage of an extensive database available from aerospace applications, particularly on fatigue behavior. However, in the course of the discussion around the toxicity of the element Vanadium, V-free alloys were specifically

developed for medical applications. In alloys like Ti-5Al- 2.5Fe, Ti-12Mo-6Zr-2Fe, Ti-15Mo-3Nb-3Al, Ti-6Al-7Nb, Ti-13Nb-13Zr, Ti-35Nb-7Zr- 5Ta, and Ti-30Ta, Fe, Nb, Ta, or Mo replaces Vanadium. At the same time, orthopedic alloys gradually shifted from α+β alloys to metastable β alloys, since – compared to Ti-6Al-4V – they have a lower Young's modulus, which comes closer to that of the human bone (10–30 GPa).

Titanium is non magnetic. This allows surgery in the magnetic field of a nuclear spin tomograph. Also, the risk of damage to small and sensitive implanted electronic devices is virtually eliminated.

In connection with medical applications, one class of titanium alloys is becoming integral to the design of a variety of new products. Actually, these are nickelbased titanium alloys and are better known as shape memory alloys: they remember their initial shape after being deformed. Moreover, they are able to undergo large elastic deformations and show high kink resistance and stability of shape. The super-elastic effect was discovered in the 1960s and has led to medical applications primarily for the Ni-Ti alloy Ti-56Ni. Like titanium alloys, they are also chemically and biologically compatible with the human body. For shape memory alloys, generally one-way effects, two-way effects, and pseudo-elasticity, also described as super-elasticity, are distinguished.

Materials with a one-way effect remember their original shape after being deformed at lower temperatures. Once heated to a higher temperature, they spring
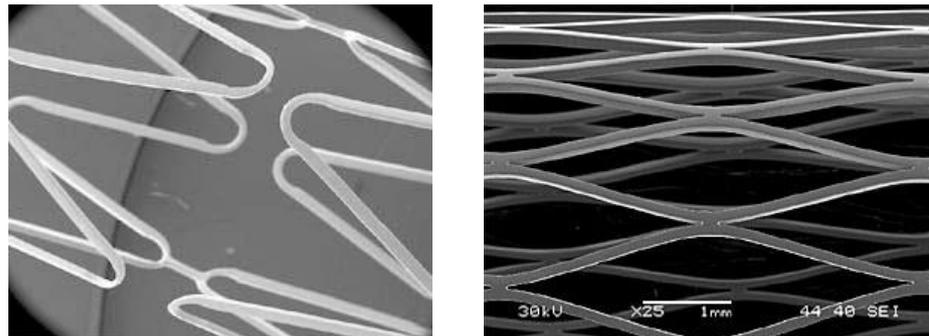
Figure 2.24 – Ni-Ti stent for medical applications

back to their original shape and keep it even when cooled down again. The metallurgical background of this phenomenon is that shape memory

alloys undergo a phase transformation in their crystal structure when cooled from the stronger, high temperature austenite to the weaker, low temperature martensite. The potential transformation temperatures range from –20 °C to +80 °C and can be adjusted by slight changes in alloy composition and through heat treatment. Ni-Ti alloys, which can be deformed at room temperature and retransform at 50–70 °C, are used today in surgery as implants (osteosynthese) and for stiffening of weakened fabrics. Probably the most celebrated application is the self-expanding stent (Figure 2.24) applied in the cardiovascular system. These permanent implants are deployed through a catheter and expand by simply returning to their equilibrium, non-deformed shape.

As the elasticity of Ni-Ti alloys can be more than 20 times greater than stainless steel, the shape memory effect is also employed for the occlusion of arterial defects thus avoiding open-heart surgery. A Ni-Ti wire mesh filled with polyester fabric is implanted through a catheter inserted in the patient's vein. Once the occlusion or hole in the arterial wall of the heart is reached, it springs open, expanding to its original shape and clamps the defect.

Applications outside medical engineering include pipe joints and body-bound rivets as well as plug-in connections of circuits. For two-way effects, the shape memory process is reversible. Upon thermal cycling the material also deforms cyclically. This behavior is utilized for control of endoscopic instruments. Outside medical engineering, the two-way effect is used in electrical engineering and electronics for heat and electrical installations, as well as in the automotive industry as measuring and control elements, e.g. engine valves, manipulators, or small robots.

The third form is pseudo-elasticity, or super-elasticity. Here the reversible austenite-martensite-austenite transformation is forced by an external deformation. Such a pseudo-elastic material can bear very high deformations and is used as a material for braces, for example. In fact, orthodontic archwire was the first product to take advantage of this property. Ni-Ti wires are able to move with the teeth, applying a constant force over a very broad treatment time and tooth position. Another popular application outside medicine is as seals. Super-elastic eyeglass frames became the first successful Ni-Ti consumer product. Since Ni-Ti components show a ten-fold higher elastic straining than conventional spring materials, they are also suitable for applications where high damping is essential.

CHAPTER 3

Literature review of titanium welding

3.1 Introduction

Welding technology has had great development in recent decades. It has diversified into several processes. Undoubtedly the most common and used industrially are arc welding processes. This development was due primarily to the need to reach higher productivity and the need to extend the fields of applicability of individual processes in materials. Thickness and shapes of the joint increasingly diversified.

The traditional welding technologies applied now in low productivity sectors and repairs in 'situ', such as oxyacetylene welding and manual welding with coated electrode, although based on established principles for decades, have had a strong evolution with the advent of electronic digital control. This is particularly in reference to MIG, TIG and plasma technologies which have taken on a new life with the introduction of modern sources based on the "inverter" technology and with adjustment of process parameters by means of digital control units.

Autogenous welding processes for fusion is not limited to the so-called "arc technology." In recent decades, innovative processes have emerged with great force on the industrial landscape that are based on completely different physical principles and are of great practical interest. Among these new technologies, the electron beam and laser processes prove to be particularly significant. Their intrinsic characteristics allow the identification of a further subdivision of welding processes: processes for fusion with an autogenous source of highly concentrated energy. This new classification considerably differentiates the laser and electron beam technologies from conventional ones. The energy source used to melt the base material can be concentrated on very small surfaces so as to obtain energy density up to 10,000 times higher than those of the arc processes.

Between the two technologies mentioned above, laser processes are encountering the most industrial interest. The processes based on electron beam sources possess some limitations such as the need to operate in a vacuum and the X-ray emission during processing restrict its use in specific situations.

3.2 Welding of titanium

Most titanium alloys can be fusion welded and all alloys can be joined by solid state processes. Indeed, Welds in titanium are substantially immune to many of the weld cracking problems that cause trouble with ferrous alloy fabrications. Despite this and other beneficial characteristics, some engineers still believe that titanium is difficult to weld, possibly due to its particular requirements with regard to gas shielding, or because it has normally been handled only by specialist fabricators. Titanium is actually easy to weld by most processes, as are most of its more common alloys. Embrittlement through contamination with air and carbonaceous materials poses the biggest threat to successful fusion welding titanium, so the area to be welded must be clean and protected by inert gas while hot. The means to protect the weldment with inert gas are commercially available and easy to implement. Welding consumables are readily available for the common titanium grades and specifications for welding wire are provided in AWS Specification A5.16. Permissible filler metal, normally identical to the parent metal, may be specified as in ASTM B 862. The weldability of titanium alloys is usually assessed on the basis of the toughness and ductility of the weld metal. Commercially pure grades are considered very easy to fabricate and are ordinarily used in the as-welded condition. Titanium alloys show reduced weld metal ductility and toughness. The table below highlights the weldability of the common ASTM titanium grades and other alloys. Technical consultation should be sought prior to designing or fabricating any of the titanium alloys, if there is any likelihood of problems arising from unfamiliarity with the materials concerned.

3.2.1 Gas tungsten arc welding

Tungsten inert gas welding is also known as tungsten arc welding and gas-tungsten arc welding (GTAW) and is currently the most commonly applied joining process for titanium and its alloys. Titanium is one of the easiest of metals to weld by the TIG process; the weld pool is fluid and its combination of low density and high surface tension enables good control of the weld surface profile and penetration, even when unsupported. An arc between the tungsten alloy electrode and workpiece obtains fusion of the joint region, while an inert gas (the torch gas) sustains the arc and protects the tungsten electrode and molten metal from atmospheric contamination. The inert gas is typically argon, but a mixture of helium and argon can be used to increase penetration or speed. Welds can be made autogenously (without filler addition) or with addition of a consumable wire into the arc. The TIG process is fully capable of operating in all welding positions and is the only process that is routinely used for orbital welding. Specialist orbital welding equipment is commercially available for a wide range of component diameters and often has the added advantage of incorporating the inert gas trailing shield necessary for titanium fabrication. Higher productivity variants of the TIG process have been applied to titanium. Hot wire TIG enables a greater fill rate to be achieved, improving productivity on multipass welds required for heavier section thicknesses. Activated TIG (A-TIG) achieves deeper penetration through the use of a special flux sprayed onto the joint surfaces prior to welding. The latter process has had particular success for welding stainless steels, but its potential application to titanium joints has yet to be fully exploited.

3.2.2 Gas metal arc welding

The MIG process has not been applied as widely to titanium as it has been to ferrous and other non-ferrous alloys. Many of the historical reasons why MIG welding has not been favoured for titanium no longer apply. High currents are required for stable metal transfer and the poor surfaces originally produced on titanium wire caused rapid contact tip wear. More recently, the combination of modern inverter power sources

with pulsed currents gives more stable metal transfer, whilst the improved surface finish of titanium wire has reduced contact tip wear such that the problem is barely apparent in development work.

In MIG welding, an arc is generated between a continuously fed consumable electrode (a wire of matching composition to the base material) and theworkpiece. Spray transfer occurs above a critical welding current density and requires the use of direct current with the electrode positive. This method demands high currents and therefore high welding speeds, which in turn require long trailing shields, and effectively restricts the process to mechanised welding. Dip transfer, whereby the electrode comes into contact with the weld pool, can be used for semi-mechanised welding, typicallyfor sheet material, but defects, caused by lack of fusion, can be a problem. Pulsed MIG appears to be the most satisfactory process, especially when used in combination with argon-helium (Ar-He) shielding gas. MIG welding offers greater productivity than TIG welding, especially for completing thicker section joints. As yet the process has been typically applied to joints for which exceptional weld quality is not critical, e.g. appliqué armour plate, but with development the process may be capable of satisfying higher quality welding requirements. A disadvantage of the process is that some degree of weld spatter appears to be unavoidable. Spatter can be reduced by employing Ar-He torch shielding gas mixtures: the addition of helium acting to stabilise the arc. Even so, in most instances spatter removal poses no problem.

3.2.3 Plasma arc welding

Plasma arc welding retains the high quality associated with TIG welding whilst having significant penetration and speed advantages. Similar to TIG, heat is transferred by an arc generated between a tungsten electrode and the workpiece; but, in the PAW process the arc is constricted by a copper alloy orifice to form a highly collimated arc column. In addition to a surrounding shielding gas, a 'plasma gas' flows through the copper orifice and a portion of this is ionized producing the characteristic plasma jet. In the conduction-limited mode a weld pool similar to that produced during TIG welding is generated, whilst in the keyhole mode, the plasma jet fully penetrates the joint. Molten metal

flows around the keyhole and solidifies behind the plasma jet as the torch traverses along the joint line. In many ways the keyhole plasma arc process is akin to a slower version of one of the power beam processes (electron beam and laser welding). A third process variation exists, referred to as microplasma arc welding. This is simply a low current variant (typically 0.1-15 A) of the conduction-limited mode, suitable for producing small controlled weld beads. Welding is generally performed with continuous direct current with the electrode negative (DCEN), but a pulsed current can be used to broaden the tolerance window of welding parameters which produce acceptable welds.

Plasma arc welding offers significant productivity gains over both TIG and MIG, especially when operated in the keyhole mode. Although welds are only typically made in the 1G or 2G positions, single pass welds can be made in material up to 18mm thick. Furthermore, the keyhole PAW process appears to offer greater immunity to weld metal porosity than any other fusion welding process. Because introduction of filler into the arc can cause instabilities in the gas plasma, keyhole PAW is normally performed autogenously, thus a small amount of underfill is typical. Completing a second pass, adding filler with the same torch operated in the conduction-limited mode, or alternatively using TIG welding, can correct this. Pipe circumferential welding (e.g. pipe joints) is certainly possible, but requires a controlled slope-down of the plasma gas flow rate and arc power to avoid any porosity defects at the stop position.

3.2.4 Electron beam welding

Electron beam (EB) welding has traditionally been the preferred process for making critical joints in titanium alloys. High quality welds can be produced with low distortion and with high reliability. Productivity can also be good, especially for thick sections which can be welded readily in a single pass. Conventional electron beam welding is performed in a vacuum of about 10^{-4} mbar, requiring a sealed chamber and pumping system. This adds to the capital cost of the equipment, especially for large components. A further drawback for large components is the extended time it takes to achieve a vacuum in the chamber, decreasing productivity. However, electron beam guns have been designed which can operate at

lower vacuum or near atmospheric pressure. So called 'reduced pressure' electron beam (RPEB) welding shows great promise for decreasing costs and increasing productivity beyond that achievable using conventional EB welding. Simple seals can be used to isolate the joint region of a large component, which is evacuated to a pressure of around 10^{-1} mbar (achievable using inexpensive mechanical vacuum pumps). An RPEB steel pipe J-laying system is currently under development at TWI. High quality welds have also been produced in titanium alloy pipe and plate.

3.2.5 Resistance welding

Resistance welding of titanium is quite straightforward and is aided by the metal's high resistivity and low thermal conductivity. The associated processes rely on the heat generated by the resistance to electrical current flowing through the workpiece to fuse the metal with the joint. Shaped electrodes apply the current and pressure required to make a localised weld. As with other joining processes, cleanliness of the abutting joint faces is essential for a successful weld. Experience gained with stainless steels is relevant for resistance welding commercially pure titanium grades, since the resistivity and thermal conductivity of the two metals are similar. Titanium alloys, however, have quite different thermal and electrical characteristics and should not be welded using parameters established for stainless steel.

3.2.6 Laser welding

Laser welding is finding increasing application for titanium, for example in the production of welded tube and pipe. The process, which offers low distortion and good productivity, is potentially more flexible than TIG or electron beam for automated welding. Application is not restricted by a requirement to evacuate the joint region. Furthermore, laser beams can be directed, enabling a large range of component configurations to be joined using different welding positions. CO_2 lasers offer the greatest power range, with single pass welds possible in 20 mm thick titanium using 25 kW systems. Nd:YAG laser welding offers

superior flexibility due to the possibility of fibre optic beam delivery systems, but penetration is restricted by a lower power capability. Laser welds can suffer from weld spatter, which may pose a problem on the root surface, particularly if postweld access is restricted.

3.3 Laser welding mechanisms

The laser beam can be used to weld both metals and plastics. Although at an industrial level, the most widespread application is certainly the welding of metals - particularly steel.

Figure 3.1 is a schematic of the laser welding process. The laser beam heats the two edges for welding and brings them to a melting point. And as a result of the relative motion between the beam and the work-piece, when the laser moves away, the molten material cools and solidifies rapidly generating the weld bead.

During the welding operation there is a flow of gas to prevent contact of the heated zone with the atmospheric gases.
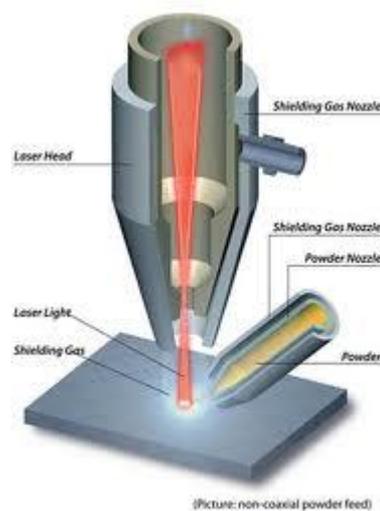
Figure 3.1 – Laser welding process

The laser welding can occur by two different ways:
- Conduction
- Key-hole

The most common in the industrial field is key-hole. This is typical of all technologies that use heat sources with high power density.

3.3.1 Conduction

Conduction welding (Figure 3.2) occurs when the power density of the laser spot is limited. The welding method is similar to the traditional one. The laser beam heats the material until it reaches its melting point; thus generating a pool of molten material that because of the relative motion between the work-piece and the beam, apparently moves with the beam.
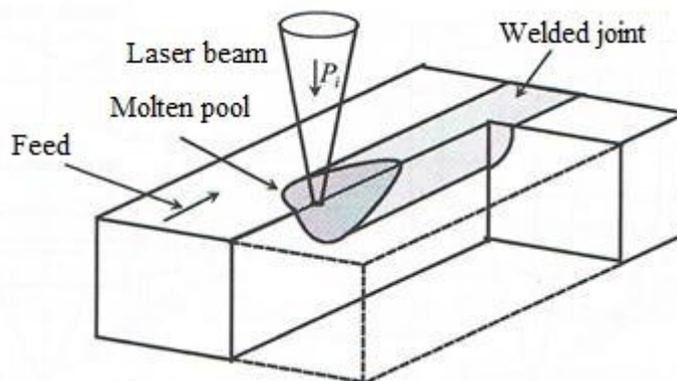
Figure 3.2 – Conduction welding

The geometry of a cross section of the bead is almost semi-circular with an aspect ratio (depth / length) approximately uniform. This geometry reflects the mode of heat diffusion. The laser beam can be assimilated to a punctiform source of heat which acts on the upper surface of the work-piece. The isotropy of the mechanism of heat conduction allows it to obtain a semi-circular geometry.

3.3.2 Key-hole

The key-hole welding (Figure 3.3) is obtained when the power density is sufficiently high to vaporize the material. The vaporization of the material leads to the formation of a vertical channel of vaporized metal called key-hole which develops in depth for the whole thickness of the work-piece. The mechanism of the key-hole (Figure 3.4) is based on the fact that the material exposed to the laser vaporizes very quickly and because of the sudden expansion, rapidly moves away from the area facilitating the further exposure to the beam of the material more in deep.
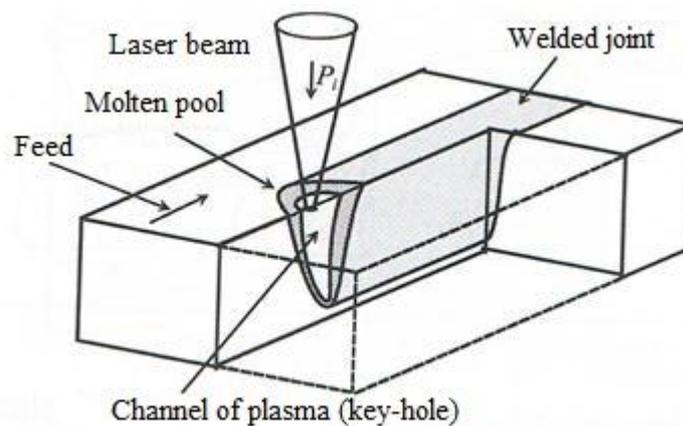
Figure 3.3 – Key-hole welding

The vaporization of the first surface layer causes the laser beam to directly irradiate the material in the underlying layer, generating a further vaporization. Proceeding with this mechanism, almost instantaneously, a very narrow and deep channel occurs.

The metal vapor within the channel absorbs the laser radiation, heats up and ionizes, becoming plasma.
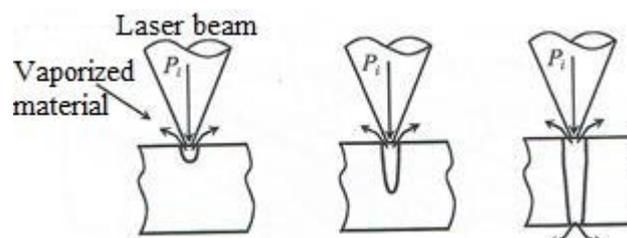
Figure 3.4 – Key-hole mechanism

During the relative motion between the beam and the work-piece, a condition of dynamic equilibrium is established. The material, close to the irradiated zone, is heated, melted and vaporized, generating high pressure inside the plasma channel which avoids the collapse of the channel under the action of the liquid material present on the side walls. The material behind the plasma channel quickly solidifies and generates the weld bead. The presence of the plasma channel is of great help for the penetration of the weld. In fact, the laser beam is actually absorbed by the plasma inside the channel itself, which in turn transfers it to the surrounding melt. In this way the heat is not absorbed from the surface of the piece, as was in conduction welding, but from the walls of the keyhole, and then in depth. In this way, the welding bead is particularly deep and narrow, which leads to a high quality weld.

The aspect ratio (depth / width) of a key-hole laser welding is much higher than 1:1 and can reach even 10:1.

In view of the advantages listed above, it is also appropriate to mention the drawbacks which are introduced by way of key-hole welding. First of all, it should be stressed as the creation of slim beads is not particularly suitable for materials susceptible to hot cracking since the growth of the dendritic structures towards the central part of the bead itself is hampered by the lack of available width. This situation may facilitate the segregation of impurities and low melting elements at the axis of the melted zone giving rise to a face of poor mechanical strength which can promote the formation of cracks during the cooling phase caused by transverse stresses.

Even the plasma, in addition to the advantages described above, is mainly the cause of two effects: absorption of the energy emitted by the beam with a consequent decline of the efficiency of the process and defocusing of the beam due to refraction taking place within the cloud same with a consequent decrease of the energy density characteristic of the process.

3.3.3 Conduction/Key-hole threshold

The two modes of laser welding are different because in key-hole welding the vaporization of material occurs, which is almost not existent

in conduction welding. Since vaporization is a threshold process, as it occurs above a certain temperature, even the passage from one mechanism to another does not take place continuously, but at a certain value of power density, which means that above this threshold value the key-hole occurs (Figure 3.5).
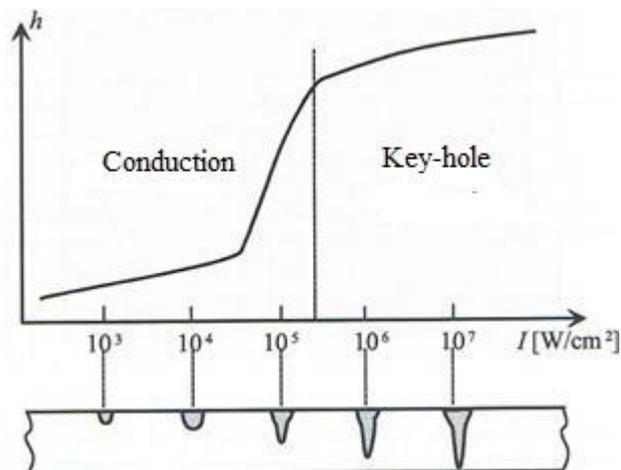
Figure 3.5 – Conduction/Key-hole transition to vary irradiance

Consider as an example a butt welding between two steel plates of equal thickness and imagine performing different tests increasing irradiance (obtained by increasing the power of the beam or reducing the spot). For low values of irradiance the welding mechanism is by conduction, and then the geometry of the generated bead is almost semi-circular shape with an unitary aspect ratio. Increasing power density, the size of the bead increases because of higher power entering the work-piece while the aspect ratio remains unchanged.

Further increasing the power density and sudden increase in the depth of penetration occurs without there being a similar increase in width and then the mechanism that is established is a key-hole welding and the aspect ratio deviates substantially from the unit value. The threshold of irradiance between conduction and key-hole depends primarily on the material and for steel is about 10^6 W/cm^2. Furthermore, the threshold is almost independent of the welding speed, which affects the geometry of the bead because at lower speeds correspond beads of smaller dimensions.

3.4 Laser welding parameters

In laser welding, there are several factors that can affect the process, acting on the final geometry, on defects and on properties of the joint. In the following sections, the most important and significant are described.

3.4.1 Welding speed

Welding speed is one of the most important variables in laser welding. It is dependent on the main geometrical and microstructural characteristics of the bead as in the case of key-hole welding as conduction welding and consequently, welding speed directly affects the performance of the joint.

By increasing welding speed, the size of the weld bead decreases, both in terms of maximum depth and of the transverse dimensions.(Figure 3.6).

Transverse dimensions are closely linked to thermal distortions. As a result it is obtained that welding speed has great influence on the distortion of the component and residual stress of the welded area.
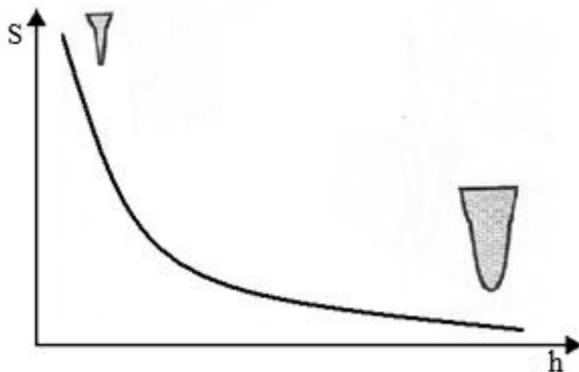
Figure 3.6 – Weld bead geometry to vary welding speed

3.4.2 Irradiance

Beam irradiance (defined as power / spot area ratio) is the only factor that regulates the switch from conduction to key-hole mechanism.

Therefore, to switch from one mechanism to another, the only variable on which to act is the beam irradiance.

Usually, increasing irradiance increases the bead depth. In case of not fully penetrated key-hole welding, an irradiance too high may be damaging. It could be at risk of having an excessive amount of plasma that remains inside the bead generating porosities dangerous for the mechanical strength of the joint. Acting on welding speed and on irradiance therefore makes it possible to reduce the transverse dimensions of the bead and increase the penetration depth.
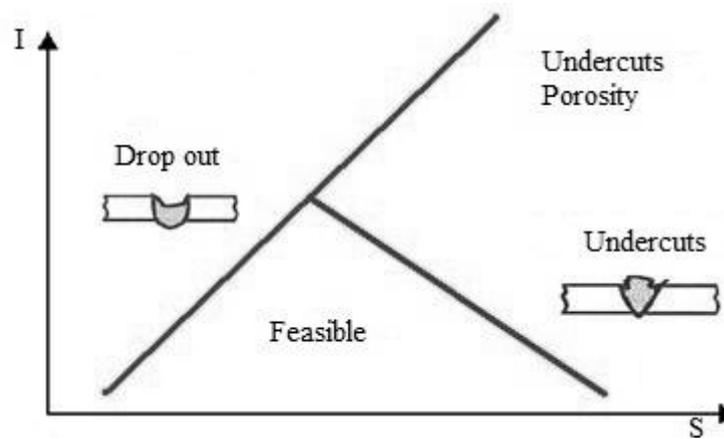
Figure 3.7 – I-S plane with the zones of feasibility

Figure 3.7 shows a diagram of welding speed vs. irradiance where each area has certain characteristics. The typical defect that occurs when the power values are too high and welding speed too low is the "drop-out" in which the molten pool is drawn downward by the action of gravity. Therefore, by using speed values too high the typical defects are "undercuts". And coupled with high power porosity, could appear in the case of not fully penetrated beads.

In key-hole welding, an excess of irradiance can lead to a decrease of penetration depth. In fact, the plasma is not transparent to the beam. And the superimposition of plasma which occurs increasing power, leads to a masking of the beam making it impossible to reach the piece below.

3.4.3 Focus position

Often in the key-hole welding it is better to position the focus below the upper surface of the work-piece as it is the condition which allows to obtain the maximum penetration depth. It is however necessary that the irradiance on the upper surface is sufficient to enable the triggering of the key-hole.

In laser welding the maximum weldable thickness is closely related to the depth of focus of the beam. As already mentioned in the chapter 1, the depth of focus can be useful to compare different optical conditions. But to understand the real depth of focus, it is necessary to perform an experimental test.

This test is based on an evaluation of the trigger of key-hole on an inclined plane as shown in Figure 3.8. Whereas the inclination of the plane (θ) in respect to the normal to the beam and the distance between the point at which the key hole triggers (x_{in}) and one in which defuses (x_{out}) we can calculate the real depth of focus as follows

$$\Delta z = |x_{in} - x_{out}| \sin \theta \qquad (21)$$
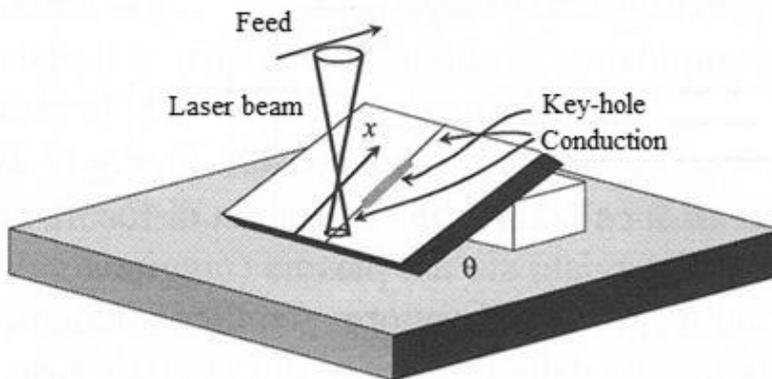
Figure 3.8 – Test to find the field depth in which key-hole occurs

3.4.4 Shielding gas

The shielding gas has the following functions:

- Replace the Atmosphere: The shielding gas has to replace the atmosphere to prevent the emergence of problems of oxidation or nitriding.
- Remove the Plasma: During key-hole welding, a large amount of plasma is generated. This ionized gas escapes from the key-hole and must be rapidly removed because it is capable of absorbing electromagnetic radiation. Therefore, the presence of plasma obscures the beam, reducing the incident power.
- Protect the Focusing System: The focusing system (lens or mirror) can be damaged from plasma (reaching the cold surface of the lens or mirror, the metal vapor condenses and is deposited, thereby contaminating the surface) and from the spatters of molten material. In both cases, the gas flow helps to prolong the life of the focusing system.
- To influence the Chemistry of the Molten Pool: As the atomic diffusion is favored by the temperature, the gaseous flow can be selected in such a way as to influence slightly the chemistry of the molten pool and consequently, the characteristics that the bead has at room temperature.

The gases most often used in laser welding are argon, helium and nitrogen. CO_2, which is particularly used in MAG proceedings, is not indicated in this case because it is more absorbent than the characteristic wavelengths of the beams generated by gaseous active gains.

Helium has a rather high ionization potential. Therefore, it is very suitable to cover the area immediately surrounding the point of incidence of the beam on the material, as it helps to suppress plasma formation. The helium, however, is particularly volatile and tends to escape very quickly from the coverage area thus determining the need to employ very high flow rates resulting in increased processing costs.

Argon has a lower ionization potential, and therefore is not well suited to cover the area in direct contact with the laser beam. This is especially true if the process is characterized by the use of sources of power exceeding 3 kW. Its high density, however, makes it suitable to perform

the function of widespread coverage on the bead during solidification for the upper and lower surfaces.

Nitrogen has an ionization potential comparable to that of argon and a density very close to that of the atmosphere. Not being an inert element, it may give rise to unwanted chemical reactions especially with the more reactive metals. The advantage of this gas is that it is much less expensive than helium and argon.

Whereas all the functions of the shielding gas described above, and that in the industrial field the welding speed can be of various m / min, it is obvious that often a single nozzle is not sufficient to ensure a good isolation from the atmosphere and an adequate removal of the plasma. Therefore, more effective systems are necessary that include a flow concentrated directly at the base of the plasma and a more widespread system that allows adequate coverage of both the melting and solidification of the bead.
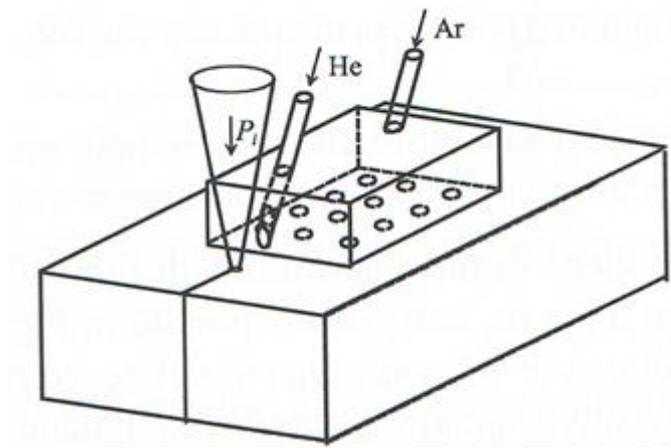
Figure 3.9 – Scheme of a shielding system

In some applications, a particular device could be used, (Figure 3.9) for the supply of different gases in different zones of the bead. Helium in the area in which key-hole occurs with the function to reduce and remove plasma and argon in the following area with the aim of being able to cover the bead and maintain low temperatures.

3.5   Laser welding of Ti6Al4V

The conventional welding methods used for titanium alloys are tungsten inert gas and plasma arc welding. In recent decades, autogenous processes with highly concentrated energy sources have become popular; these joining processes are laser and electron-beam welding. However, limited literature on laser welding of Ti6Al4V alloy is available, and most reports have concentrated on the use of CO_2 lasers.

3.5.1 CO_2 laser welding

Sun et al. have compared the parameters and microstructures for TIG, plasma, and CO_2 laser welding of Ti6Al4V. In terms of the microstructures, higher current levels for TIG and plasma, as well as lower speeds for laser welding, produced larger grain sizes due to the increase in heat input. Laser welds produced much smaller grains than both TIG and plasma. The hardness of the fusion zone increased with increasing welding current for both plasma and TIG welds, and with increasing welding speed for laser. Laser welding produced much harder welds than either plasma or TIG welding due to the high cooling rate. Caiazzo et al. have studied the effect of applying shielding protection with helium and argon gases on titanium alloys, using different nozzle designs, a study using a CO_2 laser was conducted, and the results showed that, at constant power, for each welding speed examined, a greater penetration depth was obtained with helium gas than argon due to the lower ionization energy of argon, which reduces energy transfer to the material. Furthermore, the shielding gas protects the melted material from oxidation that can cause defects, such as porosity and cracks; this porosity is caused by gas bubbles in the melted material that cannot escape before solidification.

3.5.2 Nd:YAG laser welding

Compared with the CO_2 laser, Nd:YAG and fiber lasers have become more widely used in recent years due to the shorter wavelength of these latter sources, which results in a more stable keyhole and weld pool with higher welding efficiency than the former.

Cao et al. have welded Ti6Al4V alloy sheets with nominal thicknesses of 1 and 2 mm using a Nd:YAG laser system. It was found that the fusion zone area and width decrease with increasing welding speed, the undercut depth decreases with increasing welding speed, some microporosity might appear in the 2-mm joints, no solidification cracks were observed in the fusion zone, but heat affected zone (HAZ) cracking was occasionally found. Compared to the base material, the laser weld joints have similar or slightly higher joint strengths but a significant decrease in ductility due to the presence of micropores and aluminium oxides.

Akman et al. have used a pulsed Nd:YAG laser welding to join Ti6Al4V, and porosities in the melted material were found to have a great effect on the tensile strength. An increase in porosity from 0.5% to 2% reduced the tensile strength from 500 MPa to approximately 160 MPa.

CHAPTER 4

Material, equipment and experimental work

4.1   Introduction

The aim of the thesis work is to find the better input process parameters values to weld 3 mm and 1 mm Ti6Al4V sheets using a 2 kW Yb:YAG disk laser.

Both bead on plate and butt tests have been performed, and the beads quality is characterized in terms of geometric characteristics, porosity content, microstructure, hardness and strength.

In this chapter, the first part describes the alloy of interest, equipment and methodologies by which the welds are made and analyzed. The second part of the chapter discusses the experimental designs used.

4.2   Material

The material under investigation is the Ti6Al4V alloy which is an $\alpha+\beta$ titanium alloy. Ti6Al4V is known as the "workhorse" of the titanium industry because it is by far the most common titanium alloy, accounting for more than 50% of total titanium usage and is the most widely used in the aerospace and automotive industries. Ti6Al4V offers a combination of high strength, light weight, formability and corrosion resistance which have made it a world standard in aerospace applications. This alloy may be considered in any application where a combination of high strength at low to moderate temperatures, light weight and excellent corrosion resistance are required. Some of the many applications where this alloy has been used include aircraft turbine engine components, aircraft structural components, aerospace fasteners, high-performance automotive parts, marine applications, medical devices and sports equipment.

The Ti6Al4V alloy is a titanium-based alloy containing 6% aluminium and 4% vanadium. As the pseudo-binary phase diagram shows (Figure 4.1), at room temperature the alloy is bi-phasic Tiα+Tiβ, with a slight phase percentage of Tiβ. The existence of the two phases, Tiα and Tiβ, at room temperature makes it possible to obtain an alloy with a high mechanical resistance due to the mutual interaction of the two phases. During heating, Tiα transforms into Tiβ at approximately 980°C. During fast cooling, the Tiβ phase undergoes a so-called martensitic transformation, forming a complex lamellar structure inducing significantly altered mechanical properties. These mechanical properties can be recovered by a low-temperature thermal treatment.
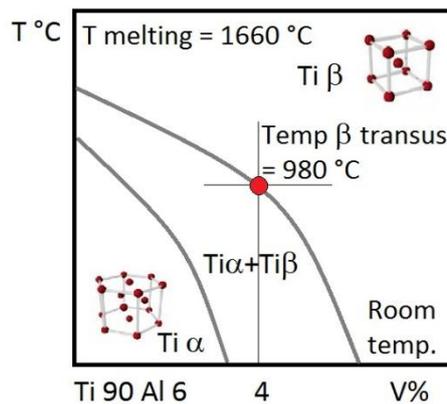
Figure 4.1 – Pseudo binary phase diagram of Ti6Al4V

The alloy under investigation is Ti6Al4V (Grade 5) whose chemical composition and mechanical property are given in Table 4.1

Table 4.1 - Nominal composition and property of Ti6Al4V

C	Fe	N_2	O_2	Al	V	H_2	Ti
<%0.08	<%0.25	<%0.05	<%0.2	<%5.5	<%3.5	<%0.0375	Balance

Density [kg/m^3]	Ultimate Tensile Strength [MPa]	Yeld Tensile Strength [MPa]	Elastic Modulus [GPa]	Hardness Rockwell C	Elongation at break
4400	1170	1100MPa	114	36	10%

4.3   Equipment

The experimental work was performed at the laboratories of "Technology and Manufacturing Systems" at the University of Salerno. In the next sessions the equipment and the experimental modalities are described.

4.3.1   Laser TruDisk2002

The laser used is the Trumpf TruDisk 2002 (Figure 4.2), whose active medium is a 200-µm-thick Yb:YAG disk longitudinally excited by diodes. The rear face of the disc is treated so as to form the rear mirror of the resonator and is also in contact with an appropriate heat sink . This geometry, with excitation and longitudinal cooling, considerably reduces the phenomenon of thermal lens typical of rod configurations as discussed in Chapter 1. With a negligible thermal lens, it is possible to obtain a beam quality much better than that provided by rod systems at the same generated power. This device produces a beam of maximum power of 2000 W and a minimum equal to 80 W.

Figure 4.2 – Trumpf TruDisk 2002

The laser beam is guided to the welding head through the use of a flexible optical fiber; and here is focused by optical glasses (Figure 4.3). The optical system D70 has a collimation lens with a focal lenght f_C = 200 mm and a focusing lens with a focal length f = 200 mm. The minimum diameter of the laser beam is defined as focus diameter $d_{0f} = \frac{f}{f_c}\, d_k$, where d_k represents the diameter of the fiber core and is 0.3 mm.
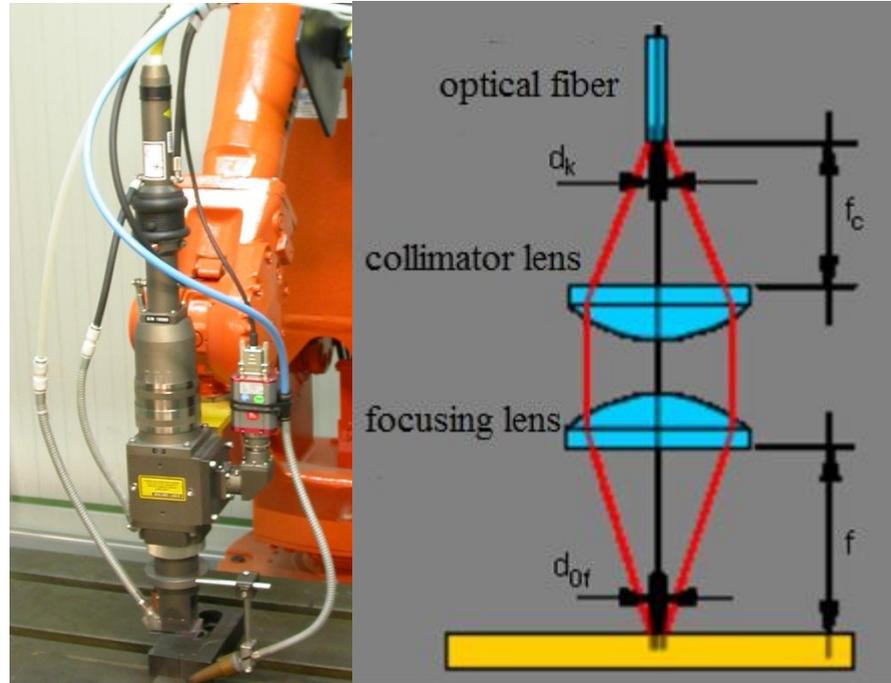
Figure 4.3 – Welding head and focusing system

The active medium generates a laser wavelength of 1.03 μm and the beam (Figure 4.4) has a Rayleigh distance of ± 2.8 mm.
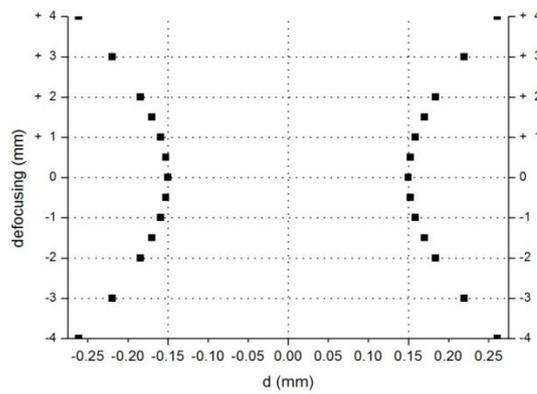
Figure 4.4 – Beam profile

Table 4.2 shows the main characteristics of the laser used.

Table 4.2 - Yb :YAG disk laser technical data

Active medium	Yb:YAG
Wavelength	1030 nm
Range power	80 – 2000 W
Beam quality	8 mm*mrad
Focal length	200 mm
Fiber diameter	300 μm
Focus diameter	300 μm

4.3.2 Robot ABB IRB 2400

The laser head is moved by a 6-axis numerically controlled robot ABB IRB 2400 (Figure 4.5). This is a 6-axis industrial robot, designed specifically for manufacturing industries that use flexible robot-based automation. The robot has an open structure that is specially adapted for flexible use, and can communicate extensively with external systems.

IRB 2400, gives excellent performance in material handling, machine tending and process applications. IRB 2400 offers increased production rates, reduced lead times and faster delivery for manufactured product. IRB 2400 is the world's most popular industrial robot The robust construction and use of minimum parts contribute to high reliability and long intervals between maintenance. Thanks to the ABB´s unique motion control of the robot optimizes the acceleration and retardation, which results in shortest cycle time possible. Best in class regarding path accuracy and position repeatability (RP = 0.06 mm). Payload options are between 7 -20 kg. Max reach 1.810 m. The robot is equipped with the IRC5 controller and robot control software, RobotWare RW. RobotWare RW supports every aspect of the robot system, such as motion control, development and execution of application programs communication etc.

Figure 4.5 – Robot ABB IRB 2400

4.3.3   Shielding system

In welding titanium alloys, the shielding melt pool is very problematic because, compared to other materials, titanium has a high affinity for environmental vapours and gases at temperatures above 300 °C. The bead colour analysis indicates the thickness of the superficial oxide. Silvery, golden and blue colours indicate a thickness of the oxide film less than 10 nm, between 10-25 nm and between 25-70 nm, respectively. A generally acceptable level of contamination is represented by gold, but in aircraft applications for example, it is desirable to obtain a complete absence of colour.
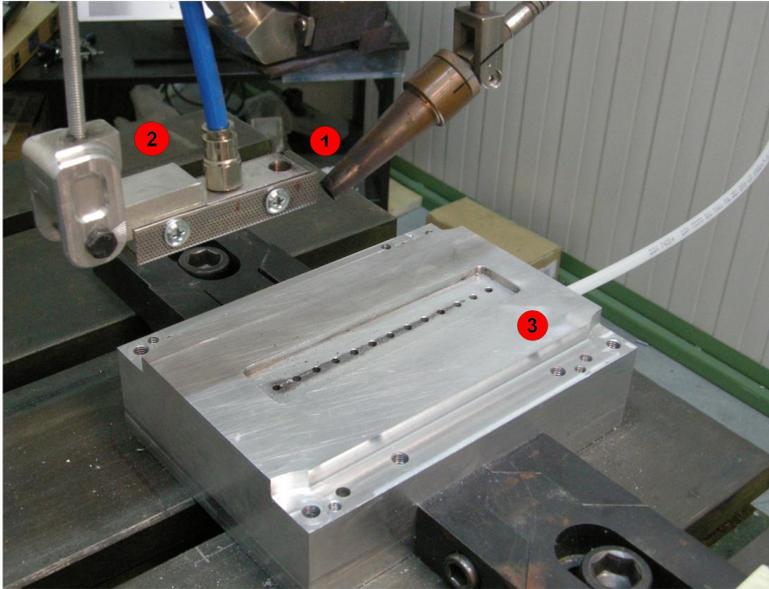
Figure 4.6 – Shielding system

The shielding system is composed of a nozzle (1), an upper diffuser (2) and a lower diffuser (3) onto which the plates were fixed (Figure 4.6). Both diffusers were designed and manufactured in our laboratory. The upper diffuser has two degrees of freedom, making a more flexible system in terms of distance from the beam axis and distance from the workpiece surface. The upper diffuser allows to an uniform layer of argon on the sheet upper surface using a micro-drilled holes plate. To determine the optimal values of the parameters related to the positioning of the nozzle and the shielding gas type and flow rate, preliminary tests were performed to obtain silver weld beads and several configurations were tested. The protection system was equipped with two shielding gases, and the best configuration was: helium in the nozzle at a flow rate of 20 Nl/min which, because of its high ionization potential, has been used to create a cloud of protection that prevents plasma formation. The lower surface and the upper surface were shielded using argon. The lower diffuser protects the root of the bead from oxidation when full penetration or excessive penetration occurs. The upper diffuser protects the top of the bead after passage of the beam to reduce oxidation during cooling. Argon was released from the upper diffuser at a flow rate of 20 Nl/min and from the lower diffuser at a flow rate of 10 Nl/min. The best results were

obtained with the nozzle above the laser beam in the direction of motion. The centre of the outlet nozzle was 4 mm from the beam and 2 mm from the top surface of the plate. The axis of the nozzle made an angle of 40° with respect to plane of the plate (Figure 4.7).
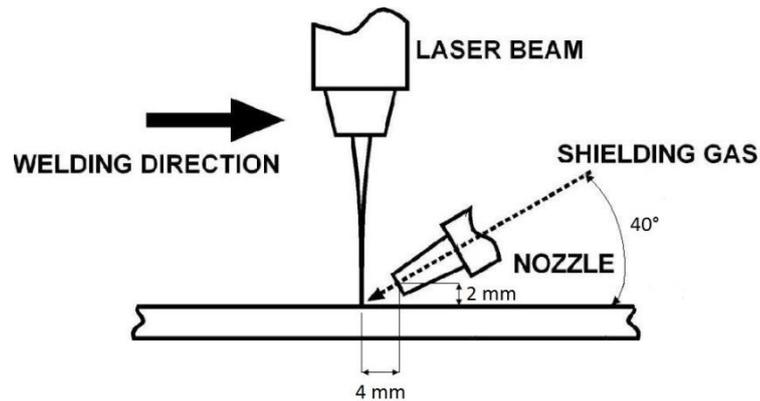
Figure 4.7 – Shielding nozzle setup

4.3.4 *Samples preparations*

Both butt and bead on plate welds were cut in orthogonal direction to the welding line, in order to obtain cross sections. The cut has been performed with the Delta AbrasiMet bench-top cutter (Figure 4.8), with an abrasive disk of boron nitride.

Figure 4.8 – Delta AbrasiMet bench-top cutter

The cross sections obtained were embedded into cylindrical forms of a phenolic resin, by means of the hot pneumatic press EP15 (Figure 4.9). It was used a polymerization process at a constant pressure of 3.2 bar and a thermal cycle made up of a heating up to 175 °C, holding at this temperature for 7 minutes and a rapid cooling to 35°C.

Subsequently, the specimens were subjected to a process of grinding and polishing in order to minimize the surface roughness to be subjected to metallographic analysis. The polishing machine used is the PRESI Mecapol P320 (Figure 4.10a), equipped with a rotating disk with adjustable speed (from 50 rpm to 500 rpm, in a clockwise or counterclockwise) on which it is possible to fix abrasive papers or cloths (linen, cotton, etc..).

Figure 4.9 – Hot pneumatic press EP15

The specimens are mounted on a holder (Figure 4.10b), then put in rotation and pushed through a closing force on the main disk.

The lapping cycle is composed by the following phases:

- 600 GRIT (size grains of 18-22 μm) abrasive paper, for 10 minutes, with a closing force of 10 daN, at 300 rpm
- 1000 GRIT (size grains of 8-11 μm) abrasive paper, for 5 minutes, with a closing force of 10 daN, at 300 rpm
- Cloth with a diamond suspension of 6 μm, for 5 minutes, with a closing force of 7 daN, at 400 rpm

- Cloth with a diamond suspension of 3 μm, for 5 minutes, with a closing force of 7 daN, at 450 rpm
- Cloth with a diamond suspension of 1 μm, for 5 minutes, with a closing force of 7 daN, at 500 rpm
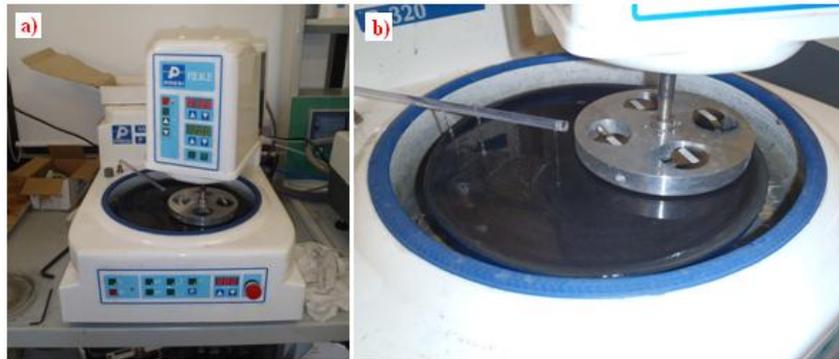
Figure 4.10 – Polishing machine PRESI Mecapol P320

At the end of the polishing process, the specimens were etched using a solution composed of:

- 10% HF (48%)
- 15% HNO_3 (65%)
- 75% of distilled H_2O

to highlight the geometric characteristics and microstructures of the beads.

During chemical etching of a metallic sample, oxidation-reduction reactions take place. All metals in contact with a solution have a tendency to ionize through the release of electrons. The development of this reaction can be evaluated by measuring the electrochemical potential and through the comparison of the metal potential with a reference electrode (electrode of hydrogen). Starting from these considerations, a table of the elements arranged in decreasing order of electron affinity can be built.

Li^+, Na^+, K^+, Ca^{2+}, Ba^{2+}, Be^{2+},Al^{3+}, Mn^{2+}, Zn^{2+}, Cr^{3+}, Cd^{2+}, Ti^+, Co^{2+}, Ni^{2+}, Pb^{2+}, Fe^{3+}, H^+, Sn^{4+}, Bi^{3+}, As^{3+}, Cu^{2+}, Ag^+, Hg^+, Au^{3+}, Pt^{3+}.

All the elements preceding hydrogen can be etched by acids with a development of hydrogen. While those positioned subsequently can not be attacked by acids except in the presence of an oxidizing agent. Therefore microstructural constituents of different electrochemical potential are etched by the acid at different speeds and this involves microstructural contrasts. In a chemical etching the acidic solution reacts with the surface of the sample through a selective dissolution according to the electrochemical potentials of the components constituting the surface itself.

The dissolution leads consequently to a removal of material especially in the areas of edge-grain which highlight the morphology of the crystalline grains and also their possible orientation.

The etching is performed by wetting the surface to be treated with the acid and leaving this to act for a period of time which varies depending on the material. Finally, the acid is removed from the surface with distilled water.

The reagent was left in contact with the joint for a few minutes, highlighting all three zones: the base material, meted zone and HAZ. The procedure was successful and satisfactory for subsequent observations.

At this point, the samples appear as shown in Figure 4.11 and can be analyzed by the optical microscope.
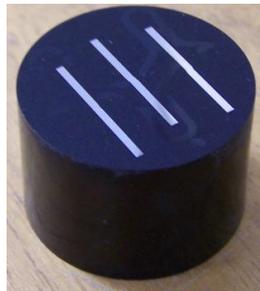
Figure 4.11 – Sample ready for the analysis

4.3.5 *Microhardness and tensile tests*

Hardness is the measure of how resistant solid matter is to various kinds of permanent shape change when a force is applied. Vickers microhardness tests were performed in order to evaluate this material

characteristic from the weld bead to the base metal. These tests are performed using a diamond indenter in the shape of a square based pyramid with vertex angle between two sides of 136 ° ± 0.5 ° (Figure 4.12) and nominally equal diagonals. The value of Vickers microhardness is determined by Equation 22:

$$HV = 0.1891 \cdot \frac{P}{d^2} \qquad (22)$$

where P represents the applied load in Newton and d the average of the two diagonals in mm.

   The minimum thickness of the specimen of which is to determine the microhardness shall not be less than 1.5 times the diagonal of the indentation and the indentation should be at a distance of at least 2.5 times the diagonal itself.
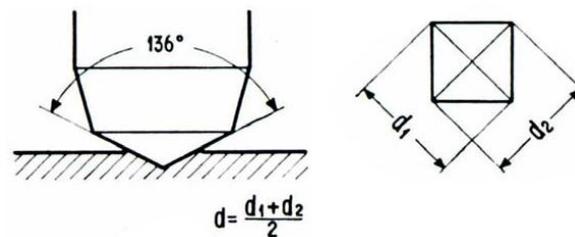
Figure 4.12 – Geometry of the diamond intender

   Vickers microhardness tests were performed, with a load of 300 gf and a duration of 15 s at 60 μm/s using a LeicaVM HTAUTO micro hardness tester (Figure 4.13).

Figure 4.13 – LeicaVM HTAUTO micro hardness tester

Tensile properties indicate how the material will react to forces being applied in tension. A tensile test is a fundamental mechanical test where a carefully prepared specimen is loaded in a very controlled manner while measuring the applied load and the elongation of the specimen over some distance. Tensile tests are used to determine the modulus of elasticity, elastic limit, elongation, proportional limit, reduction in area, tensile strength, yield point, yield strength and other tensile properties.

The main product of a tensile test is a load versus elongation curve which is then converted into a stress versus strain curve. Since both the engineering stress and the engineering strain are obtained by dividing the load and elongation by constant values (specimen geometry information), the load-elongation curve will have the same shape as the engineering stress-strain curve. The stress-strain curve relates the applied stress to the resulting strain and each material has its own unique stress-strain curve. A typical engineering stress-strain curve is shown in Figure 4.14. If the true stress, based on the actual cross-sectional area of the specimen, is used, it is found that the stress-strain curve increases continuously up to fracture.
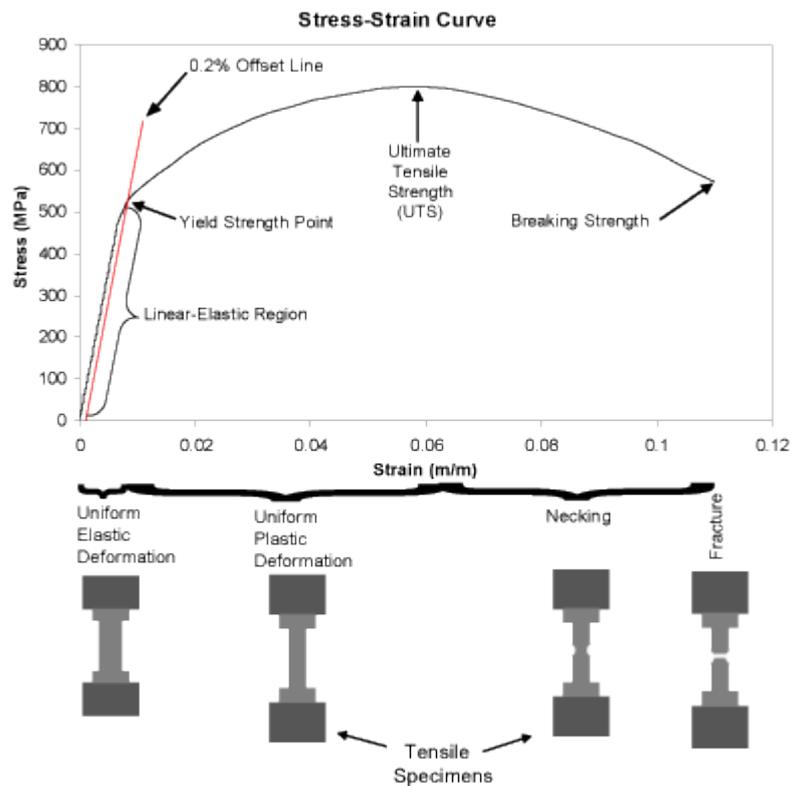
Figure 4.14 – Typical engineering stress-strain curve

As can be seen in the Figure 4.14, the stress and strain initially increase with a linear relationship. This is the linear-elastic portion of the curve and it indicates that no plastic deformation has occurred. In this region of the curve, when the stress is reduced, the material will return to its original shape. In this linear region, the line obeys the relationship defined as Hooke's Law where the ratio of stress to strain is a constant.

The slope of the line in this region where stress is proportional to strain and is called the modulus of elasticity or Young's modulus. The modulus of elasticity (E) defines the properties of a material as it undergoes stress, deforms, and then returns to its original shape after the stress is removed. It is a measure of the stiffness of a given material. To compute the modulus of elastic, simply it is necessary divide the stress by the strain in the material. Since strain is unitless, the modulus will have the same units as the stress, such MPa. The modulus of elasticity applies

specifically to the situation of a component being stretched with a tensile force. This modulus is of interest when it is necessary to compute how much a rod or wire stretches under a tensile load.

In ductile materials, at some point, the stress-strain curve deviates from the straight-line relationship and law no longer applies as the strain increases faster than the stress. From this point on in the tensile test, some permanent deformation occurs in the specimen and the material is said to react plastically to any further increase in load or stress. The material will not return to its original, unstressed condition when the load is removed. In brittle materials, little or no plastic deformation occurs and the material fractures near the end of the linear-elastic portion of the curve.

With most materials there is a gradual transition from elastic to plastic behavior, and the exact point at which plastic deformation begins to occur is hard to determine. Therefore, various criteria for the initiation of yielding are used depending on the sensitivity of the strain measurements and the intended use of the data. For most engineering design and specification applications, the yield strength is used. The yield strength is defined as the stress required to produce a small, amount of plastic deformation. The offset yield strength is the stress corresponding to the intersection of the stress-strain curve and a line parallel to the elastic part of the curve offset by a specified strain (in the US the offset is typically 0.2% for metals and 2% for plastics).

The ultimate tensile strength (UTS) or, more simply, the tensile strength, is the maximum engineering stress level reached in a tension test. The strength of a material is its ability to withstand external forces without breaking. In brittle materials, the UTS will at the end of the linear-elastic portion of the stress-strain curve or close to the elastic limit. In ductile materials, the UTS will be well outside of the elastic portion into the plastic portion of the stress-strain curve.

On the stress-strain curve above, the UTS is the highest point where the line is momentarily flat. Since the UTS is based on the engineering stress, it is often not the same as the breaking strength. In ductile materials strain hardening occurs and the stress will continue to increase until fracture occurs, but the engineering stress-strain curve may show a decline in the stress level before fracture occurs. This is the result of engineering stress being based on the original cross-section area and not accounting for the necking that commonly occurs in the test specimen. The UTS may not be completely representative of the highest level of

stress that a material can support, but the value is not typically used in the design of components anyway. For ductile metals the current design practice is to use the yield strength for sizing static components. However, since the UTS is easy to determine and quite reproducible, it is useful for the purposes of specifying a material and for quality control purposes. On the other hand, for brittle materials the design of a component may be based on the tensile strength of the material.

The ductility of a material is a measure of the extent to which a material will deform before fracture. The conventional measures of ductility are the engineering strain at fracture (usually called the elongation) and the reduction of area at fracture. Both of these properties are obtained by fitting the specimen back together after fracture and measuring the change in length and cross-sectional area. Elongation is the change in axial length divided by the original length of the specimen or portion of the specimen. It is expressed as a percentage. Because an appreciable fraction of the plastic deformation will be concentrated in the necked region of the tensile specimen, the value of elongation will depend on the gage length over which the measurement is taken. The smaller the gage length the greater the large localized strain in the necked region will factor into the calculation. Therefore, when reporting values of elongation , the gage length should be given.

Tensile tests were performed on 3 mm butt welds using a Schenk 630N machine operating with a load rate of 250 N/s at room temperature.

The specimens were designed according to the UNI EN 895: 1997 standard with the following characteristics (Figure 4.15):

- Thickness of the test specimens: 3mm
- Width of the calibrated parallel length: 25 mm
- Original gauge length: 100 mm
- Parallel length: 120 mm
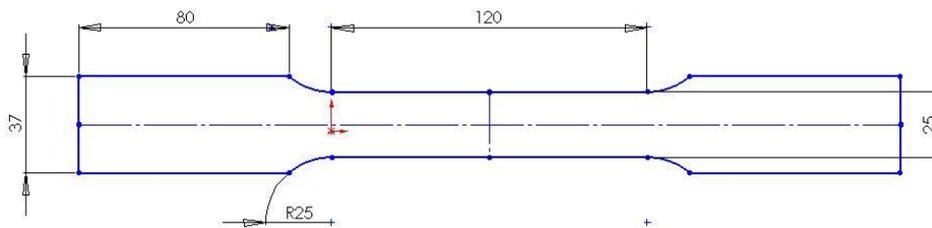
Figure 4.15 – Scheme of the tensile test specimen

4.4 Experimental plans

The experimental work is composed of three different experimental designs. Ti6Al4V plates of two different thickness were taken into consideration: 3 and 1 mm.

With regard to 3 mm, after the bead on plate tests, butt welds were carried out varying only power and welding speed focusing the beam on the upper surface of the plates. The joint that has the best characteristics is selected and subjected to tensile test.

Subsequently, in order to evaluate the effect of defocusing, a couple of parameters were selected (power-welding speed) of the previous. Then the bead on plate tests were carried out using 9 different focus positions.

With regard to 1 mm sheets, a fractional factorial design was carried out in order to evaluated the effects of power, welding speed and focus position on butt welds by response surface method. Using the ANOVA analysis, geometric characteristics, defects and hardness regression models were obtained. These equations were then used in order to satisfy some optimization criteria to get triples of parameters to obtain good quality joints.

4.4.1 Butt welding on 3 mm thickness sheets

Before making butt welds, bead on plate tests were carried out to determine the window parameters of power and welding speed to be used for butt welds. Both bead on plate tests and butt welding tests were performed on Ti6Al4V plates with dimensions of 50x50x3 mm. The decision was made to focus the beam on the upper surface of the plates to

obtain maximum power density values and a spot diameter of 0.3 mm. Good results in terms of penetration depth were obtained with powers between 1500 W and 2000 W and welding speeds between 15 mm/s and 25 mm/s. For this reason, the butt welds were carried out using a full factorial plan with two factors and three levels, as shown in the Table 4.3 which also reports the heat input (power/welding speed). Each test was randomly repeated three times for a total of 27 experimental tests.

Table 4.3 – Butt welding parameters for 3 mm thick sheets

Laser power [W]	Welding speed [mm/s]	Heat input [J/mm]
1500	15	100
1500	20	75
1500	25	60
1750	15	117
1750	20	88
1750	25	70
2000	15	133
2000	20	100
2000	25	80

4.4.2   Bead on plate tests on 3 mm thickness sheets

Bead on plate tests were performed on Ti6Al4V plates with dimensions of 50x50x3 mm. An experimental plan was conducted using nine focus positions with constant power and welding speed to evaluate the effect of defocusing on geometry, defects, hardness and microstructure of the beads. The focus positions chosen were in the range from -4 mm to +4 mm respect to the upper surface of the beads. A power of 2000 W and a welding speed of 20 mm/s were selected. This power value could ensure the key-hole formation also with a defocusing of 4 mm because a density power of 9354 W/mm^2 near the conduction-keyhole threshold (10^4 W/mm^2) was obtained. The welding speed selected was a good compromise between heat input (100 J/mm) and bead quality. Table 4.4 shows the experimental plan composed of nine experimental conditions repeated three times in a random order for a total of 27 tests.

Table 4.4 – Bead on plate defocusing values for 3 mm thick sheets

Focus position [mm]	Power density [W/mm^2]
-4	9354
-3	13230
-2	18790
-1	25126
0	28309
1	25126
2	18790
3	13230
4	9354

4.4.3 Butt welding on 1 mm thickness sheets

With regard to the 1 mm plates, an experimental design with input factors power, welding speed and focus position was made.

Preliminary bead on plate tests were carried out to decide the level values of these parameters to be considered in the experimental plan. These preliminary tests are necessary for several reasons because in addition to giving indications on complete penetration of the weld, they have allowed the assessment of possible macro-defects and to verify the effectiveness of the shielding and clamping system (Figure 4.16) because the latter is much more critical for a 1 mm compared to a 3 mm thicknees.
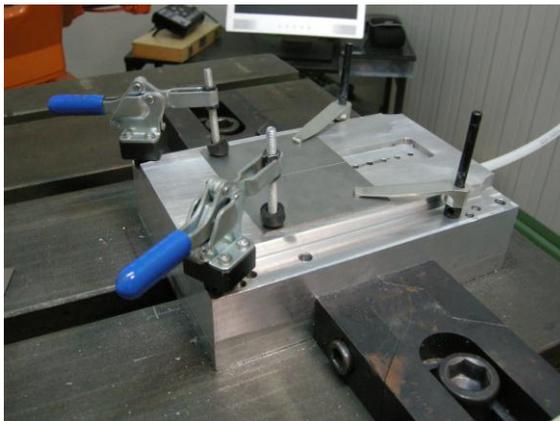
Figure 4.16 – Clamping system

The first step was to set the defocusing values. It has been chosen:

- focusing the beam to the upper surface of the bead, in order to obtain the higher power density achievable
- a symmetrical range
- integer values of defocusing.

Since the regression models provide the best results in terms of predictability within the considered ranges, the farther values from 0 mm defocusing were chosen, which ensure, however, the key-hole formation. So ±2 mm defocusing was selected. In fact, by choosing values outside this range, for example ± 3 mm, considering maximum output power of the laser used, a too narrow range of power would have to be considered in order to have a power density greater than 10^4 W/mm^2 (threshold value from conduction to key-hole for titanium).

To obtain a power density greater than 10^4 W/mm^2, the chosen power values vary between 1400 W and 1800 W. In fact, with defocusing and power values chosen, a key-hole welding should take place.

In regards to the speed range, values that cause a thermal input such as to ensure full penetration of the weld were selected. From literature, using a Nd:YAG laser, with a heat input value of 14.3 J/mm, there was no full penetration. Condition instead achieved with a value of 16.7 J/mm.

These results have been useful to acquire information about the speed values to be used to obtain with the power values chosen a heat input value such as to ensure full penetration. Bead on plate tests were carried out, using a power of 1400 W and a speed of 110 mm/s, causing a heat input of 12.7 J/mm. But as shown in Figure 4.17, full penetration was not obtained.

Figure 4.17 – BoP at 1400 W, 110 mm/s and -2 mm

In order to obtain a greater heat input and penetration depth, a bead on plate test with a welding speed of 100 mm/s was carried out. In this case, a heat input of 14 J/mm, a greater penetration depth even if not continuous (Figure 4.18), was obtained.
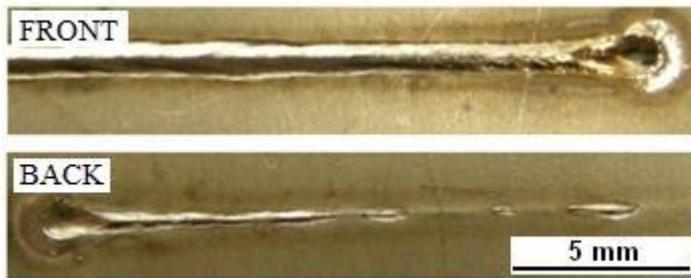
Figure 4.18 – BoP at 1400 W, 100 mm/s and -2 mm

But since in a butt weld a greater penetration than that obtainable with a bead on plate test occurs, a butt weld with a speed of 100 mm/s and with a power of 1400 W was made. As expected, full penetration is obtained as shown in Figure 4.19. The above tests were carried out with a power of 1400 W because this is the worst condition in terms of penetration depth being the minimum power value.
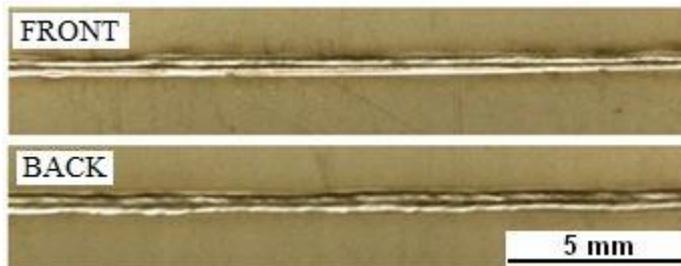
Figure 4.19 – Butt test at 1400 W, 100 mm/s and -2 mm

In Table 4.5 the values of the chosen parameters are reported. In Tables 4.6 and 4.7, the values of power density and thermal input obtained are respectively shown.

Table 4.5 – Butt welding parameters for 1 mm thick sheets

	Minimum	**Intermediate**	**Maximum**
P [W]	1400	1600	1800
S [mm/s]	60	80	100
F [mm]	-2	0	+2

Table 4.6 – Power density values obtained for 1 mm

		Power [W]		
	Power density [W/mm^2]	1400	1600	1800
Focus position [mm]	-2	13163	15043	16923
	0	19806	22635	25465
	2	13163	15043	16923

Table 4.7 – Heat input values obtained for 1 mm

		Power [W]		
	Heat input [J/mm]	1400	1600	1800
Speed [mm/s]	60	23.3	26.7	30.0
	80	17.5	20.0	22.5
	100	14.0	16.0	18.0

A full factorial design with three factors and three levels would be made of 3^3=27 experimental conditions. In addition, usually 3 or more repetitions of each experimental condition are performed in order to remove random errors effects. Since achieving an experimental plan of 3x27=81 tests would be too expensive, it was decided to use a fractional factorial plan. An experimental plan suited to perform an optimization of the output variables by response surface methodology was chosen.

A rotatable plan ensures that the variance of the expected response is the same at all points that have the same distance from the center of the plan. Thus the variance of the expected response remains unchanged when the plane is rotated around the center, hence the name rotatable

plan. A plan that provides the same accuracy of estimation in all directions was selected because the optimum location is a priori unknown.

The most used fractional designs to obtain models of the second order are the central composite design (CCD) and Box-Behnken design.

The CCD consists of three groups of points:

- n_F points of a 2^k factorial plan (plan with k factors at two levels)
- axial points (also called "star points", points on the red axes in Figure 4.20)
- n_c central points

Two important parameters of the plan are: axial distance α from the plan center and the central points number.
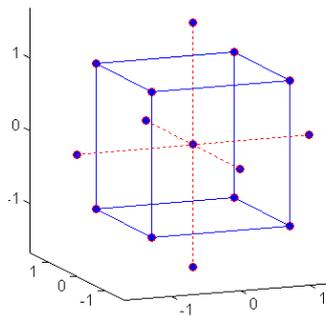
Figure 4.20 – Central composite design for k=3

A CCD is made rotatable by the α value selected: in fact, a value of α = $(n_F)^{1/4}$ produces a rotatable CCD. Figure 4.20 shows the CCD for k = 3. Such a plan consists of tests at points with power, speed and defocusing values different from those previously selected by bead on plate tests. For this reason a CCD plan was not chosen. To overcome this problem, a face-centered CCD (a variant of the CCD in which α=1) could be used (Figure 4.21).
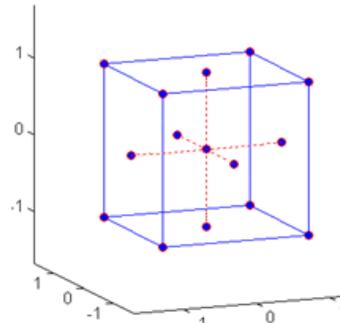
Figure 4.21 – Face-centered CCD for k=3

With such a plan, previously established parameter ranges would be respected. But this plan would not be rotatable. For this reason, even this other option was rejected.

Box and Behnken have proposed three-levels plans for response surface methodology. These designs (Figure 4.22), used to describe non-linear responses, are usually very efficient with respect to the number of tests required, and are either rotatable or nearly rotatable.
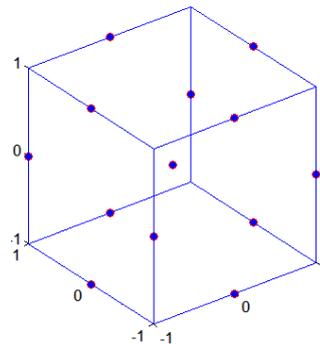
Figure 4.22 – Box-Behnken design

As shown in Figure 4.22, the Box-Behnken design contains all the points that are on a sphere of radius $\sqrt{2}$ and therefore does not show points to the vertices of the cubic region identified by the lower and upper limits of each variable. For all these reasons, a Box-Behnken design was chosen with three replications of the central point to provide a more uniform estimate of the variance of the expected response.

In Table 4.8, Box-Behnken experimental design obtained by Design-Expert 8.0.6 software is reported.

Table 4.8 – Box-Behnken experimental plan for 1 mm thick sheets

RUN	P [W]	S [mm/s]	F [mm]	RUN	P [W]	S [mm/s]	F [mm]
1	1800	80	-2	24	1600	80	0
2	1600	80	0	25	1800	80	-2
3	1400	60	0	26	1800	100	0
4	1400	100	0	27	1600	100	2
5	1800	60	0	28	1600	80	0
6	1400	80	2	29	1600	60	-2
7	1800	80	2	30	1400	80	-2
8	1800	100	0	31	1600	80	0
9	1600	80	0	32	1600	100	2
10	1800	60	0	33	1600	100	-2
11	1600	60	-2	34	1400	80	2
12	1400	80	2	35	1600	100	-2
13	1600	80	0	36	1400	100	0
14	1400	80	-2	37	1600	60	2
15	1400	60	0	38	1400	100	0
16	1400	60	0	39	1600	60	-2
17	1800	80	2	40	1600	100	2
18	1600	80	0	41	1800	100	0
19	1400	80	-2	42	1600	100	-2
20	1600	60	2	43	1800	80	2
21	1800	60	0	44	1600	80	0
22	1800	80	-2	45	1600	80	0
23	1600	60	2				

As previously mentioned, each experimental condition is repeated three times, for a total of 45 tests. In Table 4.9, the same experimental conditions tests are grouped in the same item, in terms of actual and coded factors.

Table 4.9 – Experimental conditions in terms of actual and coded factors

ITEM	P	S	F
A	1400	60	0
B	1600	100	-2
C	1600	80	0
D	1600	80	0
E	1800	80	2
F	1400	80	2
G	1400	80	-2
H	1600	100	2
I	1800	100	0
L	1600	80	0
M	1800	60	0
N	1400	100	0
O	1600	60	-2
P	1800	80	-2
Q	1600	60	2

ITEM	P	S	F
A	-1	-1	0
B	0	1	-1
C	0	0	0
D	0	0	0
E	1	0	1
F	-1	0	1
G	-1	0	-1
H	0	1	1
I	1	1	0
L	0	0	0
M	1	-1	0
N	-1	1	0
O	0	-1	-1
P	1	0	-1
Q	0	-1	1

Chapter 5

Analysis and optimization

5.1 Power and welding speed effects on 3 mm thickness

5.1.1 Joint morphology

As shown from the cross sections in Tables 5.1, 5.2 and 5.3, fully penetrated welds were obtained except for the conditions of 1500 W and 25 mm/s, which showed a non-uniform full penetration.

Table 5.1 – Butt welding cross sections at 1500 W
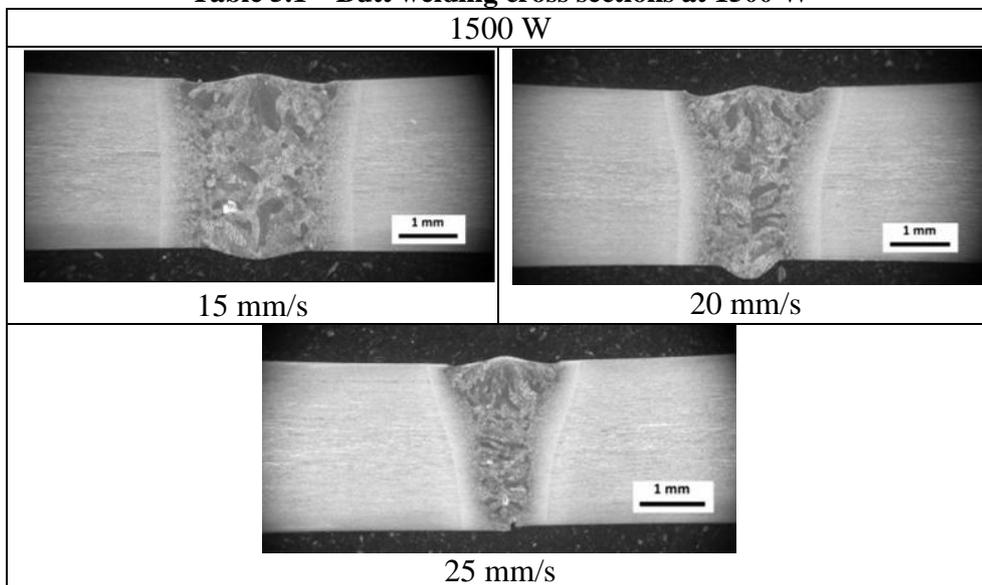
Table 5.2 – Butt welding cross sections at 1750 W

1750 W

15 mm/s

20 mm/s

25 mm/s
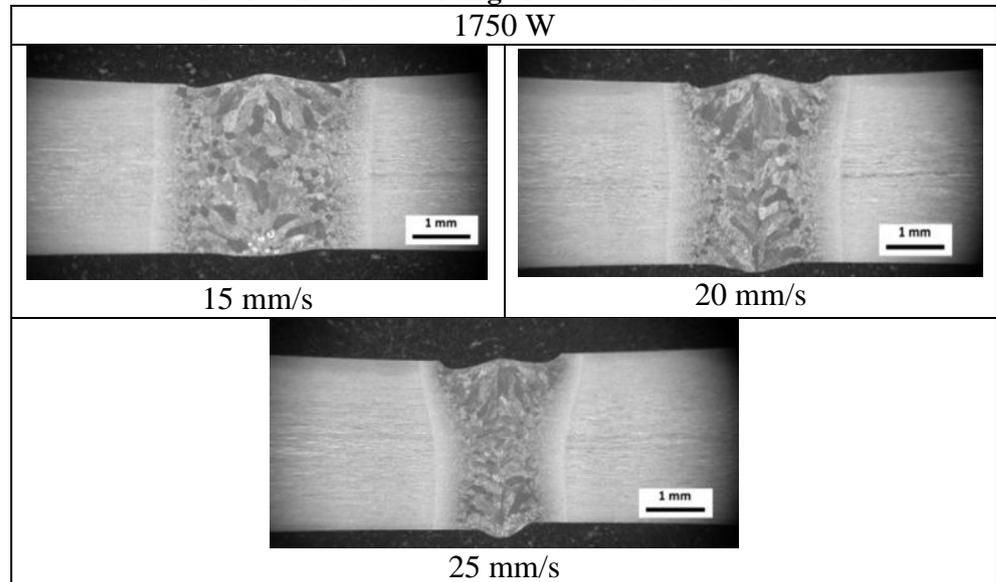
Table 5.3 – Butt welding cross sections at 2000 W

2000 W

15 mm/s

20 mm/s

25 mm/s
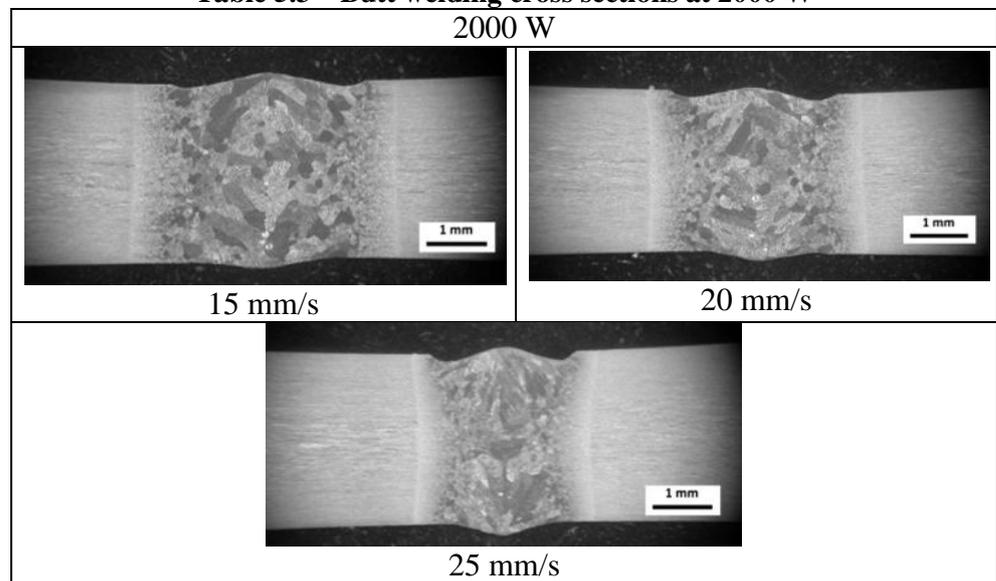
The joint morphology was evaluated by measuring the geometric features shown in Figure 5.1: width upper (Wu), width lower (Wl), heat affected zone upper (HAZu), heat affected zone lower (HAZl) and melted area (MA).
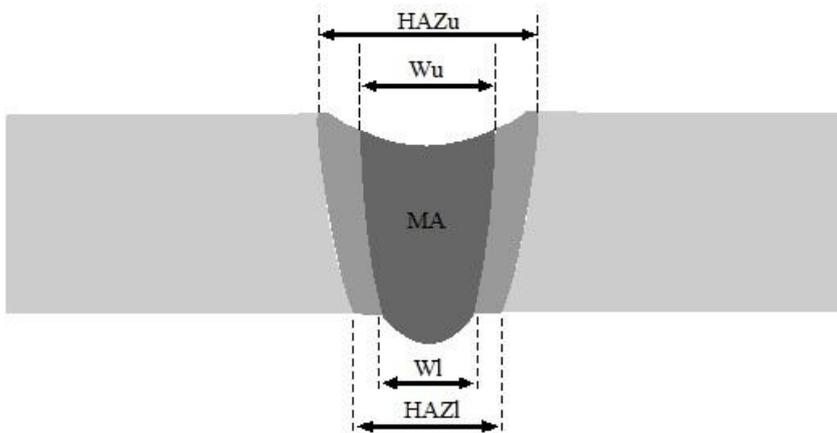
Figure 5.1 – Geometric features measured

Table 5.4 shows the mean of the geometric features for each experimental condition.

Table 5.4 – Geometric features values

P [W]	S [mm/s]	Q [J/mm]	Wu [mm]	Wl [mm]	HAZu [mm]	HAZl [mm]	MA [mm^2]
1500	15	100	3.28	2.78	3.68	3.46	8.43
1500	20	75	2.74	1.84	3.04	2.41	5.54
1500	25	60	2.44	0.48	2.76	1.61	4.20
1750	15	117	3.39	3.02	3.87	3.74	9.35
1750	20	88	2.92	2.32	3.19	2.98	7.02
1750	25	70	2.70	2.12	3.04	2.65	6.63
2000	15	133	4.04	3.95	4.61	4.56	11.86
2000	20	100	3.31	3.00	3.70	3.56	8.88
2000	25	80	2.95	2.53	3.28	2.96	7.37

The measured geometric features increase with increasing power and decrease with increasing welding speed as shown in Figures 5.2, 5.3, 5.4 and 5.5. These two conditions resulted in an increase in the heat input,

which varied from 60 J/mm to 133 J/mm. For the same values of heat input, geometrical features were similar. A lower heat input allowed for smaller melted and heat affected areas. Therefore, better quality beads were obtained with heat input values ranging from 60 J/mm to 80 J/mm. At 60 J/mm, uniform, full penetration was not assured. Furthermore, the bead shape changed from cylindrical to conical with increasing welding speed, as shown from the cross-sections and from Wu and Wl values.

The heat affected zones were very narrow and assumed a minimum and maximum value respectively of 2.76 mm and 4.61 mm on the upper surface, instead a minimum and maximum value respectively of 1.61 mm and 0.56 mm on the lower surface
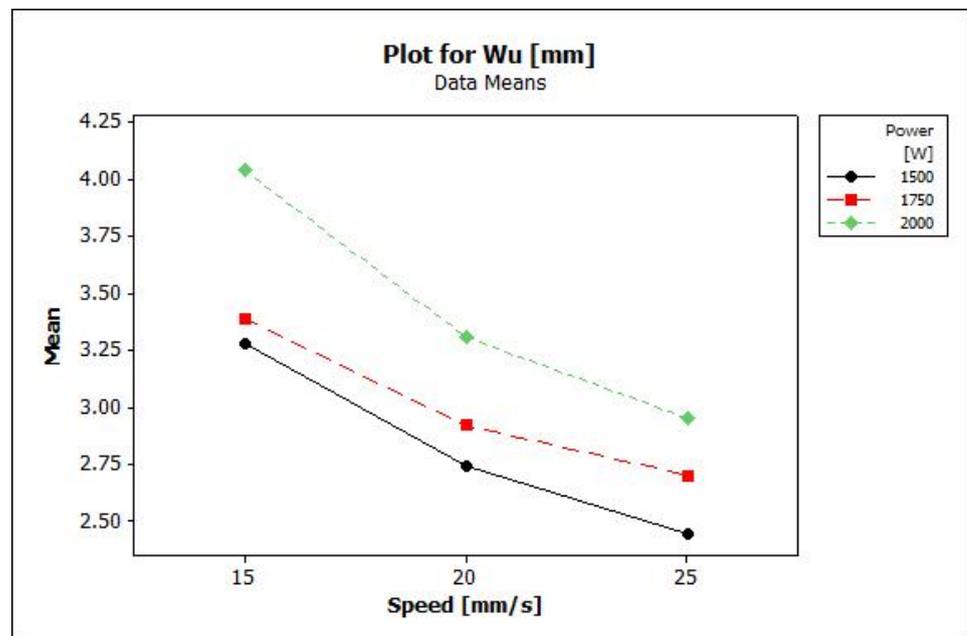
Figure 5.2 – Wu vs Speed for all Power values
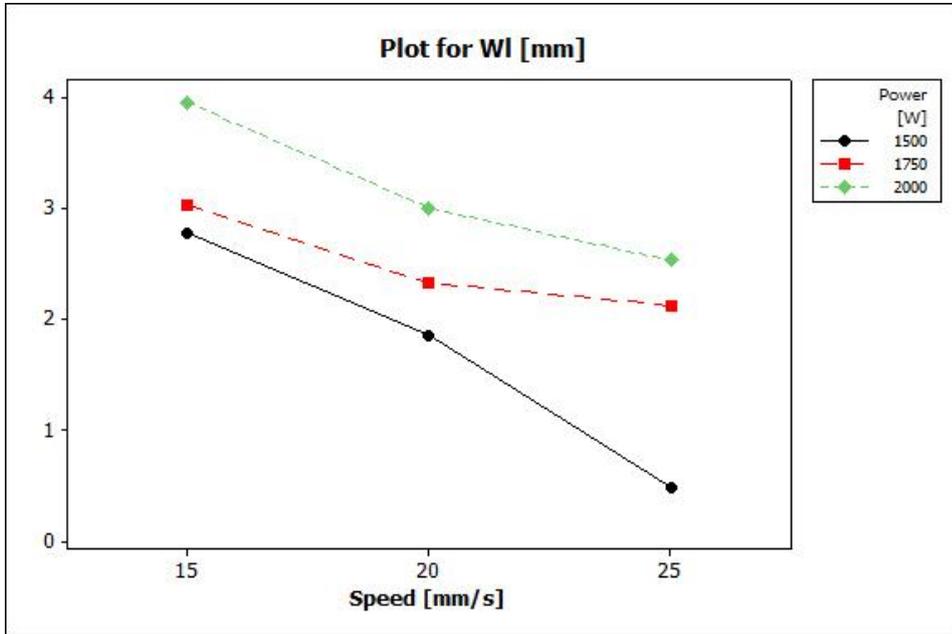
Figure 5.3 – Wl vs Speed for all Power values
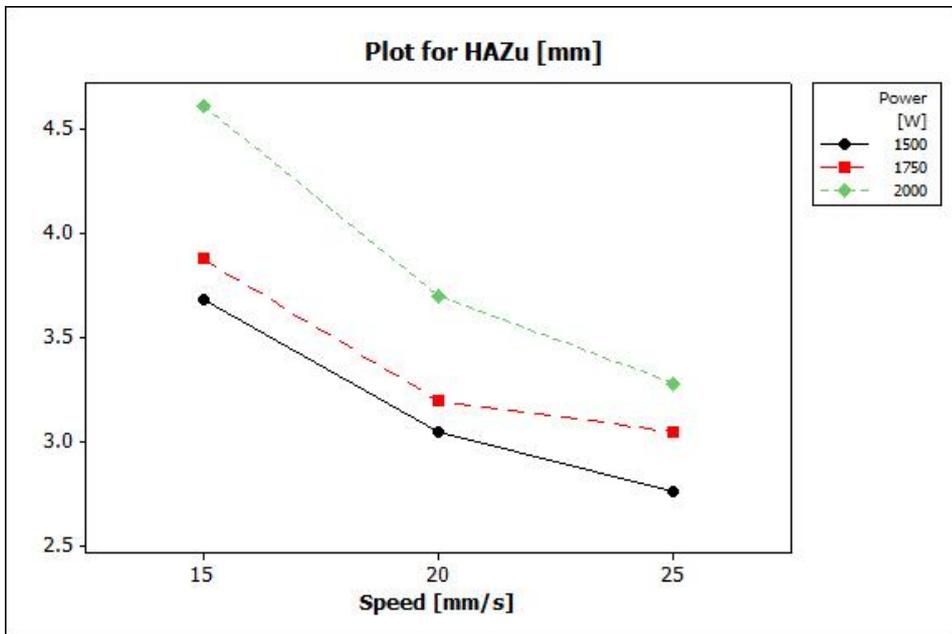
Figure 5.4 – HAZu vs Speed for all Power values
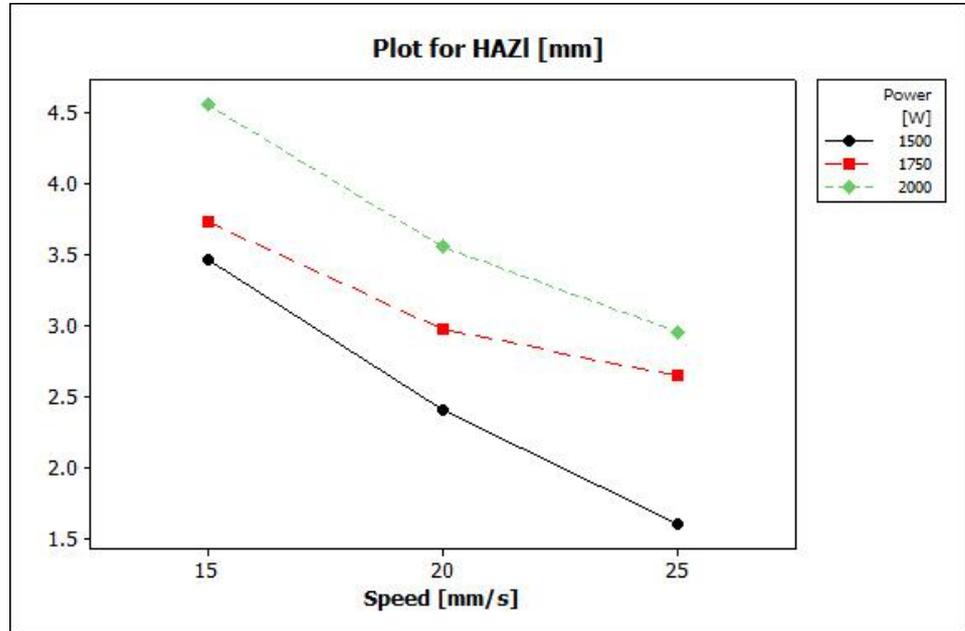
Figure 5.5 – HAZl vs Speed for all Power values
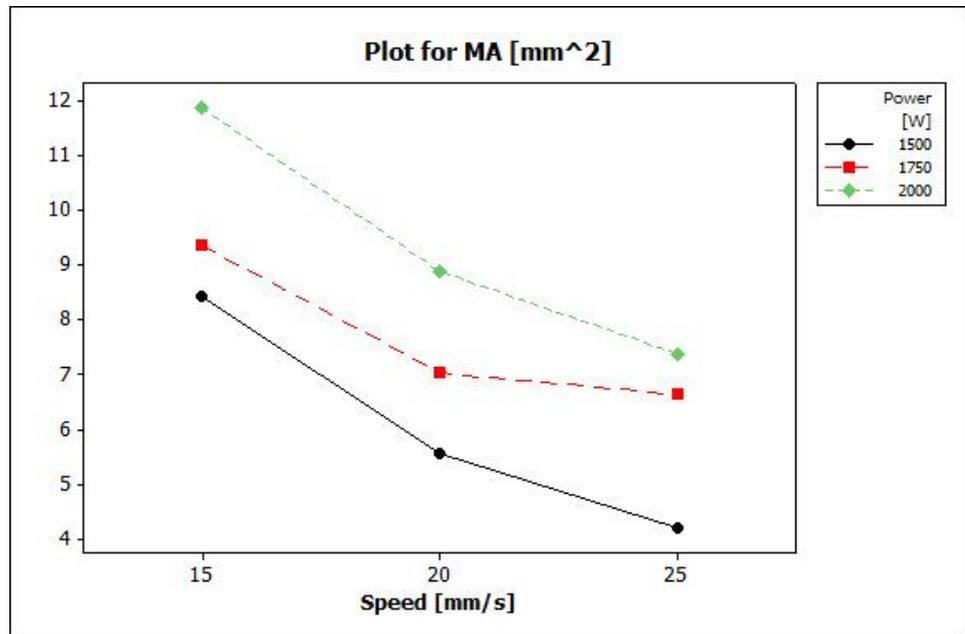
Figure 5.6 – MA vs Speed for all Power values

From the main effects plots it is possible to observe that welding speed has a greater influence on the upper characteristics (Figures 5.7, 5.8, 5.9, 5.10, 5.11) compared to the power. But, moving from top to the bottom surface, this behavior is lost and the lower characteristics are influenced in the same way by power and welding speed.
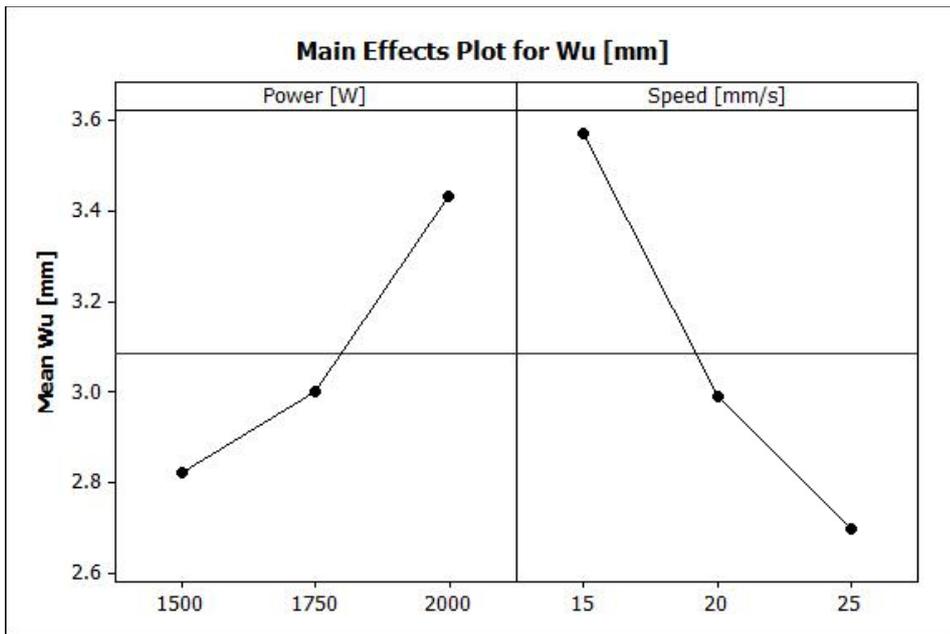
Figure 5.7 – Main effects plot for Wu of 3 mm thick sheets
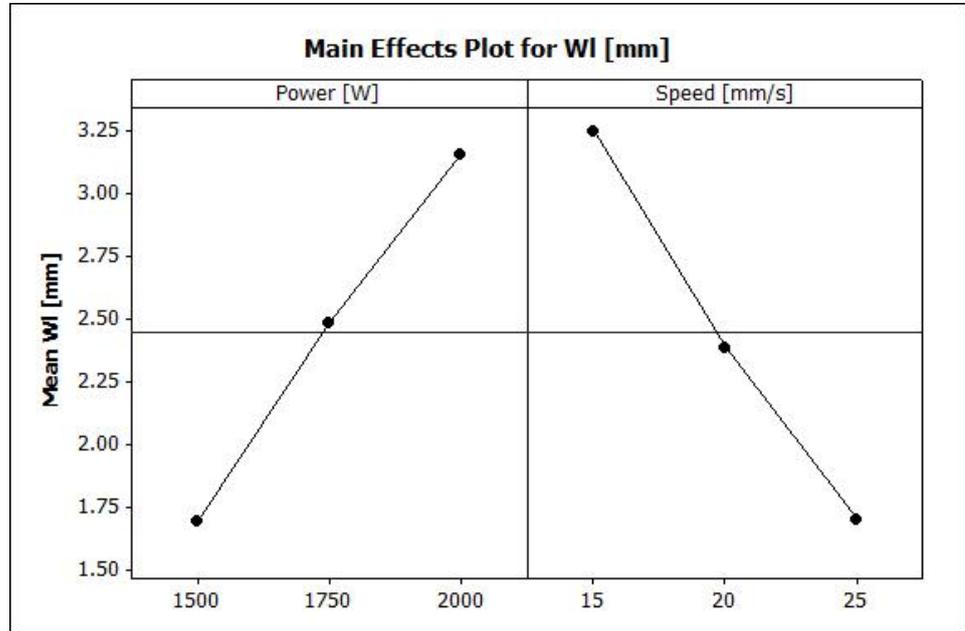
Figure 5.8 – Main effects plot for Wl of 3 mm thick sheets
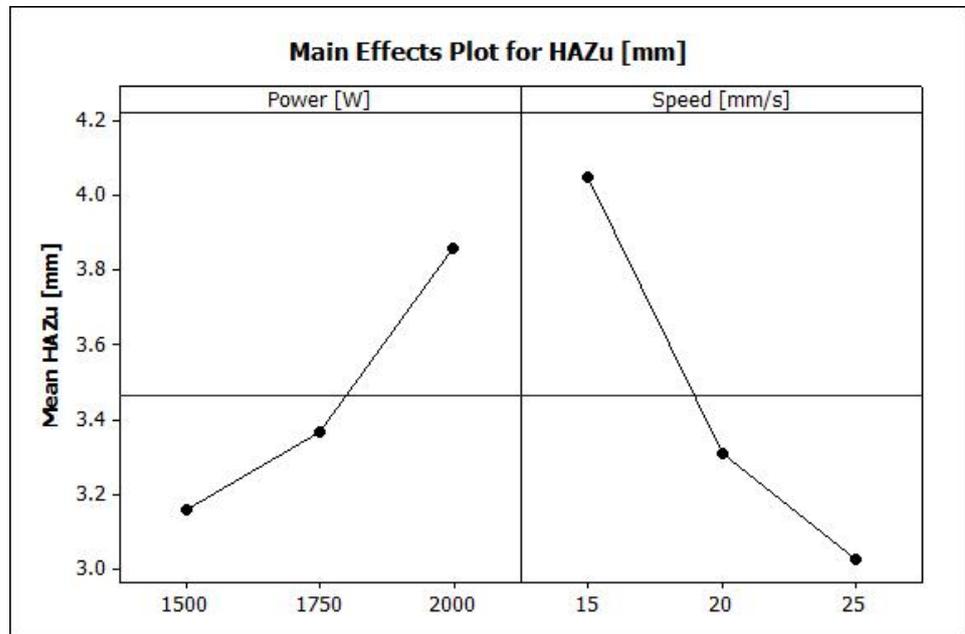
Figure 5.9 – Main effects plot for HAZu of 3 mm thick sheets
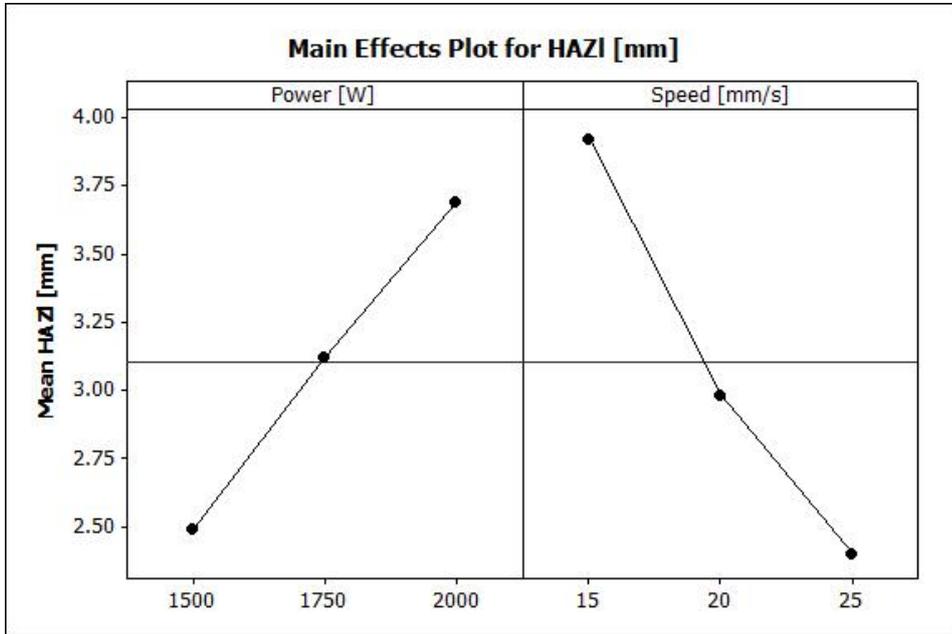
Figure 5.10 – Main effects plot for HAZl of 3 mm thick sheets
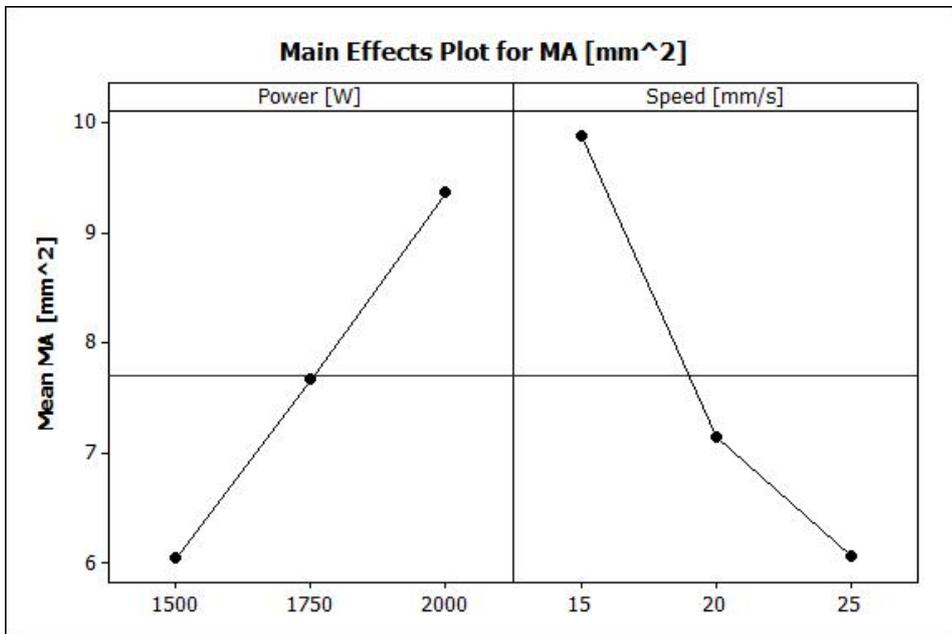
Figure 5.11 – Main effects plot for MA of 3 mm thick sheets

5.1.2 *Defects*

Geometrical defects (Figure 5.12) such as undercut, excess weld metal, excessive penetration and misalignment were measured for all 27 beads.
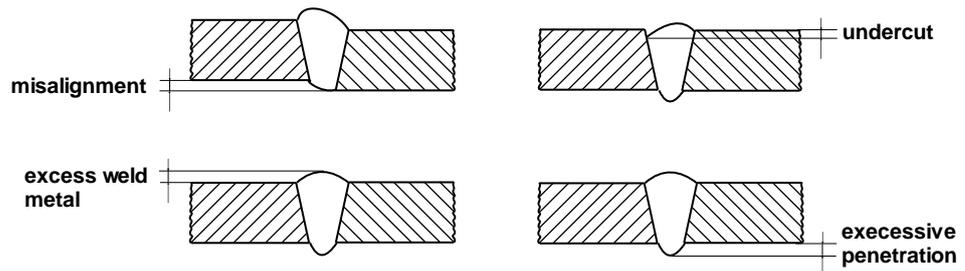
Figure 5.12 – Geometric defects measured

Undercuts are two small depressions that extend in the welding direction, positioned on either side of the bead near the solid-melted interface. In general, these defects reduce the weld thickness and work as a stress concentrators, reducing the tensile strength and fatigue life. These defects increase with increasing both power and welding speed. In fact, at high power there is severe material evaporation. Instead, when welding is performed very quickly, the fluid dynamics of the melt causes a depression that remains in the bead.

Table 5.5 – Geometric defects values for 3 mm thick sheets

P [W]	S [mm/s]	Q [J/mm]	EP [mm]	EWM [mm]	Udx [mm]	Usx [mm]	MIS [mm]
1500	15	100	0.09	0.13	0.07	0.08	0.08
1500	20	75	0.21	0.08	0.10	0.10	0.11
1500	25	60		0.07	0.05	0.05	0.04
1750	15	117	0.01	0.15	0.09	0.08	0.08
1750	20	88	0.06	0.11	0.10	0.09	0.12
1750	25	70	0.13	0.07	0.13	0.12	0.08
2000	15	133	0.04	0.15	0.10	0.08	0.09
2000	20	100	0.13	0.13	0.12	0.12	0.06
2000	25	80	0.17	0.10	0.15	0.15	0.05

In Table 5.5 defects values to vary the input factor are reported. The undercuts increase with increasing power and welding speed but, when a lack of penetration occurred, the undercuts are very small, as the cross-section at 1500 W and 25 mm/s shows.

The excess weld metal increases with increasing power and with decreasing welding speed. Instead the excessive penetration and the misalignment don't show clear trend to vary power and welding speed.

However, all values defects are in accordance the quality stringent level limits imposed by the UNI EN ISO 13919 1:1997 standard:

- undercuts ≤ 0.15 mm
- excess weld metal ≤ 0.65 mm
- excessive penetration ≤ 0.65 mm
- linear misalignment ≤ 0.3 mm

Another typical defect in weld joints is porosity. Porosity usually decreases the weld cross-section and thus the strength of the joint, especially when the pores are large in size and number. Cross-sectional analysis showed that porosity was mainly distributed in the root of the melted area (Figure 5.13). This is probably due to more rapid cooling and solidification, which impedes the escape of bubbles. Because porosity is located in the root area and in the excessive penetration material, it does not seem to affect the tensile strength of the joints as will be shown later. The spherical shape of the pores is typically caused by hydrogen absorption in the molten pool.
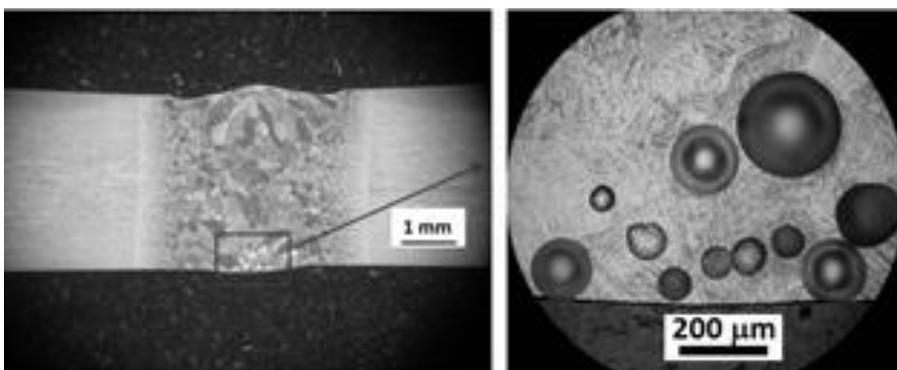
Figure 5.13 – Porosity location for a specimen welded at 1750 W and 15 mm/s

Because it is not sufficient to evaluate the presence of porosity simply through examination of the cross-sections, X-ray examinations were performed on a series of nine samples. As shown in Figure 5.14 , X-ray analysis showed an increase in porosity by a reduction in the speed, probably due to the increased time available for the bubbles to grow. However, the porosity content did not show a clear tendency to vary with power.

(a)

(b)
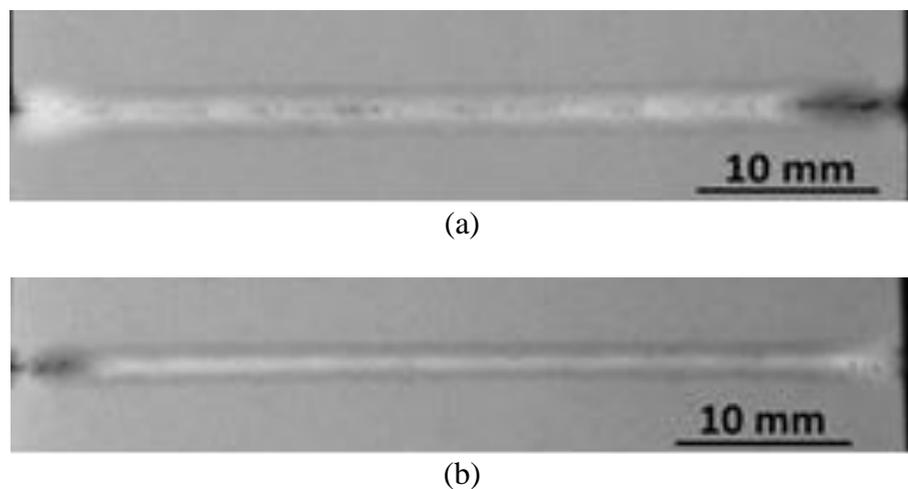
Figure 5.14 – X-ray photograph of specimens at 1750 W 15 mm/s (a) and 25 mm/s (b)

5.1.3 Microstructure

Figure 5.15 shows the typical microstructure of a weld bead. The base material (BM) has a typical structure for α+β titanium alloy, composed of the dark β phase in a dominant, bright α matrix. The β phase is distributed at the boundaries of the elongated α grains.
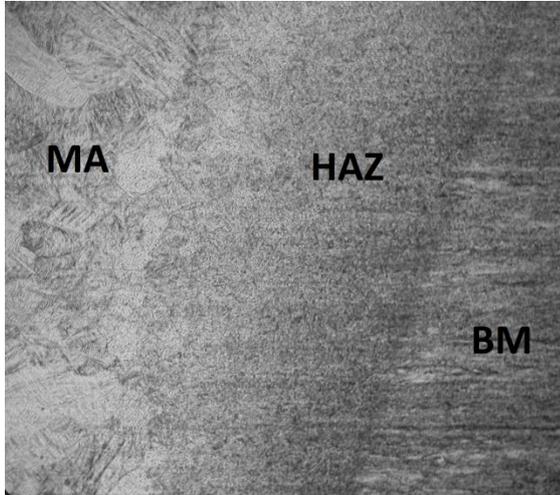
Figure 5.15 – Microstructure of the melted area, HAZ and base material

The melted area consisted mainly of acicular α' martensite, a similar structure quenched from the β phase region above the β transus.

Cooling rates higher than 410 °C/s are usually required for Ti6Al4V alloy to attain a completely martensitic microstructure. The high self-quenched rate associated with the laser-beam welding process certainly promotes the diffusionless transformation of the β phase into a martensitic microstructure.

The heat affected zone is a mixture of α' and primary α phases, which corresponds to a structure quenched below the β transus ranging from 720 to 985 °C. Near the melted zone, some α' phase could be observed whereas farther away from the MA a relative increase of primary α was observed, mainly due to lower cooling rate.
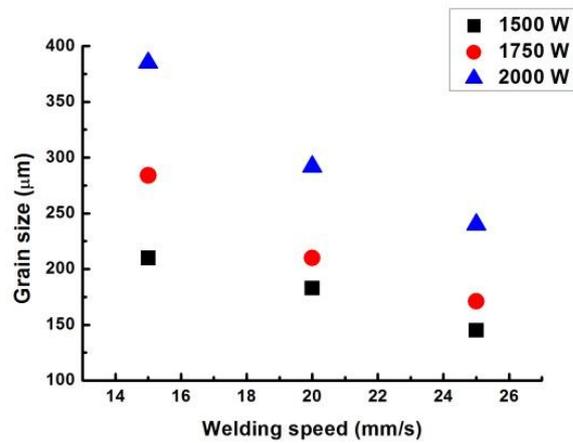
Figure 5.16 – Grain size vs. welding speed

In the melted area, the size of the grains increased with increasing heat input during welding and decreased with increasing welding speed, as shown in Figure 5.16 . When the power increases, the grains have more time to grow, which is also the case when using a low welding speed.

Figure 5.17 shows the microstructures of specimens welded at 1500 W-25 mm/s and at 2000 W-15 mm/s.

(a)   (b)
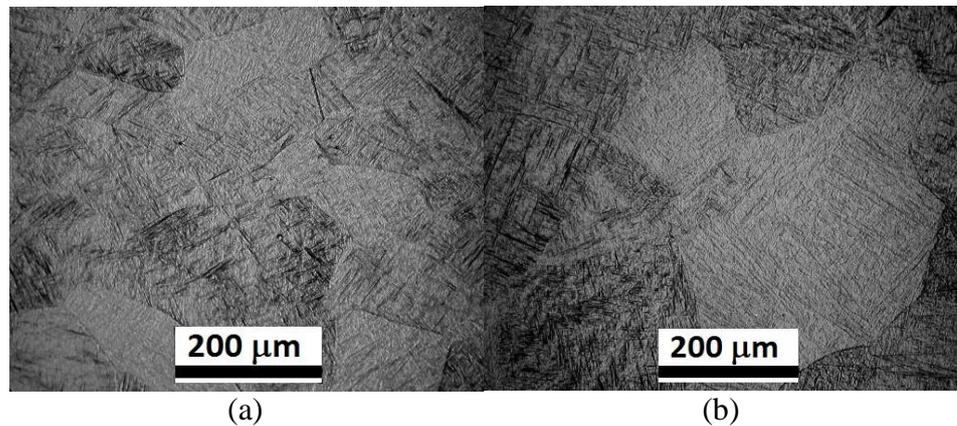
Figure 5.17 – Figure 8 : Microstructures of specimens welded at 1500 W-25 mm/s (a) and at 2000 W-15 mm/s (b)

5.1.4 Mechanical characterization

Vickers microhardness tests were performed 1.5 mm below the upper surface of the joints with the application of a load of 300 gf. The hardness assumed an average value of 354 HV in the base metal and increased in the melted zone with an average value that varied from 389 HV to 418 HV. An increase in the welding speed increased the average hardness in the melted area probably due to rapid cooling rate. There was not a clear tendency of hardness to vary with the power. The maximum hardness in the melted area was due to the presence of α' martensite that gradually decreased from the fusion boundary and disappeared at the HAZ-base material interface. Figure 5.18 shows the microhardness distribution for a specimen at 1500 W and 15 mm/s
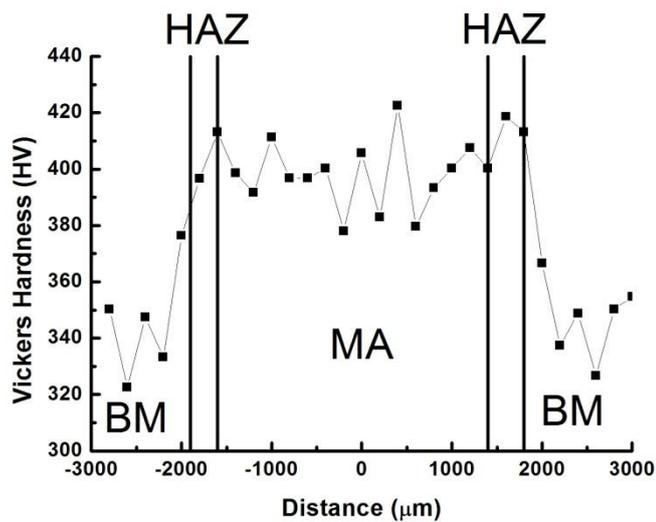
Figure 5.18 – Hardness distribution profile of a specimen welded at 1500 W-15 mm/s

Then, after the weld joint analysis, the specimens with weld parameters of 1750 W and 25 mm/s were selected for tensile test because the corresponding joints had good geometric characteristics due to low heat input, less porosity content and satisfactory geometric defects.

All three samples exhibited a fragile fracture mode, typical of Ti6Al4V Grade 5, with moderate elongation, limited shrinkage of cross-

sectional area and a fracture path inclined by 45° with respect to the loading direction.
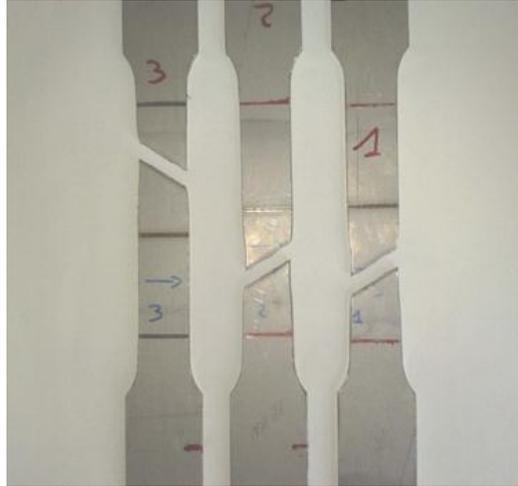
Figure 5.19 – Welded specimens after tensile tests

All three welded specimens showed a break in the original gauge length away from the beads, as shown in Figure 5.19.

The ultimate tensile stress was 1149 MPa, the yield stress was 950 MPa, and the elongation at fracture varied between 8-9% (Figure 5.20).
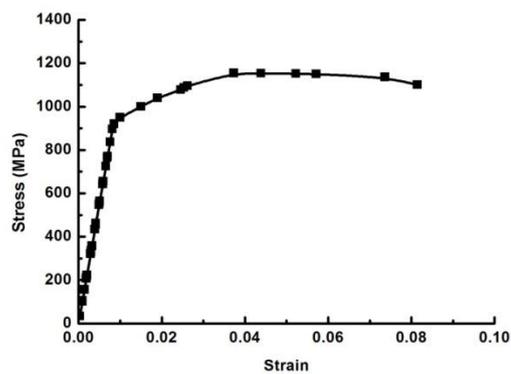
Figure 5.20 – Example of a stress-strain diagram

5.2   Defocusing effect on 3 mm thickness

5.2.1   Bead morphology

The bead morphology was evaluated by measuring the following geometric features shown: width upper, width lower, heat affected zone upper, heat affected zone lower and melted area. Fully penetrated welds were obtained except for the conditions of 4 mm defocused respect to the upper surface, which showed a non-uniform full penetration as shown from the cross-sections in Table 5.6.

Table 5.6 – Bead on plate cross-sections at different focus positions

-1 mm	-2 mm	-3 mm	-4 mm

0 mm			

+1 mm	+2 mm	+3 mm	+4 mm

The bead shape changed from cylindrical to conical with increasing defocusing. For defocusing values from -1 to +1 mm, the size of the bead were similar and showed a cylindrical geometry (similar values of Wu, Wl) due to a small power density variation on the upper surface of the piece. Whereas, for defocusing values from -2 to -4 mm and from +2 mm to +4 mm, the bead geometry became conical with increasing defocusing because a great difference between Wu and Wl was found (Figure 5.21).

This is due to the reduction of power density which was not sufficient to melt the same material width on the upper and lower surfaces of the workpiece.
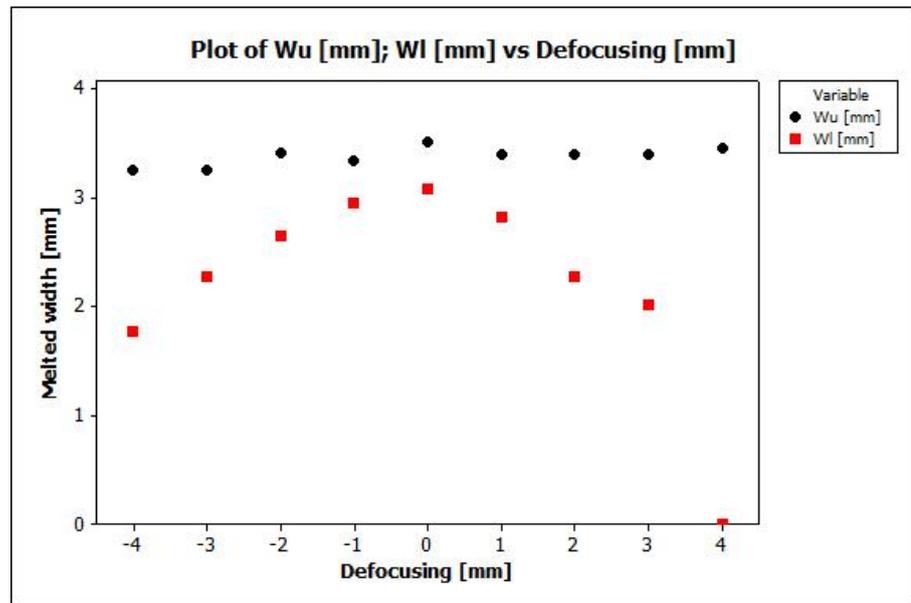
Figure 5.21 – Wu and Wl vs defocusing

The penetration depth was much more affected by the divergent beam shape outside the Rayleigh length; defocusing of -4 mm full penetration was obtained because of convergent beam shape. The MA was maximum with 0 mm defocusing and decreased to the minimum values with ±4 mm defocusing due to lower power density as shown in Figure 5.22.
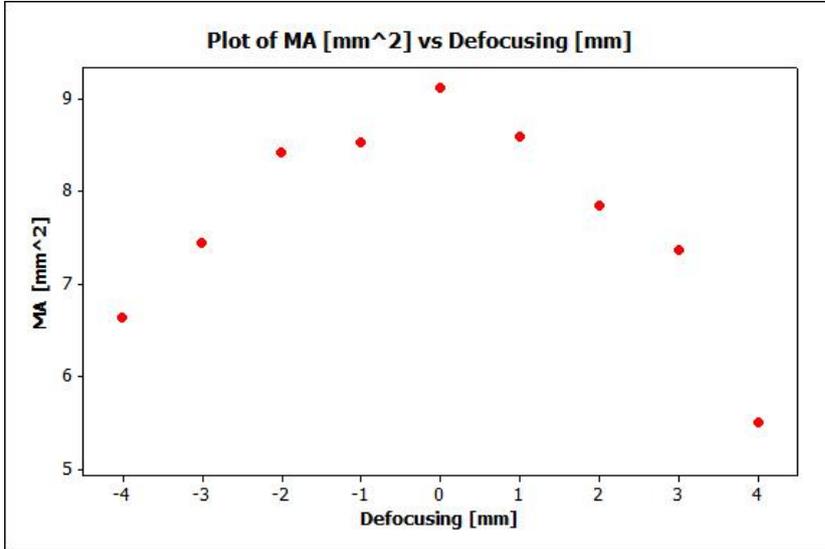
Figure 5.22 – MA vs defocusing

The difference between the heat affected zones and the melted widths were very small for all defocusing values but didn't show clear trends.

In Table 5.7 all the measured geometric characteristics are reported.

Table 5.7 – Geometric features values for BoP tests

F [mm]	Wu [mm]	Wl [mm]	HAZu [mm]	HAZl [mm]	MA [mm^2]
-4	3.245	1.775	3.495	2.05	6.64
-3	3.255	2.275	3.6	2.62	7.435
-2	3.405	2.645	3.74	3.065	8.41
-1	3.34	2.945	3.67	3.475	8.52
0	3.515	3.085	3.825	3.495	9.115
1	3.395	2.82	3.76	3.2	8.59
2	3.4	2.275	3.71	2.695	7.845
3	3.39	2.02	3.73	2.305	7.355
4	3.45		3.69	1.185	5.505

5.2.2 Defects

Geometrical defects (Figure 5.23) such as undercut, excess weld metal, excessive penetration were measured for all 27 beads.
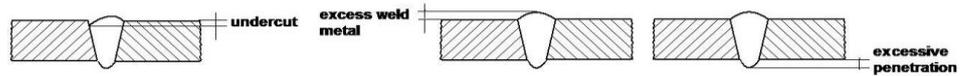
Figure 5.23 – Geometrical defects measured for BoP tests

Table 5.8 shows that undercuts decreased with defocusing, due to lower material evaporation because of lower power density; the undercut values ranged from 0.03 mm to 0.12 mm respectively with defocusing of -4 mm and 0 mm.

The excess weld metal did not show a clear tendency with varying focal position and ranged from 0.09 mm to 0.17 mm.

Table 5.8 – Geometrical defects values for BoP tests

F [mm]	EP [mm]	EWM [mm]	Usx [mm]	Udx [mm]
-4	0.190	0.145	0.035	0.030
-3	0.325	0.085	0.085	0.085
-2	0.315	0.095	0.085	0.095
-1	0.295	0.170	0.105	0.100
0	0.240	0.115	0.110	0.120
1	0.230	0.145	0.075	0.055
2	0.220	0.150	0.075	0.080
3	0.130	0.160	0.040	0.055
4	0.005	0.110	0.070	0.060

Excessive penetration increased from 0.13 mm to 0.33 mm respectively with defocusing of +3 mm and -3 mm and decreased to 0.19 mm with -4 mm defocusing. This trend (Figure 5.24) occurred because, focusing from +3 mm to 0 mm, the increase in power density on the upper surface of the piece was obtained. Instead, defocusing from 0 mm to -3 mm, since key-hole welding mode occurred, the maximum power density is within the piece causing an increase in excess of penetration. Whereas,

defocusing to -4 mm, the focus is located outside the piece, producing a lower excess penetration.
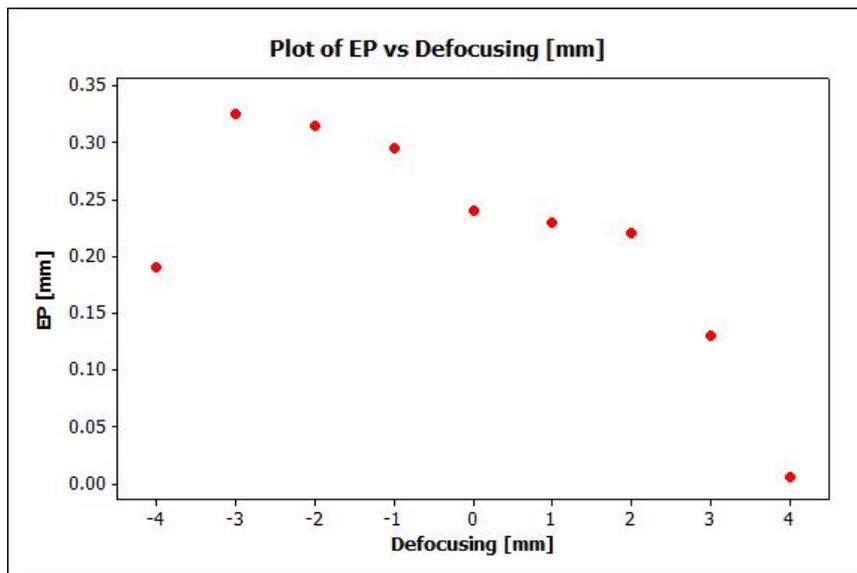
Figure 5.24 – EP vs Defocusing

Also in this case, values defects are in accordance the quality stringent level limits imposed by the UNI EN ISO 13919 1:1997 standard

5.2.3 *Microstructure and hardness*

In the melted area, a significant variation in grain size between 0 mm and -4 mm defocusing was found, whose average size was of 290 μm (Figure 5.25a) and 90 μm (Figure 5.25b) respectively. This variation is much more apparent with defocusing positions out of the Rayleigh length due to lower power density and consequent higher cooling rate.

<div align="center">(a)   (b)</div>
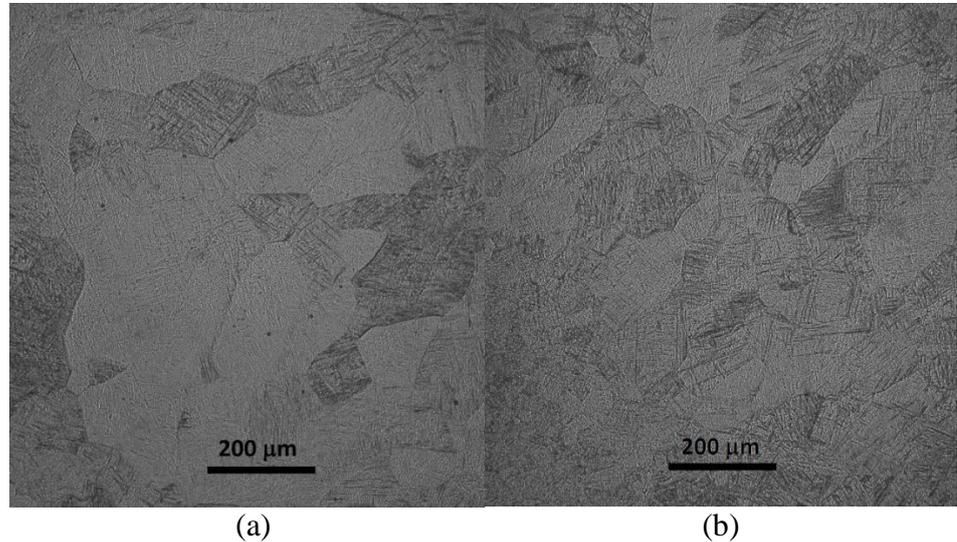
Figure 5.25 – Microstructures of specimens welded at 0 mm (a) and -4 mm (b) focus position

Vickers microhardness tests were performed 1.5 mm below the upper surface of the beads. The hardness assumed an average value of 356 HV 0.5/30 in the base metal and increased in the melted zone with an average value that varied from 371 HV 0.5/30 to 397 HV 0.5/30.

The maximum hardness in the melted area was due to the presence of α' martensite that gradually decreased from the fusion boundary and disappeared at the HAZ-base material interface.

An increase of average hardness in the melted zone with increasing defocusing it was observed, as Figure 5.26 shows. This is due to the reduction in the average size of grains in the melted zone.
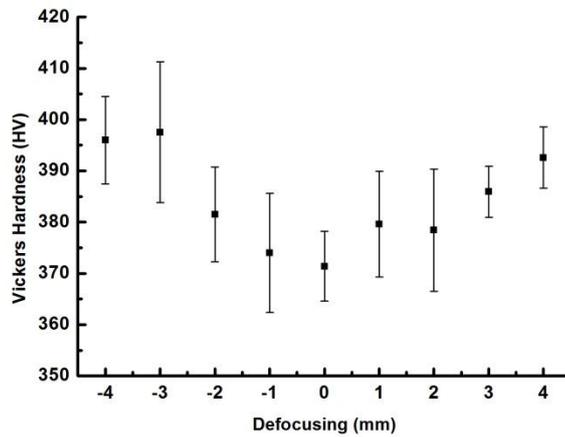
Figure 5.26 – Hardness values in the melted area for all focus position

5.3 Analysis of thin sheets butt welding

5.3.1 Geometric features

The melted zone geometric characteristics measured are: width upper, width lower, and melted area. In Figure 5.27 only one cross-section for each triple of parameters is reported. Fully penetrated joints were obtained.
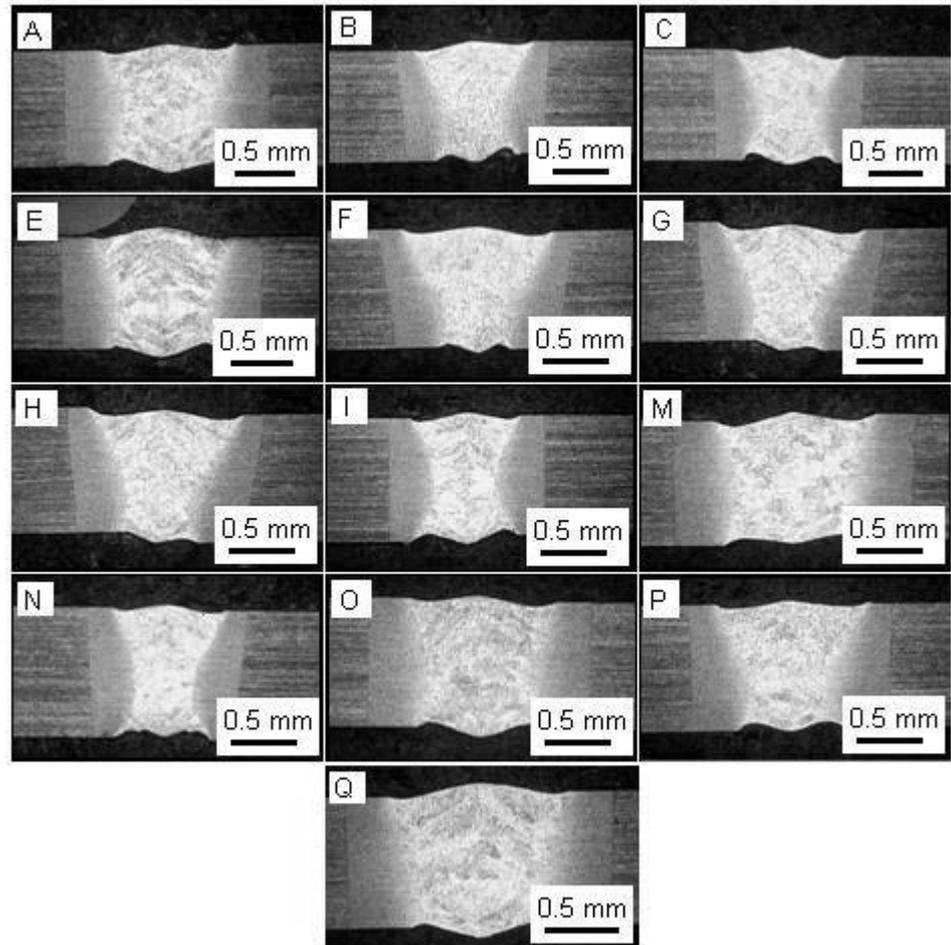
Figure 5.27 – 1 mm butt welding cross sections

Welding speed and defocusing were proven to be the factors that most influenced the Wu (Figure 5.28). The Wu increased with increasing power, but not as much as it increased with decreasing welding speed. Increasing the interaction time between laser beam and material increased the width of the base metal being melted. Moreover, from 0 mm to ±2 mm defocusing, there was an increase in Wu. This effect might be due to the increase in spot area on the upper joint surface causing an increase of the melted width. The Wl (Figure 5.29) showed a trend similar to Wu one to vary in power and welding speed, but it didn't seem to be influenced by defocusing. When moving from the top to the bottom joint surface, a

reduction of the focus position effect was observed. At last, the amount of melted area (Figure 5.30) increased with power and decreased with welding speed as the three widths, while an intermediate trend between Wu and Wl is shown.
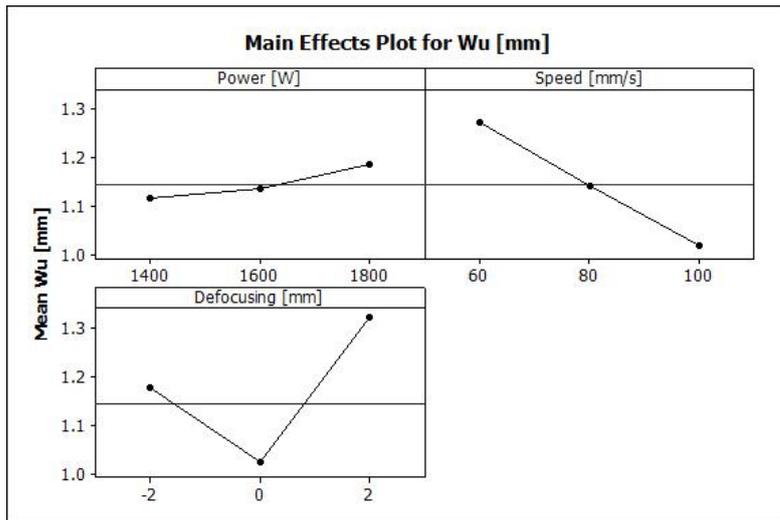
Figure 5.28 – Main effects plot for Wu of 1 mm thick sheets
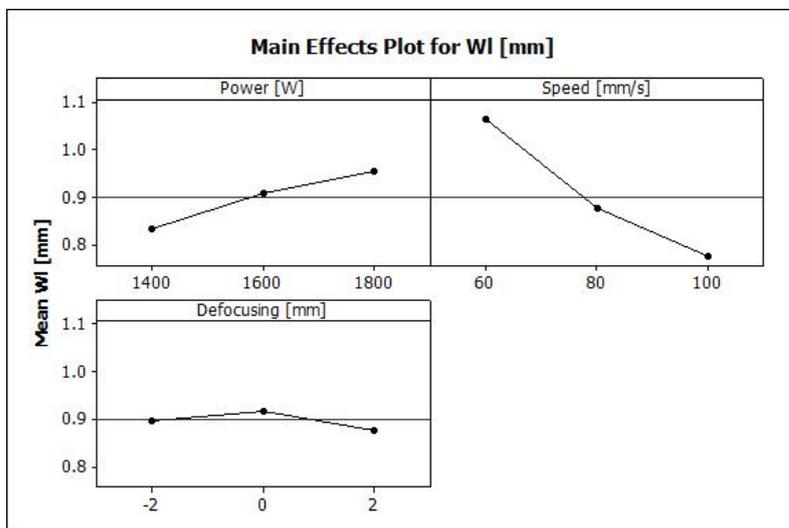
Figure 5.29 – Main effects plot for Wl of 1 mm thick sheets
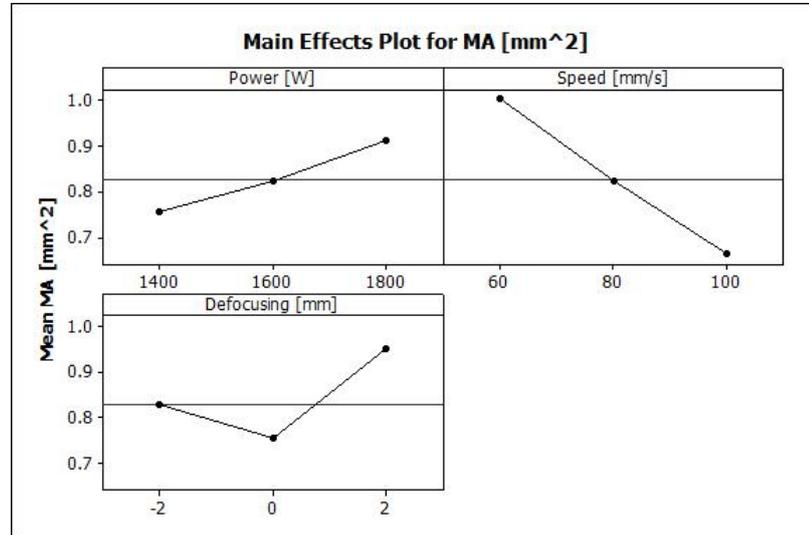
Figure 5.30 – Main effects plot for MA of 1 mm thick sheets

In Table 5.9 are reported the mean values of all measured geometric characteristics.

Table 5.9 – Geometric features values for 1 mm thick sheets

ID	P [W]	S [mm/s]	F [mm]	Wu [mm]	Wl [mm]	MA [mm^2]
A	1400	60	0	1.18	1.05	0.90
B	1600	100	-2	1.05	0.8	0.67
C	1600	80	0	1.01	0.91	0.76
D	1600	80	0	0.99	0.92	0.73
E	1800	80	2	1.33	0.98	1.09
F	1400	80	2	1.30	0.75	0.81
G	1400	80	-2	1.13	0.8	0.76
H	1600	100	2	1.27	0.73	0.77
I	1800	100	0	0.90	0.84	0.66
L	1600	80	0	0.98	0.87	0.70
M	1800	60	0	1.25	1.09	0.99
N	1400	100	0	0.86	0.73	0.55
O	1600	60	-2	1.27	1.07	0.98
P	1800	80	-2	1.26	0.91	0.91
Q	1600	60	2	1.39	1.05	1.14

5.3.2 Defects and Hardness

Geometric defects such as undercuts (upper undercut and lower undercut), excess weld metal, excessive penetration and misalignment were measured for all 45 beads and the mean values for each experimental conditions are reported in Table 5.10.

Table 5.10 – Geometric defects values for 1 mm thick sheets

ID	EWM [mm]	EP [mm]	MIS [mm]	Uu [mm]	Ul [mm]
A	0.030	0.035	0.05	0.027	0.047
B	0.030	0.020	0.08	0.033	0.060
C	0.035	0.040	0.08	0.037	0.048
D	0.040	0.040	0.04	0.028	0.056
E	0.040	0.040	0.08	0.030	0.021
F	0.030	0.035	0.07	0.042	0.031
G	0.040	0.030	0.06	0.031	0.068
H	0.020	0.040	0.10	0.047	0.030
I	0.040	0.035	0.05	0.029	0.036
L	0.035	0.040	0.11	0.033	0.047
M	0.035	0.030	0.08	0.062	0.035
N	0.025	0.025	0.08	0.034	0.049
O	0.040	0.040	0.10	0.027	0.055
P	0.040	0.040	0.04	0.038	0.040
Q	0.035	0.040	0.08	0.038	0.015

For 1 mm thickness, the quality stringent level limits imposed by the UNI EN ISO 13919 1:1997 standard become:

- undercuts ≤ 0.05 mm
- excess weld metal ≤ 0.35 mm
- excessive penetration ≤ 0.35 mm
- linear misalignment ≤ 0.1 mm

All defects values are lower than these limits, except for the undercut that assumes values higher than 0.05 for B, G, M conditions. However these undercut values are in accordance with the quality intermediate

level limits that is 0.1 mm. In this case all defects are not correlated with the input factors.

Vickers microhardness tests were performed 0.5 mm below the upper surface of the joints with the application of a load of 300 gf. Three indentations were made on the melted zone of one sample for each experimental conditions. In Table 5.11 the mean diagonal (dm), the hardness values (HV) and the hardness mean values (HVm) are reported:

Table 5.11 – Melted zone hardness value for 1 mm thick sheets

ID	P [W]	S [mm/s)	F [mm]	Dm [mm]	HV	HVm
A	1400	60	0	0.03825	386.02	
				0.03906	366.31	374.56
				0.03934	371.52	
B	1600	100	-2	0.03767	396.03	
				0.03805	384.22	395.68
				0.03723	406.42	
C	1600	80	0	0.03830	379.04	
				0.03854	374.62	370.68
				0.03943	357.25	
D	1600	80	0	0.03756	394.35	
				0.03906	364.12	375.45
				0.03889	367.61	
E	1800	80	2	0.03666	413.78	
				0.03741	397.47	390.25
				0.03927	360.39	
F	1400	80	2	0.03688	408.67	
				0.03741	397.56	395.65
				0.03822	380.46	
G	1400	80	-2	0.03644	418.65	
				0.03741	397.89	404.68
				0.03743	396.76	
H	1600	100	2	0.03674	411.56	
				0.03741	397.21	398.35
				0.03791	386.55	
I	1800	100	0	0.03772	390.78	
				0.03844	376.67	373.45
				0.03964	353.05	

				0.03748	395.66	
L	1600	80	0	0.03859	373.32	375.65
				0.03937	358.89	
				0.03831	378.54	
M	1800	60	0	0.03967	353.07	355.76
				0.04075	334.45	
				0.03676	411.35	
N	1400	100	0	0.03859	373.76	395.36
				0.03720	401.56	
				0.03726	400.24	
O	1600	60	-2	0.03912	363.65	382.36
				0.03801	384.55	
				0.03667	413.58	
P	1800	80	-2	0.03794	386.23	388.23
				0.03904	364.88	
				0.03664	414.21	
Q	1600	60	2	0.03813	382.44	386.78
				0.03915	362.68	

Figure 5.31 shows the main effect plot of main hardness in the melted zone with varying the input factors. An increase in the welding speed increased the average hardness in the melted area as well as a decrease in the power due to less heat input. Moreover, an increase of average hardness in the melted zone with increasing defocusing it was observed due to the reduction in the average size of grains in the melted zone because due to less irradiance values.
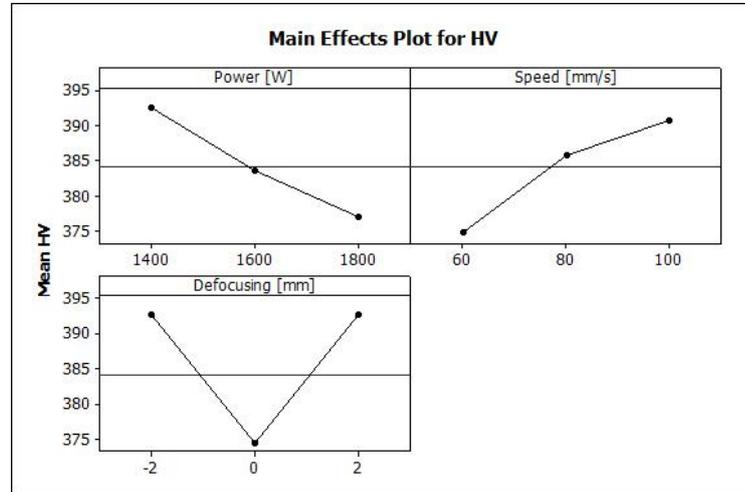
Figure 5.31 – Main effects plot for HV of 1 mm thick sheets

5.4   Modeling and optimization

5.4.1 ANOVA analysis and regression models

Regression equations were used to define the relationships between the responses and the input process factors. The response function can be written as:

$$Y = f(x_1, x_2, \dots, x_k) + \varepsilon \tag{23}$$

where Y is the observed value of a response variable, x1, x2,…, xk the levels of k factors and ε the noise or error terms in observing the response.

The quadratic model contains the linear terms, interactions and square terms:

$$Y = b_0 + \sum_{i=1}^{n} b_i x_i + \sum_{i=1}^{n} b_{ii} x_{ii}^2 + \sum_{i=1}^{n} \sum_{\substack{j=1 \\ j \neq i}}^{n} b_{ij} x_i x_j + \varepsilon \tag{24}$$

The ANOVA analysis and the development of regression equations were carried out for Wu, Wl, MA and HV. As input factors power, welding speed and defocusing have been chosen.

The test for significance of the regression models, the F-test for significance on individual model coefficients and the lack-of-fit test were all performed using the same statistical package. Then, the step-wise regression method was used to eliminate the not significant model terms automatically starting from a quadratic models. So, the resulting ANOVA Tables 5.12-5.15 for the models summarize the analysis of variance of each response and show the significant model terms. These tables also show the other adequacy measures R^2, adjusted R^2 and predicted R^2. They are all not so close to 1, but however they indicate adequate models. In fact, there is adequate precision in the comparison of the range of the predicted value at the design points to the average prediction error, and all its values are much greater than 4, the desirable ratio.

Table 5.12 – ANOVA table for Wu

Source	Sum of Squares	df	Mean Square	F Value	p-value Prob > F	
Model	0.37	4	0.092	35.34	< 0.0001	significant
P	9.112E-003	1	9.112E-003	3.49	0.0912	
S	0.13	1	0.13	48.86	< 0.0001	
F	0.042	1	0.042	16.11	0.0025	
F^2	0.19	1	0.19	72.88	< 0.0001	
Residual	0.026	10	2.610E-003			
Lack of Fit	0.026	8	3.204E-003	13.73	0.0696	not significant
Pure Error	4.667E-004	2	2.333E-004			
Cor Total	0.39	14				

R^2=0.9339   Adj R^2=0.9075
Pred R^2=0.8374Adeq precision=19.817

Table 5.12 shows that for Wu the main effect of the power, welding speed, defocusing and the second order effect of defocusing were the

most significant model terms. The high significance of F^2 was due to the importance of the irradiance, while the not perfect symmetry with defocusing, shown by the main effects plot, was justified by linear term F. The model F-value of 35.34, implied the model was significant. There is only a 0.01% chance that a "Model F-Value" this large could occur due to noise. Values of "Prob > F" less than 0.0500 indicate model terms are significant. Values greater than 0.1000 indicate the model terms are not significant. The "Lack of Fit F-value" of 13.73 implies there is a 6.96% chance that a "Lack of Fit F-value" this large could occur due to noise.

The "Pred R^2" of 0.8374 is in reasonable agreement with the "Adj R^2" of 0.9075. "Adeq Precision" measures the signal to noise ratio. A ratio greater than 4 is desirable. So a ratio of 19.817 indicates an adequate signal. This model can be used to navigate the design space.

The final mathematical model in terms of coded factors became:

$$W_u = 1.02 + 0.034P - 0.13S + 0.073F + 0.23F^2 \tag{25}$$

while the final mathematical model in terms of actual factors became

$$W_u = 1.25929 + 1.69750E - 004P - 6.31250E - 003S \\ + 0.036250F + 0.056429F^2 \tag{26}$$

Figure 5.32 shows the response surfaces and the contour plots of Wu as functions of two input factors at a time, keeping the third at its intermediate value.
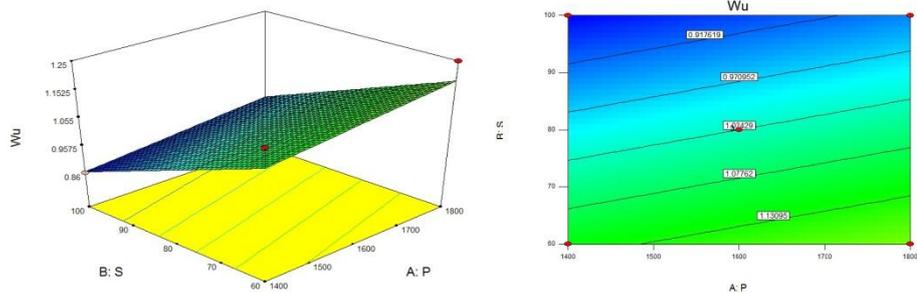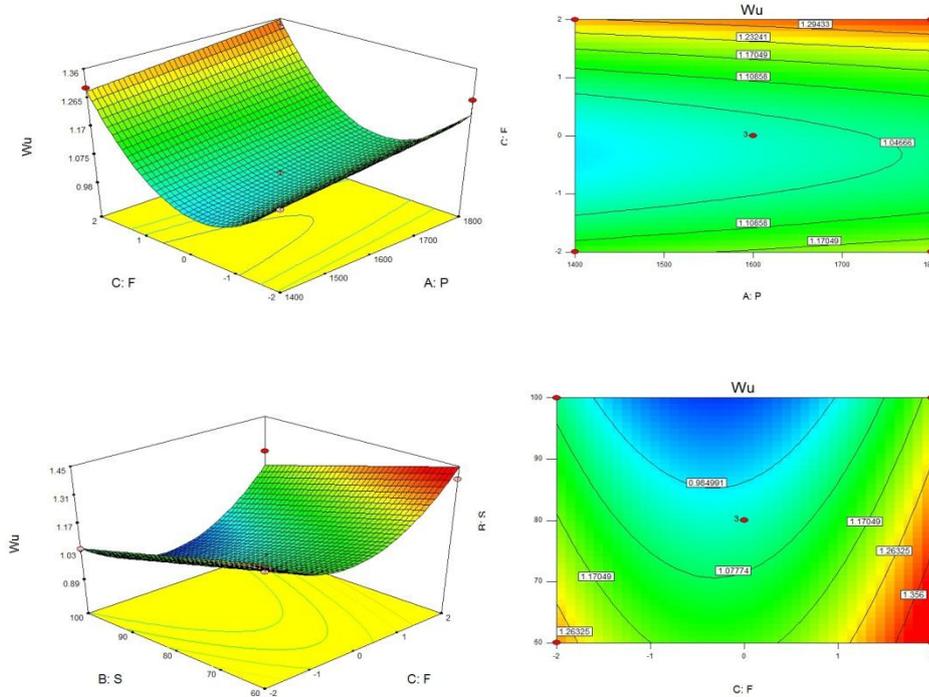
Figure 5.32 – Response surfaces and contour plots of Wu

The perturbation plot (Figure 5.33a) shows what is the influence of individual parameters and their weight on Wu: a pronounced gradient, or even a curvature indicates that the response is sensitive to that particular factor. A horizontal line, however, shows complete absence of influence of the response to this factor. Welding speed and defocusing were proven to be the factors that most influenced the Wu as previously shown by main effect plot.

Figure 5.33b shows the relationship between the actual and predicted values of Wu. This figure indicates that the developed model is adequate because the residuals in prediction of the response is minimum. The residuals tend to be close to the diagonal line indicating that the model can adequately describe the response within the limits of the factors being investigated herein. Furthermore, to verify the adequacy of the developed models, three confirmation experiments were carried out using new test conditions, but are within the experiment range previously defined.

(a)   (b)
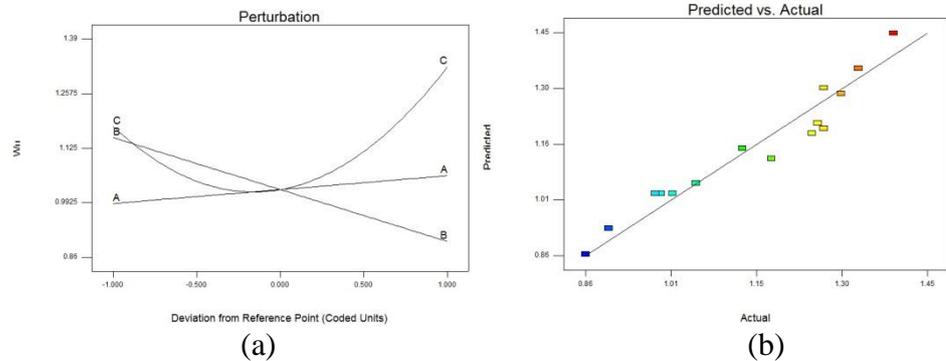
Figure 5.33 –Perturbation plot (a) and predicted vs actual (b) for Wu

Table 5.13 shows that for Wl the main effect of the power, welding speed, were the most significant model terms. Wl didn't depend on the focus position in this range. The model F-value of 50.42, implied the model was significant. The "Lack of Fit F-value" of 3.17 implies the Lack of Fit is not significant relative to the pure error. There is a 26.36% chance that a "Lack of Fit F-value" this large could occur due to noise. Non-significant lack of fit is good we want the model to fit.The "Pred R^2" of 0.8937 is in reasonable agreement with the "Adj R^2" of 0.8759. "Adeq Precision" measures the signal to noise ratio. A ratio greater than 4 is desirable. So a ratio of 20.805 indicates an adequate signal. This model can be used to navigate the design space.

Table 5.13 – ANOVA table for Wl

Source	Sum of Squares	df	Mean Square	F Value	p-value Prob > F	
Model	0.20	2	0.099	50.42	< 0.0001	significant
P	0.030	1	0.030	15.27	0.0021	
S	0.17	1	0.17	85.57	< 0.0001	
Residual	0.024	12	1.966E-003			
Lack of Fit	0.022	10	2.219E-003	3.17	0.2636	not significant
Pure Error	1.400E-003	2	7.000E-004			
Cor Total	0.22	14				

$R^2 = 0.8937$ Adj $R^2 = 0.8759$

Pred $R^2 = 0.8217$ Adeq precision = 20.805

The final mathematical model in terms of coded factors became:

$$W_l = 0.90 + 0.061P - 0.15S \tag{27}$$

while the final mathematical model in terms of actual factors became

$$W_l = 0.99 + 3.06250E - 004P - 7.25000E - 003S \tag{28}$$

Figure 5.34 shows the response surfaces and the contour plots of Wl as functions of two input factors at a time, keeping the third at its intermediate value.
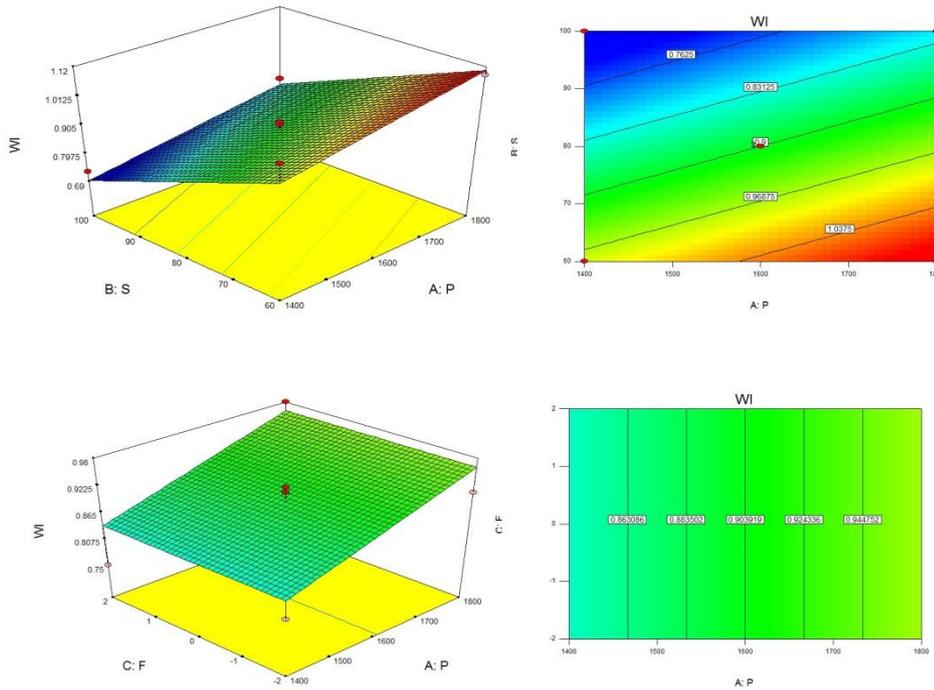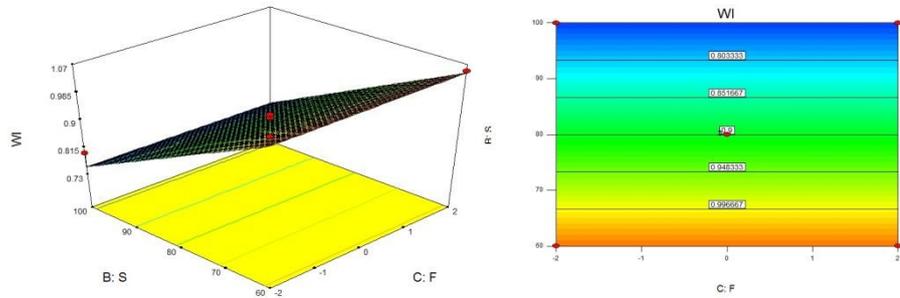
Figure 5.34 – Response surfaces and contour plots of Wl

The perturbation plot (Figure 5.35a) shows what is the influence of individual parameters and their weight on Wl. Power and welding speed were proven to be the factors that most influenced the Wl as previously shown by main effect plot. Figure 5.35b shows the relationship between the actual and predicted values of Wl. This figure indicates that the developed model is adequate because the residuals in prediction of the response is minimum, since the residuals tend to be close to the diagonal line indicating that the model can adequately describe the response within the limits of the factors being investigated herein.

(a)   (b)
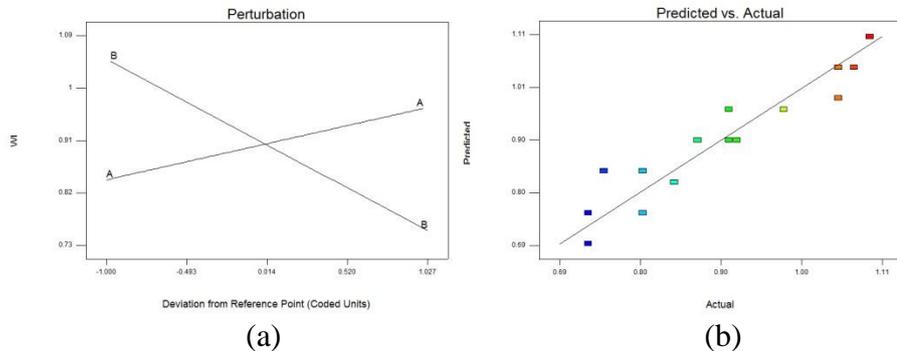
Figure 5.35 –Perturbation plot (a) and predicted vs actual (b) for Wl

Table 5.14 shows that for MA the main effect of the power, welding speed, defocusing and the second order effect of defocusing were the most significant model terms as Wl. The model F-value of 73.65, implied the model was significant. The "Lack of Fit F-value" of 1.38 implies the Lack of Fit is not significant relative to the pure error. There is a 48.67% chance that a "Lack of Fit F-value" this large could occur due to noise.

Non-significant lack of fit is good we want the model to fit. The "Pred R^2" of 0.9275 is in reasonable agreement with the "Adj R^2" of 0.9540. "Adeq Precision" measures the signal to noise ratio. A ratio greater than 4 is desirable. So a ratio of 29.433 indicates an adequate signal. This model can be used to navigate the design space.

Table 5.14 – ANOVA table for MA

Source	Sum of Squares	df	Mean Square	F Value	p-value Prob > F	
Model	0.35	4	0.086	73.65	< 0.0001	significant
P	0.036	1	0.036	31.10	0.0002	
S	0.23	1	0.23	197.25	< 0.0001	
F	0.020	1	0.020	17.06	0.0020	
F^2	0.058	1	0.058	49.20	< 0.0001	
Residual	0.012	10	1.172E-003			
Lack of Fit	9.921E-003	8	1.240E-003	1.38	0.4867	not significant
Pure Error	1.800E-003	2	9.000E-004			
Cor Total	0.36	14				

R^2=0.9672   Adj R^2=0.9540
Pred R^2=0.9275   Adeq precision=29.433

The final mathematical model in terms of coded factors became:

$$MA = 0.76 + 0.067P - 0.17S + 0.050F + 0.12F^2 \tag{29}$$

while the final mathematical model in terms of actual factors became

$$MA = 0.89571 + 3.37500E - 004P - 8.50000E - 003S \tag{30}$$
$$+ 0.025000F + 0.031071F^2$$

Figure 5.36 shows the response surfaces and the contour plots of MA as functions of two input factors at a time, keeping the third at its intermediate value.
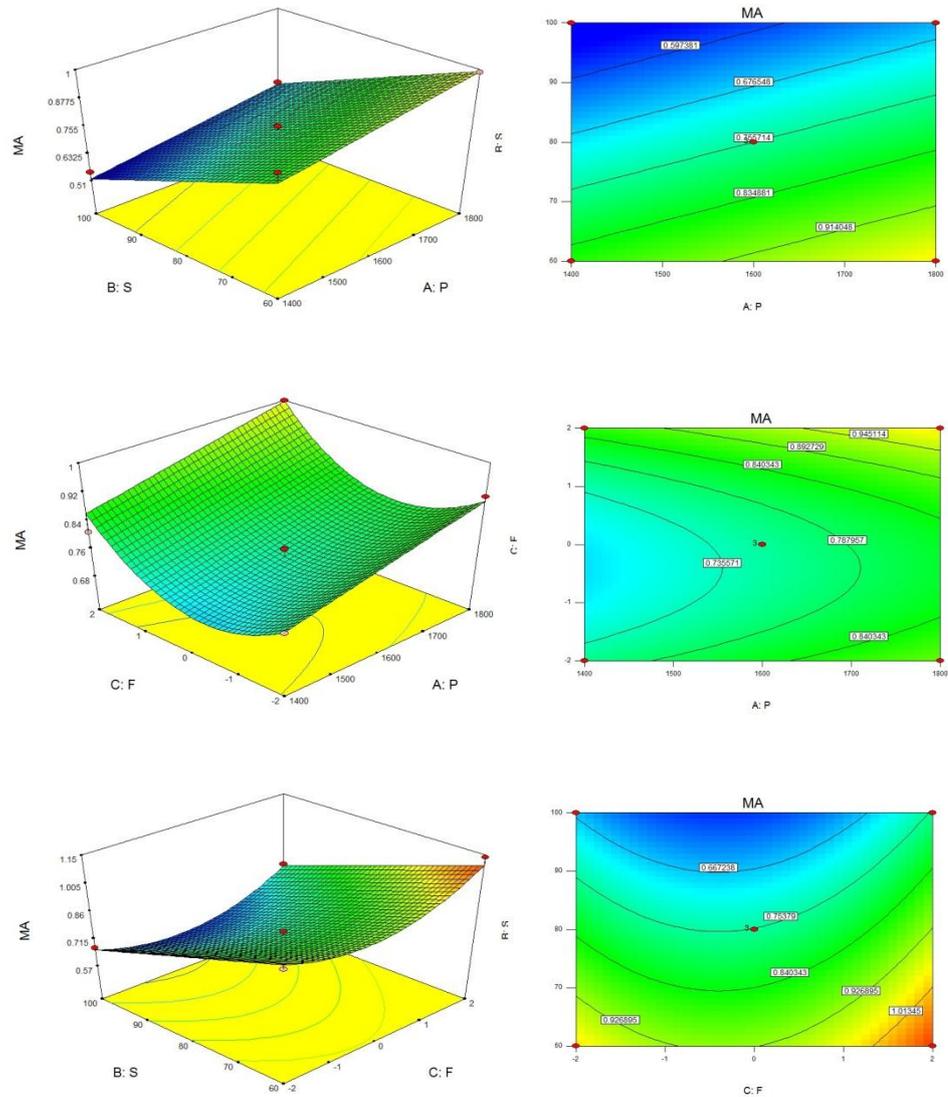
Figure 5.36 – Response surfaces and contour plots of MA

The perturbation plot (Figure 5.37a) shows what is the influence of individual parameters and their weight on MA. Welding speed is proven to be the factor that most influenced the MA as previously shown by main effect plot. Figure 5.37b shows the relationship between the actual and

predicted values of MA. This figure indicates that the developed model is adequate because the residuals in prediction of the response is minimum, since the residuals tend to be close to the diagonal line indicating that the model can adequately describe the response within the limits of the factors being investigated herein.


(a)   (b)
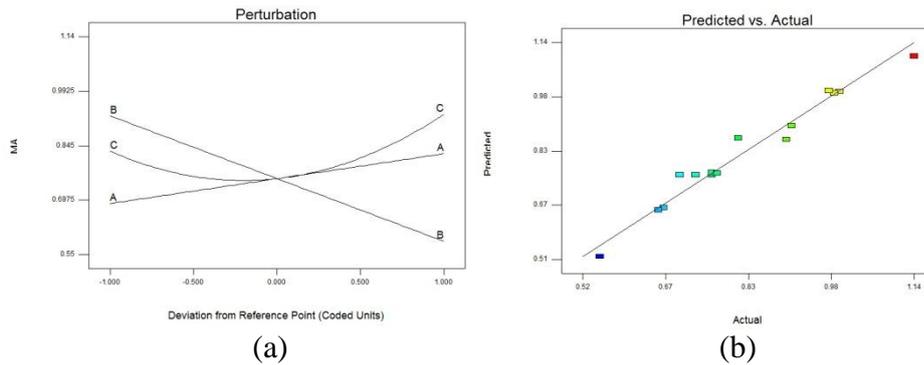
Figure 5.37 –Perturbation plot (a) and predicted vs actual (b) for MA

Table 5.15 shows that for HV the main effect of the power, welding speed, defocusing and the second order effect of defocusing were the most significant model terms. The p-value of the F term is high, but this term is necessary to make the model hierarchical and to obtain the model in terms of actual factors. The model F-value of 32.31, implied the model was significant. The "Lack of Fit F-value" of 2.49 implies the Lack of Fit is not significant relative to the pure error. There is a 31.75% chance that a "Lack of Fit F-value" this large could occur due to noise. Non-significant lack of fit is good we want the model to fit. The "Pred R^2" of 0.8220 is in reasonable agreement with the "Adj R^2" of 0.8994. "Adeq Precision" measures the signal to noise ratio. A ratio greater than 4 is desirable. So a ratio of 17.452 indicates an adequate signal. This model can be used to navigate the design space.

Table 5.15 – ANOVA table for HV

Source	Sum of Squares	df	Mean Square	F Value	p-value Prob > F	
Model	2245.95	4	561.49	32.31	< 0.0001	significant
P	489.22	1	489.22	28.15	0.0003	

S	502.13	1	502.13	28.89	0.0003	
F	8.000E-004	1	8.000E-004	4.603E-005	0.9947	
F^2	1254.60	1	1254.60	72.18	< 0.0001	
Residual	173.81	10	17.38			
Lack of Fit	157.97	8	19.75	2.49	0.3175	not significant
Pure Error	15.83	2	7.92			
Cor Total	2419.76	14				

R^2=0.9282   Adj R^2=0.8994
Pred R^2=0.8220   Adeq precision=17.452

The final mathematical model in terms of coded factors became:

$$HV = 374.42 - 7.82P + 7.92S + 1.000E - 002F + 18.33F^2 \qquad (31)$$

while the final mathematical model in terms of actual factors became

$$HV = 405.28571 - 0.039100P + 0.39612S + 5.00000E \qquad (32)$$
$$- 003F + 4.58295F^2$$

Figure 5.38 shows the response surfaces and the contour plots of HV as functions of two input factors at a time, keeping the third at its intermediate value.
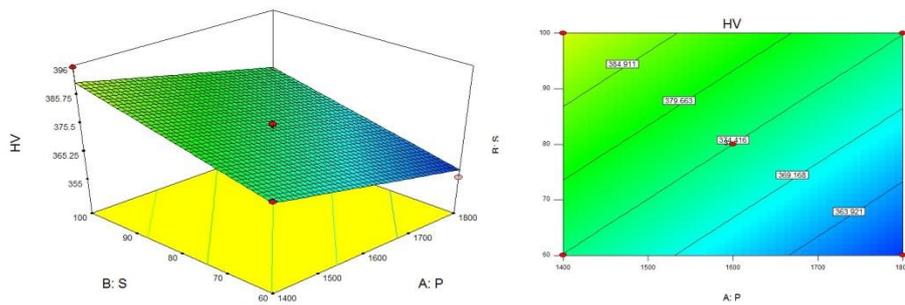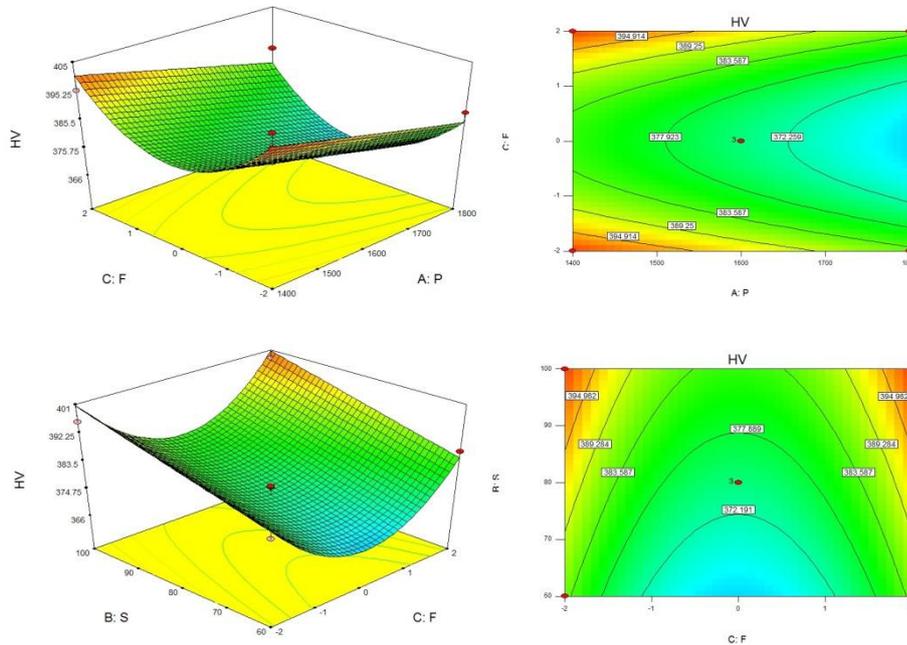
Figure 5.38 – Response surfaces and contour plots of HV

The perturbation plot (Figure 5.39a) shows what is the influence of individual parameters and their weight on HV. Power and welding speed are proven to have the same and opposite influence on HV, while focus position influences HV symmetrically (linear term F not much influential). Figure 5.39b shows the relationship between the actual and predicted values of HV. This figure indicates that the developed model is adequate because the residuals in prediction of the response is minimum, since the residuals tend to be close to the diagonal line indicating that the model can adequately describe the response within the limits of the factors being investigated herein.

(a)   (b)
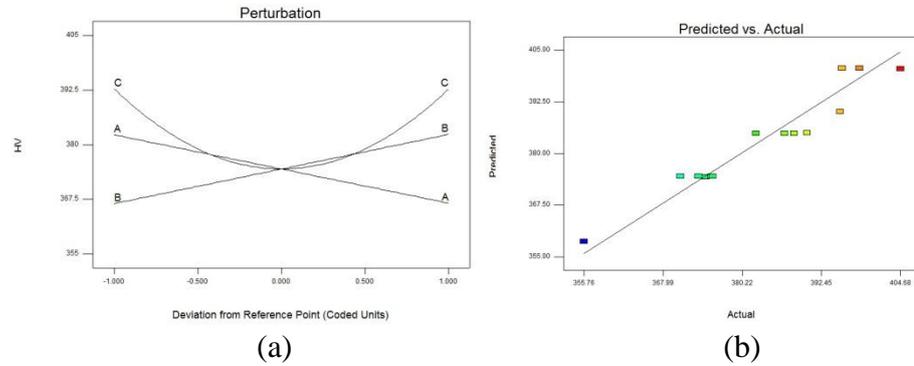
Figure 5.39 –Perturbation plot (a) and predicted vs actual (b) for HV

To verify the adequacy of the developed models, three confirmation experiments were carried out using new test conditions, but they are within the experiment range defined early. These experimental conditions were randomly selected. Then, the prediction is carried out using the previous developed models.

Each experimental condition was repeated three times and the average value was calculated.

Tables 5.16 and 5.17 summarized the experimental conditions, the actual experimental values, the predicted values and the percentages of errors. The validation results demonstrate that the developed equations are accurate because all error values are in the range of engineering errors and accepted in the industry.

Table 5.16 – Validation experimental conditions

Exp. No.	P [W]	S [mm/s]	F [mm]
1	1744	98	-1.8
2	1550	73	2
3	1632	85	-0.5

Table 5.17 – Percentage errors between actual and predicted values

Exp. No.		W_u	W_l	MA	HV
1	Act	1.13	0.83	0.76	419
	Pred	1.05	0.81	0.71	391
	|E|%	7	2	7	7
2	Act	1.26	1.03	0.98	409
	Pred	1.36	0.94	0.97	391
	|E|%	7	10	1	4
3	Act	0.94	0.91	0.78	398
	Pred	1.00	0.87	0.72	376
	|E|%	6	4	8	6

5.4.2 Optimization

There are many statistical methods for solving multiple response problems such as overlaying the contours plot for each response, constrained optimization problems and the desirability approach. The desirability method is recommended because it is simple, available in softwares and provides flexibility in giving weight and importance for all individual responses, as well. It deals with using a technique for combining multiple responses into a dimensionless measure of performance, called the overall desirability function. The desirability function approach involves transforming each estimate response, Y_i, into a unitless utility bounded $0<d_i<1$, where the higher d_i value indicates that response value Y_i is more desirable, if $d_i=0$ this means a completely undesired response. The shape of desirability function can be changed for each goal by the weight field wt_i. Weights are used to give more emphasis to the upper/lower bounds or to emphasize the target value. Weight can be ranged between 0.1 and 10; a weight greater than 1 gives more emphasis to the goal, while weights smaller than 1 give less emphasis. When the weight value is equal to 1, this will make the d_is vary from 0 to 1 in a

linear mode. In the desirability objective function D each response can be assigned an importance r relative to the other responses. Importance varies from the least important value of 1, indicated by (+), the most important value of 5, indicated by (+++++). If the varying degrees of importance are assigned to the different responses, the overall objective function is shown in Equations from 33 to 37 below, where n is the number of responses in the measure and T_i is the target value of its response.

- For the goal of maximum the desirability is defined:

$$d_i = \begin{cases} 1 & Y_i \leq Low_i \\ \left(\dfrac{Y_i - Low_i}{High_i - Low_i}\right)^{wt_i}, & Low_i < Y_i < High_i \\ 0 & Y_i \geq High_i \end{cases} \quad (33)$$

- For the goal of minimum the desirability is defined:

$$d_i = \begin{cases} 1 & Y_i \leq Low_i \\ \left(\dfrac{High_i - Y_i}{High_i - Low_i}\right)^{wt_i}, & Low_i < Y_i < High_i \\ 0 & Y_i \geq High_i \end{cases} \quad (34)$$

- For the goal as a target the desirability is defined:

$$d_i = \begin{cases} \left(\dfrac{Y_i - Low_i}{T_i - Low_i}\right)^{wt_{1i}} & Low_i < Y_i < T_i \\ \left(\dfrac{Y_i - High_i}{T_i - High_i}\right)^{wt_{2i}}, & T_i < Y_i < High_i \\ 0 & Otherwise \end{cases} \quad (35)$$

- For the goal within range the desirability is defined:

$$d_i = \begin{cases} 1, & Low_i < Y_i < High_i \\ 0, & Otherwise \end{cases} \quad (36)$$

$$D = \left(\prod_{i=1}^{n} d_i^{r_i}\right)^{\frac{1}{\sum r_i}} \qquad (37)$$

The reason for using the geometric mean rather than the arithmetic mean is that if at least one individual desirability is equal to zero, the general desirability will be equal to zero; it is necessary that a response is outside the allowed limits because all is unacceptable.

The optimization tools in Design-Expert software looks for a combination of factor levels that simultaneously match and satisfy the requirements placed (called optimization criteria) on each of the responses and factors. The optimization process involves combining the goals into the overall desirability function. Then, the numerical optimization would find one point or more that maximize this function.

First optimization criteria

The goal of the first criteria is to minimize width values and melted area, with no constraints on the process parameters, minimizing the hardness in the melted zone too. Equal importance and weight for all variables were given. Such a situation is preferable when the variables involved in the optimization process are equally important. In Table 5.18 the choices made for this optimization criteria are summarized.

Table 5.18 – First optimization criteria conditions

Name	Goal	Lower limit	Upper limit	Lower weight	Upper weight	Importance
P	is in range	1400	1800	1	1	3
S	is in range	60	100	1	1	3
F	is in range	-2	2	1	1	3
Wu	minimize	0.86	1.39	1	1	3
Wl	minimize	0.73	1.09	1	1	3
MA	minimize	0.55	1.14	1	1	3
HV	minimize	355.76	404.68	1	1	3

Figure 5.40 shows the desirability functions of process parameters P, S and F, which may vary in all of their respective ranges without favoring a specific point.
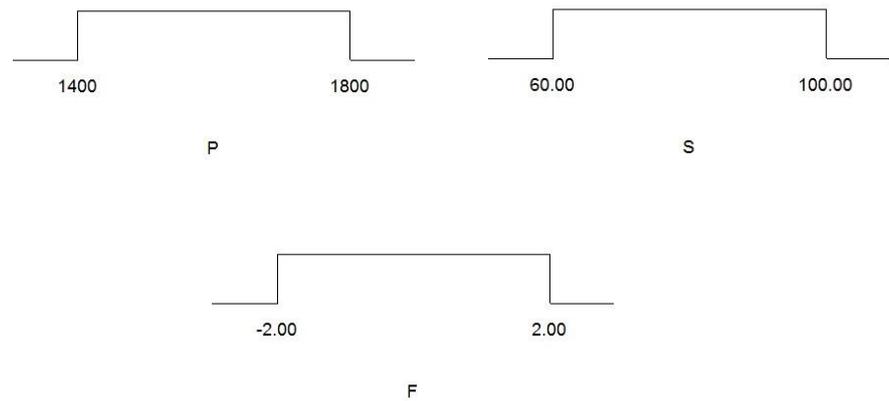

Figure 5.40 –Desirability functions of process parameters

In order to obtain a bead as narrow as possible, has been chosen to minimize the geometric characteristic. Their desirability function are shown in Figure 5.41.
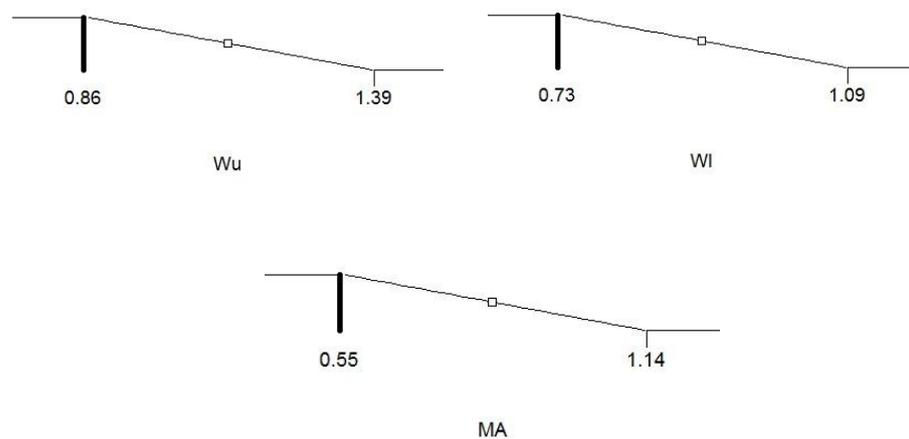

Figure 5.41 –Desirability functions of geometric features

In order to obtain similar characteristics between the base metal and weld zone avoiding subsequent post treatments, has been chosen to minimize the hardness value in the melted zone. In Figure 5.42 the desirability function of HV is shown.

355.76   404.68

HV
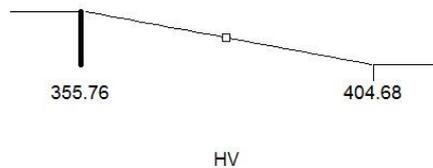
Figure 5.42 –Desirability functions of hardness

The optimization results are presented in Table 5.19. The best results (those with a higher value of desirability), are those that involve a laser power of 1577 W, a welding speed of 100 mm/s and a defocusing value of -0.15 mm, obtaining a desirability value of 0.782. Under these conditions, the upper width is set around 0.89 mm, the lower width around 0.75 mm, the melted area around 0.57 mm^2 and the hardness is 383 HV. So if the process parameters are free to change in all respective range, in order to minimize the geometric characteristics and the hardness, it should be used the maximum value of welding speed, a defocusing value near to zero and a laser power value near to the central value in the range (1600 W).

Table 5.19 – First optimization criteria results

N.	P	S	F	Wu	Wl	MA	HV	Desirability
1	1577	100.00	-0.15	0.889994	0.748105	0.575004	383.326	0.782
2	1576	100.00	-0.15	0.889749	0.74761	0.574481	383.387	0.782
3	1580	100.00	-0.15	0.890502	0.748868	0.575915	383.223	0.782
4	1574	100.00	-0.15	0.889472	0.747001	0.573858	383.461	0.782
5	1579	100.00	-0.13	0.890704	0.74869	0.57596	383.226	0.782
6	1586	100.00	-0.16	0.891248	0.750576	0.577639	383.019	0.782
7	1573	100.00	-0.13	0.889682	0.746692	0.57382	383.477	0.782
8	1562	100.00	-0.14	0.887696	0.74333	0.57001	383.914	0.782
9	1587	100.00	-0.10	0.892909	0.751052	0.579256	382.884	0.782
10	1612	100.00	-0.15	0.895916	0.758549	0.586649	381.981	0.782
11	1602	100.00	-0.26	0.892832	0.755675	0.582102	382.549	0.781
12	1524	100.00	-0.13	0.881472	0.731728	0.557357	385.385	0.781
13	1656	100.00	-0.23	0.902019	0.772008	0.600313	380.416	0.779
14	1756	100.00	-0.12	0.920873	0.802878	0.63592	376.291	0.769

Figure 5.43 shows the desirability functions to vary two process parameters at a time keeping the third at the optimum value. It is possible to observe that the desirability is maximum at 1577 W, but it doesn't change much at different power.
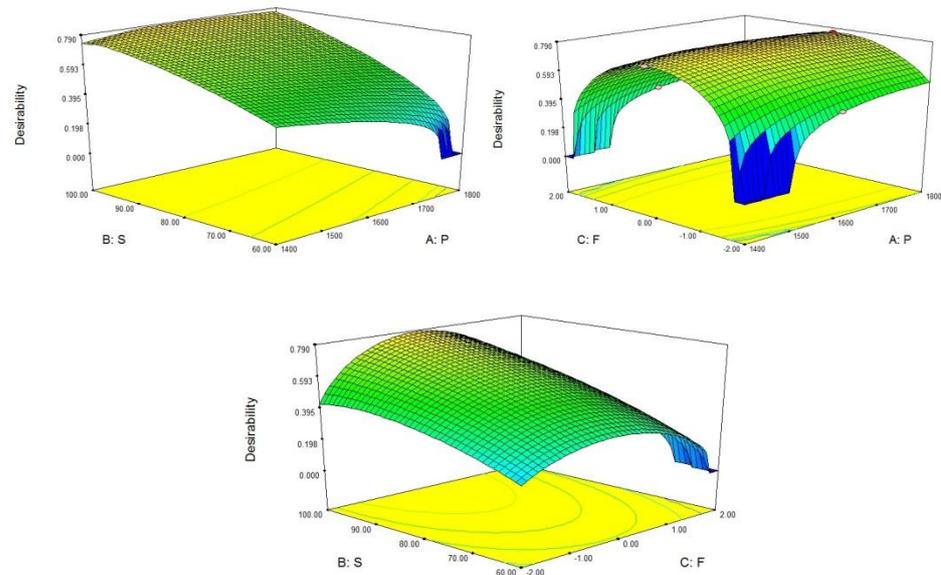
Figure 5.43 –Desirability functions for the first criteria

Second optimization criteria

A different approach may be considered when you want to give more importance to one or more answers. In this second optimization criteria (Table 5.20) more importance is given to the geometric characteristics of the bead than the hardness of the melted zone. So it's been given an importance of 5 to Wu, Wl, and MA, while HV has an importance of 3. Table 5.21 shows the results obtained after the optimization.

Table 5.20 – Second optimization criteria conditions

Name	Goal	Lower limit	Upper limit	Lower weight	Upper weight	Importance
P	is in range	1400	1800	1	1	3
S	is in range	60	100	1	1	3
F	is in range	-2	2	1	1	3
Wu	minimize	0.86	1.39	1	1	5
Wl	minimize	0.73	1.09	1	1	5
MA	minimize	0.55	1.14	1	1	5
HV	minimize	355.76	404.68	1	1	3

Table 5.21 – Second optimization criteria results

N.	P	S	F	Wu	Wl	MA	HV	Desirability
1	1518	100.00	-0.18	0.87949	0.730001	0.554606	385.685	0.843
2	1516	100.00	-0.17	0.879395	0.729359	0.554121	385.742	0.843
3	1537	100.00	-0.10	0.884314	0.73577	0.562284	384.841	0.840
4	1599	100.00	-0.39	0.892228	0.754573	0.580221	383.08	0.829
5	1663	100.00	-0.05	0.906812	0.774142	0.605566	379.907	0.816

This result shows that, compared with the first criteria optimization, it is necessary to reduce the power value to 1518 W (compared with 1577 W), to obtain an increase in the desirability that goes from 0.782 to 0.843. The best results are those that involve a laser power of 1518 W, a welding speed of 100 mm/s and a defocusing value of -0.18 mm. Under these conditions, the upper width is set around 0.88 mm, the lower width around 0.73 mm, the melted area around 0.55 mm^2 and the hardness is 386 HV. So in terms of results, comparing the optimum geometric characteristics values for both criteria, the second is just a little smaller than the first, and the difference in terms of hardness is of 3 HV.

As shown in Figure 5.44 the desirability surfaces for the second criteria are very similar to those of the first criteria.
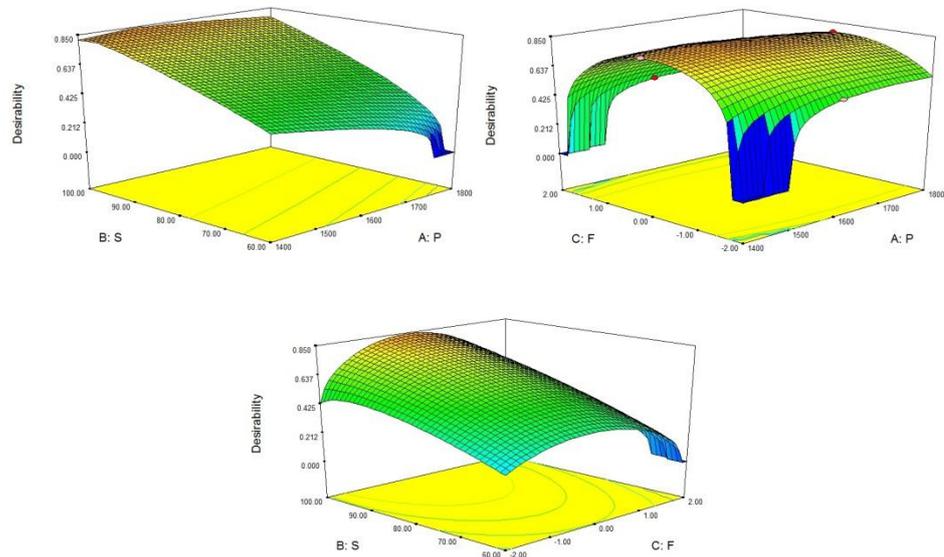
Figure 5.44 –Desirability functions for the second criteria

Third optimization criteria

In the third and last optimization criteria (Table 5.22) more importance is given to the hardness minimization of the melted zone than the geometric characteristics of the bead. So a greater importance has been given to the HV equal to 5, while to the geometric characteristics an importance of 3.

Table 5.22 – Third optimization criteria conditions

Name	Goal	Lower limit	Upper limit	Lower weight	Upper weight	Importance
P	is in range	1400	1800	1	1	3
S	is in range	60	100	1	1	3
F	is in range	-2	2	1	1	3
Wu	minimize	0.86	1.39	1	1	3
Wl	minimize	0.73	1.09	1	1	3
MA	minimize	0.55	1.14	1	1	3

HV	minimize	355.76	404.68	1	1		5

Table 5.23 – Third optimization criteria results

N.	P	S	F	Wu	Wl	MA	HV	Desirability
1	1799	100.00	-0.15	0.92743	0.815806	0.64972	374.673	0.740
2	1796	100.00	-0.15	0.926916	0.81499	0.648769	374.782	0.740
3	1794	100.00	-0.15	0.926652	0.81434	0.648128	374.859	0.740
4	1787	100.00	-0.16	0.925197	0.812178	0.64553	375.154	0.739
5	1789	99.86	-0.13	0.926996	0.813769	0.647835	374.986	0.739
6	1743	100.00	-0.14	0.918183	0.798694	0.631008	376.846	0.738
7	1722	100.00	-0.13	0.914876	0.792399	0.624198	377.641	0.737
8	1669	100.00	-0.09	0.906916	0.776258	0.607122	379.662	0.733
9	1520	100.00	-0.10	0.881481	0.730645	0.556629	385.496	0.708

As it is shown from the results of the optimization in Table 5.23, the best result has a desirability of 0.740, lower than those of the two previous criteria.

So if the process parameters are free to change in all respective ranges in order to minimize the geometric characteristics and the hardness, the maximum value of welding speed should be used and a defocusing value near to zero. But, unlike the previous criteria, a laser power value of 1799 W that is practically the maximum power range value (1800 W). Under these conditions, the upper width is set around 0.93 mm, the lower width around 0.81 mm, the melted area around 0.65 mm^2 and the hardness is 375 HV.

In Figure 5.45 the desirability surfaces are shown.
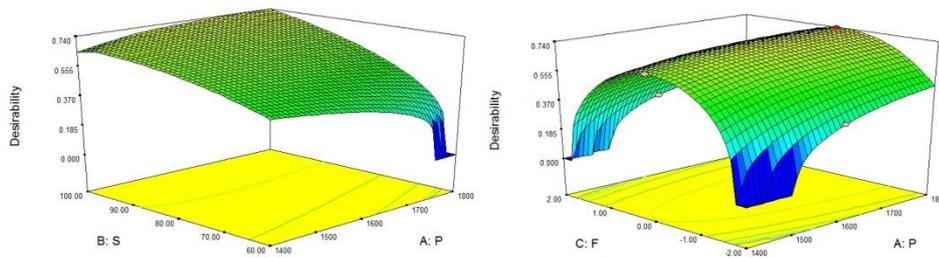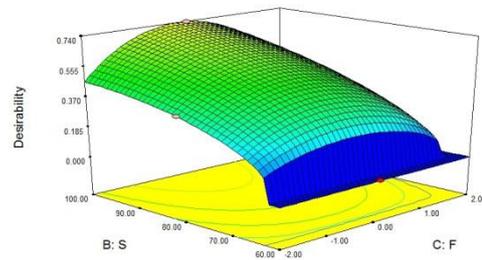
Figure 5.45 –Desirability functions for the third criteria

In conclusion, in order to minimize the geometric characteristics and hardness of the bead, all three criteria have provided as the optimum value of the welding speed the maximum one and as the optimum value of defocusing the intermediate one. Intermediate power should be used when more importance to the geometric characteristics is given, or the maximum power in order to favor the minimization of the hardness.

CONCLUSIONS

In this thesis work Bead on Plate and butt welding test on 1 mm and 3 mm-thick Ti6Al4V sheets were performed using a 2-kW Yb:YAG disk laser in order to evaluate this new generation of solid state laser and to find optimal welding parameters for the above-mentioned alloy.

In regard to 3-mm thick sheets, butt welding tests were performed by a full factorial experimental plan using three values of power and three welding speed. The joints were characterized in terms of the weld geometry, geometrical defects, porosity by X-ray inspections and resistance by tensile tests.

Fully penetrated welds were obtained for all samples except for those welded at 1500 W and 25 mm/s, which showed a non-uniform full penetration.

The melted top, heat affected zone width, melted bottom and melted area increased with increasing power and decreased with increasing welding speed.

Better quality beads were obtained with heat input values from 60 J/mm to 80 J/mm. At 60 J/mm, uniform full penetration was not assured. Furthermore, the beads shape changed from cylindrical to conical with increasing welding speed.

Geometrical defects, such as undercut, excess weld metal, excessive penetration and misalignment were in accordance with the stringent limits imposed by the UNI EN ISO 13919 1:1997 standard for all joints.

Cross-sectional analysis and X-ray examinations showed that the porosity was mainly distributed in the root of the melted area. The X-ray inspections showed a moderate increase in porosity by reducing the speed. No cracks were observed in either the melted area or in the heat affected zone.

Afterwards, bead on plate tests were performed on 3 mm-thick sheets using nine values of focus positions with constant power and welding speed. The focus positions chosen were in the range from -4 mm to +4 mm respect to the upper surface of the beads.

The bead shape changed from cylindrical to conical with increasing defocusing. The MA was maximum with 0 mm defocusing and decreased

to the minimum values with -4 mm defocusing due to lower power density.

Undercuts decreased with defocusing and the excessive penetration increased with defocusing from +3 mm to -3 mm and decreased with -4 mm defocusing.

In the melted area, a significant variation in grain size between 0 mm and ±4 mm defocusing was found. An increase of average hardness in the melted zone with increasing defocusing due to the reduction in the average size of grains was observed.

Analyzing the results obtained, the best value of defocusing was -4 mm because, among full penetrated beads, it showed lower undercut and excessive penetration, lower melted area and smaller grain size in the melted area.

In regard to 1 mm-thick sheets, butt welding tests were performed.

A Box-Behnken fractional design was conducted using three levels of power, welding speed and defocusing.

Good quality and fully penetrated welds were obtained for all samples. Geometrical features and defects were measured. Lower thermal input decreased the volume of the base metal being melted consequently the width of the welded areas decreases, as well as when the power decreased. From 0 mm to ±2 mm defocusing there was an increase in Wu and MA. Moving from the top to the bottom joint surface, a reduction of the focus position influence was observed. The upper and lower undercuts didn't show a clear trend to vary the thermal input. These could be due to the upper and lower gas flow that acted as noise.

An increase in the welding speed increased the average hardness in the melted area as well as a decrease in the power due to less heat input. Moreover, an increase of average hardness in the melted zone with increasing defocusing it was observed due to the reduction in the average size of grains in the melted zone because due to less irradiance values.

ANOVA analysis and mathematical models were carried out to predict geometrical features. These models could adequately predict the responses within the factors domain and were used to satisfy three optimization criteria. These criteria showed that, in order to minimize the geometric features and hardness of the bead, all three criteria have provided as the optimum value of the welding speed the maximum one and as the optimum value of defocusing the intermediate one. Intermediate power should be used when more importance to the

geometric features is given, or the maximum power in order to favor the minimization of the hardness.

Moreover, because titanium has a high affinity for environmental vapors and gases at high temperatures, it was necessary to manufacture an appropriate welding shielding system that gave excellent results and allowed to obtain very good quality welds.

References

- Duley, W.W., 1998. Laser welding, Wiley-Interscience.
- Silfvast, William T. "Lasers," Fundamentals of Photonics, Module 5.
- Silfvast, William T. "Lasers," Encyclopedia of Physical Science and Technology, Volume 7, Academic Press, 1987.
- Silfvast, William T. "Lasers," Handbook of Optics, 2nd Edition, Edited by Mike Bass, McGraw Hill and Optical Society of America, 1995.
- Silfvast, William T. Laser Fundamentals. New York: Cambridge University Press, 1996.
- Siegman, A. E. Lasers. Mill Valley, California: Interscience Publishers, 1986.
- A. Giesen et al., "Scalable concept for diode-pumped high-power solid-state lasers", Appl. Phys. B 58, 363 (1994)
- Giesen, A., Speiser, J., (2007), Fifteen Years of Work on Thin-Disk Lasers: Results and Scaling Laws, Journal of Selected Topics in Quantum Electronics,Vol. 13, No 3, 598-609
- J. A. Abate et al., "Active Mirror: a large-aperture medium repetition rate Nd:glass amplifier", Appl. Opt. 20 (2), 351 (1981)
- P. Klopp et al., "Highly efficient mode-locked Yb:Sc2O3 laser", Opt. Lett. 29 (4), 391 (2004)
- R. Peters et al., "Broadly tunable high-power Yb:Lu2O3 thin disk laser with 80% slope efficiency", Opt. Express 15 (11), 7075 (2007)
- C. R. E. Baer et al., "Femtosecond Yb:Lu2O3 thin disk laser with 63 W of average power", Opt. Lett. 34 (18), 2823 (2009)
- "Titanium and Titanium Alloys. Fundamentals and Applications", Edited by Christoph Leyens, Manfred Peters.
- Lee S. Smith, Philip Threadgill, Michael Gittos: "Titanium information group", Titanium Metals Corporation (2000).
- Capello, E., 2008. Le lavorazioni industriali mediante laser di potenza, Maggioli Editore.

- Sun, Z., Pan, D., Zhang, W., (2002), Correlation Between Welding Parameters and Microstructures in TIG, Plasma, and Laser Welded Ti-6Al-4V, 6th International Conference Trends in Welding Research, Pine Mountain, Georgia, USA, 760-767.

- Caiazzo, F., Curcio, F., Daurelio, G., Memola Capece Minutolo, F., (2004), Ti6Al4V Sheets Lap and Butt Joints Carried out by CO2 Laser: Mechanical and Morphological Characterization, Journal of Material Processing Technology, 149, 546-552.

- Cao, X., Jahazi, M., (2009), Effect of Welding Speed on Butt joint Quality of Ti6Al4V Alloy Welded Using a High-Power Nd:YAG Laser, Optics and Lasers in Engineering, 47, 1231-1241.

- Akman, E., Demir, A., Canel, T., Sinmazcelik, T., (2009), Laser Welding of Ti6Al4V Titanium Alloys, Journal of Materials Processing Technology, 209, 3705-3717.

- Mazumder, J., Steen, W. M.,(1980), Welding of Ti-6Al-4V by Continuous Wave CO2 Laser, Metal Construction, 12/9, 423-427.

- Tsay, L. W., Tsay C. Y., (1997), The Effect of Microstructures on the Fatigue Crack Growth in Ti-6Al-4V Laser Welds, International Journal of Fatigue, 19/10, 713-720.

- Serroni, G., Bitonto, C., Prisco, U., Squillace, A., Favi, A., Prisco, A., (2010), Mechanical Characterization of Nd:YAG Laser Welding on Ti-6Al-4V, Innovative Production Machines and System.

- Cao, X., Jahazi, M., Immarigeon, J., P., Wallace, W., (2006), A Review of Laser Welding Techniques for Magnesium Alloys, Journal of Materials Processing Technology, 171/2, 188-204.

- Cheolhee, K., Junghak, K., Hyunsik, L., Jeonghan, K., (2008), Investigation of Laser Remote Welding using Disc Laser, Journal of Materials Processing Technology, 201, 521-525.

- Mastrocinque, E., Corrado, G., Caiazzo, F., Pasquino, N., Sergi, V., (2011), Pulsed-disk-laser Welding of Ti6Al4V, 9th International Conference on Advanced Manufacturing Systems and Technology, Mali Losinj, Croatia.

- Wang, S., H., Wei, M., D., Tsay, L., W., (2003), Tensile Properties of LBW Welds in Ti6Al4V Alloy at Evaluates Temperatures below 450 °C, Materials Letters, 57, 1815-1823.

- Kabir, A. S. H., Cao, X., Medraj, M., Wanjara, P., Cuddy, J., Birur, A., (2010), Effect of Welding Speed and Defocusing Distance on the Quality of Laser Welded Ti-6Al-4V, Material Science and Tecnology, Houston, Texas, 2787-2797.
- Khaled, Z., (1994), An Investigation of Pore Cracking in Titanium Welds, Journal of Materials Engineering and Performance, 3/3, 419-434.
- Casavola, C., Pappalettere, C., Tattoli, F., (2009), Experimental and Numerical Study of Static and Fatigue Properties of Titanium Alloy Welded Joints, Mechanics of Materials, 41, 231-243.
- E. Mastrocinque, G. Corrado, F. Caiazzo, N. Pasquino, V. Sergi, F. Acerra, Disk Laser Welding of Ti6Al4V Alloy, 21th Internation Conference on Production Research, Stuttgart, Germany, (2011).
- EN ISO 13919-1: 1997. Welding - Electrons and laser beam welded joints - Guidance on quality levels for imperfections – Steel.
- Montgomery, D. C., Design and Analysis of Experiments, Mc-Graw Hill (2005).
- http://www.rp-photonics.com/thin_disk_lasers.html